Synthesis and Optoelectronic properties of ultrathin Bi_2O_2Se Nanosheets

विद्या वाचस्पति की
उपाधि की अपेक्षाओं की आंशिक पूर्ति में प्रस्तुत शोध प्रबंध

A thesis submitted in partial fulfillment of the requirements of the degree of Doctor of Philosophy

द्वारा
सूरज लखचौरा

By
Suraj Lakhchaura

पंजीकरण सं. / Registration No.: **20193631**

शोध प्रबंध पर्यवेक्षक / Thesis Supervisor:
Dr. Atikur Rahman

भारतीय विज्ञान शिक्षा एवं अनुसंधान संस्थान पुणे
INDIAN INSTITUTE OF SCIENCE EDUCATION AND RESEARCH PUNE

2024

Certificate

Certified that the work incorporated in the thesis entitled "**Synthesis and Optoelectronic properties of ultrathin Bi_2O_2Se Nanosheets**", submitted by **Suraj Lakhchaura**, was carried out by the candidate under my supervision. The work presented here or any part of it has not been included in any other thesis submitted previously for the award of any degree or diploma from any other University or institution.

Pune 411008 **Dr. Atikur Rahman**

14 August, 2024 Supervisor

Declaration by Student

Name of Student: **Suraj Lakhchaura**

Reg. No.: **20193631**

Thesis Supervisor : **Dr. Atikur Rahman**

Department: **Physics**

Date of joining program: **01/01/2019**

Date of Pre-Synopsis Seminar : **17/052024**

Title of Thesis: **Synthesis and Optoelectronic properties of ultrathin Bi_2O_2Se Nanosheets**

I declare that this written submission represents my idea in my own words and where others' ideas have been included; I have adequately cited and referenced the original sources. I declare that I have acknowledged collaborative work and discussions wherever such work has been included. I also declare that I have adhered to all principles of academic honesty and integrity and have not misrepresented or fabricated or falsified any idea/data/fact/source in my submission. I understand that violation of the above will be cause for disciplinary action by the Institute and can also evoke penal action from the sources which have thus not been properly cited or from whom proper permission has not been taken when needed.

The work reported in this thesis is the original work done by me under the guidance of

Dr. **Atikur Rahman**

Date: **14/08/2024**

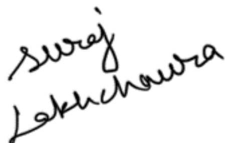

Signature of the student

To My Sister, Father, and Late Mother

Acknowledgment

I am incredibly grateful to my advisor Dr. Atikur Rahman, for his invaluable guidance, unwavering support, and continuous encouragement throughout my research journey. He has provided me full freedom to do experiments and explore resources and instruments available in our lab. I am grateful for the serene research environment he established, as he always showed concern for our physical and mental well-being.

I want to thank my RAC members Prof. Subhabrata Dhar and Dr. Aparna Deshpande for their invaluable suggestions, constructive feedback and comments during annual RAC meetings. I express my gratitude to CSIR for the Fellowship

I want to thank my seniors, Dr. Gokul and Dr.Vrinda, for providing a very friendly Lab environment. I want to thank Gokul Bhai for sharing his knowledge not only in Experiments but also in wildlife, geopolitics, and cinema. I know him more as an elder brother than a senior. I want to thank Manisha for making delicious tea. I would like to thank all my past and present labmates for making a vibrant research environment in our lab from which my work has greatly benefited.

I wish to extend my appreciation to all the staff: Technical, Physics office, Academic office, housekeeping, and hostel for their help and for making my academic and nonacademic journey better.

I want to thank my batchmates Iktesh bhai and Dhruv bhai for their valuable comparing during my PhD tenure. I want to thank Digvijay Bhai and Manisha for making delicious tea. My Ph.D. journey is incomplete without their tea. I want to thank Deepak bhai and Bhabhiji for offering delicious food during Diwali and other occasions, and also for their company during evening walk. I would like to thank my floormates Dhruv bhai, Iktesh bhai, Akash bhai, Aman bhai,

Digvijay bhai, Sushant bhai, and others for their company in cooking food, celebrating birthdays, Tracking and other stuff. All the members of the 9th floor are always my family.

Lastly, I am grateful to my family members, especially my sister, father, and Late mother, for their invaluable support throughout my life.

Abstract

Bismuth oxyselenide (Bi_2O_2Se) has garnered significant attention as a promising two-dimensional material for next-generation electronic and optoelectronic devices due to its remarkably high mobility, moderate bandgap, exceptional environmental stability, and possession of a high-dielectric constant native oxide. Bi_2O_2Se-based field-effect transistors (FETs) have demonstrated outstanding current on/off ratios exceeding 10^6 with an almost ideal subthreshold swing of approximately 65 mV dec^{-1}, crucial for low-power logic devices. This stratified material exhibits a unique defect structure where the donor state is situated above the conduction band, resulting in exceptional metallicity. In this Thesis, we have investigated the optoelectronic properties of Bi_2O_2Se nanosheets. In the thesis firstly, we have optimized the growth conditions for synthesizing ultrathin nanosheets of Bi_2O_2Se on Fluorophlogopite mica. We have developed a non-corrosive dry transfer method to Transfer these nanosheets for studying their electrical Properties. Our transferred nanosheets display outstanding optoelectronic properties, which is attributed to our damage-free transfer method.

Then we have investigated the temperature-dependent electronic Transport properties of our samples. Here, we report the observation of metal insulation transition in a few nanometer-thin Bi_2O_2Se nanosheets by tuning the carrier density via back gate biasing. At high carrier density $\sigma = n^{\alpha}$, our devices displayed $\alpha \sim 1$, which tells about the presence of screened coloumb impurity scattering. As we decreased the carrier density below a critical density n_C, the charge homogeneity of the system breaks down, resulting in the development of strong inhomogeneity. This leads to a percolation-driven transition in our system. At low carrier density $n < n_C$, the system is in an insulating phase where transport is well described by a thermal activation mechanism where carriers are trapped in localized states, demonstrating the

role of disorder in our system. Our extracted value of average percolation exponent $\delta = 1.28$ matches well with the theoretical value of 4/3, confirming percolation-based MIT in Bi_2O_2Se nanosheets.

List of Publications

1. Suraj Lakhchaura, Gokul M A and Rahman A 2024 Ultrahigh responsivity of non-van der Waals Bi_2O_2Se photodetector Nanotechnology 35 075707.

2. Suraj Lakhchaura, Gokul M A and Rahman A 2024 Gate induced Metal-Insulator Transition in Bi_2O_2Se. (Under Review in Communication materials)

Conference presentations -

1. Optoelectronic properties of Ultrahigh mobility of Bi_2O_2Se Nanosheets (Poster Presentation), Emerging Materials 2023.

2. Gate induced Metal-Insulator Transition in Bi_2O_2Se (Poster Presentation), RPGR 2023.

Contents

Certificate iii

Declaration by Student v

Acknowledgment ix

Abstract xi

List of Publications xiii

Chapter 1: Introduction 1

1.1 Family of 2D materials 1

1.2 Preparation Methods of Bi_2O_2Se 3

1.2.1 Chemical vapor deposition 4

1.2.2 Pulsed laser deposition 5

1.2.3 Molecular beam epitaxy 6

1.2.4 Solution-assisted method 8

1.2.5 liquid-phase exfoliation method 9

1.3 Crystal Structure of Bi_2O_2Se 10

1.4 Electronic Band Structure of Bi_2O_2Se 12

1.5 Thesis Outline 14

Bibliography 15

Chapter 2: Experimental Techniques 21

2.1 Material Synthesis 21

2.1.1 Chemical Vapor Deposition 21

2.2 Characterization techniques 24

2.2.1 Raman Spectroscopy 24

2.2.2 Atomic Force Microscopy 26

2.2.3 Scanning Electron Microscopy 28

2.2.4 Transmission Electron Microscopy 29

2.3 Device Fabrication 30

2.3.1 Photolithography 30

2.3.2 Physical Vapor Deposition 32

2.3.2.1 Thermal Evaporation 33

2.3.2.2 Sputtering 34

2.3.3 Reactive Ion Etching 35

2.3.4 Wire Bonding 37

2.4 Interfacing of Instruments 38

Bibliography 40

Chapter 3: Ultrahigh responsivity of non-van der Waals Bi_2O_2Se photodetector 43

3.1 Introduction 43

3.2 Experimental Details 45

3.2.1 Growth and Characterization 45

3.2.2 Transfer and device fabrication 45

3.2.3 Electrical Measurement 46

3.3 Results and Discussion 47

3.3.1 CVD Growth of Bi_2O_2Se 47

3.3.2 Characterisation of as-grown Bi_2O_2Se 48

3.3.3 Nail Polish Assisted Transfer and Electrical Characterisation 52

3.3.4 Optoelectronic properties 56
3.4. Summary 64
Bibliography 64

Chapter 4: Carrier Density Induced Metal-Insulator Transition in Bi_2O_2Se Nanosheets 71

4.1 Introduction 71
4.2 Experimental Details 74
4.3 Results and Discussion 74
4.3.2 Temperature Dependent Electronic Transport Properties 78
4.3.3 Metal-Insulator Transition 81
4.3.4 Percolation Driven Transition 84
4.4 Summary 87
Bibliography 87

Chapter 5: Conclusion and Future Directions 93

5.1 Conclusion 93
5.2 Future Directions 93
5.2.1 Encapsulated Bi_2O_2Se 94
5.2.2 Dual-Gated Bi_2O_2Se 95
5.2.3 F-Mica as a Back Gate 98
5.2.4 $CsPbBr_3$/ Bi_2O_2Se Heterostructure 100

Appendix A 101
Appendix B 103

Chapter 1

Introduction

Since the discovery of graphene in 2004, the scientific community has been captivated by two-dimensional (2D) materials. Their unique physical and chemical properties are significantly altered by the quantum size effect, stemming from their nanoscale thickness[1,2]. This confinement of charge carriers, light, and heat within the 2D plane induces notable transformations in electronic and optical characteristics[3,4]. The realm of 2D materials is vast, encompassing a diverse array of elements from the periodic table[5]. Consequently, this diversity yields a wide spectrum of electronic behaviors, including metals, semimetals, insulators, and semiconductors with bandgaps across the ultraviolet to infrared spectrum[6–8]. Furthermore, the 2D structure aligns seamlessly with current thin film fabrication methods in the semiconductor industry, enabling easy integration with conventional electronic materials like silicon and application on various substrates. This synergy positions 2D materials as promising contenders for advancing nanoelectronics, optoelectronics, and the development of ultra-thin, flexible devices. Notably, the demonstration of 2D atomic crystal integration circuits, encompassing memory, logic gates, amplifiers, oscillators, mixers, switches, and modulators, showcases the potential for 2D materials to spearhead a new era of electronic devices[9]. Leveraging functional integration circuits crafted from 2D materials holds promise in addressing both technological and foundational hurdles in the electronics industry.

1.1 Family of 2D materials

A wide range of 2D materials have been investigated through years of research, showcasing diverse electronic properties from conductors to insulators. This family of materials includes graphene, MXenes, 2D transition metal dichalcogenides (TMDs), layered perovskites, black phosphorus (BP), graphitic carbon nitride (g-C3N4), hexagonal boron nitride (hBN), and metal phosphorus trichalcogenides. These materials have been researched and analyzed to examine their material characteristics and possibilities for sensing, optoelectronic, storage, catalysis, memory, and dielectric applications[10–16]. Besides the outstanding features mentioned earlier, research also indicates the constraints linked to these 2D materials. Graphene's high mobility ($>10^4$ cm^2 V^{-1} s^{-1}) is impressive. However, it's limited on/off ratio resulting from the lack of a bandgap hinders its use in electronic applications[17,18]. Conversely, 2D TMDs provide. a bandgap modulated by layers, but their application is restricted due to the low carrier mobility at room temperature[19–21]. Despite its exceptional mobility and broad bandgap tunability, the practical application of BP as a semiconductor is impeded by stability and processability limitations[22]. Most 2D materials, including BP, exhibit high air sensitivity, instability, and subpar performance due to their van der Waals nature and interlayer gap. These setbacks restrict the utilization of 2D materials in device applications. Hence, there is a pressing need to explore, design, and study novel 2D materials with adjustable electronic properties, high carrier mobility, processability, and environmental stability to enable the development of cutting-edge semiconductor devices[23].

Recently, 2D bismuth oxychalcogenides (BOXs) have garnered considerable interest because of their outstanding physical and chemical characteristics, including high carrier mobility, environmental stability, and tunable band gap. Theoretical results indicated that among the BOXs,

Bi_2O_2Se is the easiest to grow due to its relatively wider ranges of stable chemical potential, and therefore, it has been explored more for fundamental and industrial applications.

1.2 Preparation Methods of Bi_2O_2Se

Many research endeavors have focused on achieving uniform large-scale growth of 2D Bi_2O_2Se through a variety of top-down and bottom-up techniques. These methods include molecular beam epitaxy (MBE), chemical vapor deposition (CVD), various chemical reaction approaches, salt-assisted CVD, and mechanical exfoliation. The majority of documented findings have primarily centered on the CVD growth process due to its ability to produce atomically uniform 2D Bi_2O_2Se with favorable nucleation characteristics. While the exfoliation method can yield high-quality van der Waals (vdW) 2D materials, the high interlayer binding energy in Bi_2O_2Se hinder achieving large-scale atomic uniformity, particularly in exfoliating down to monolayer thickness. Leveraging the formal bonds, the chemical reaction route has also been utilized for scalable production and fundamental research of Bi_2O_2Se[24,25]. However, chemically integrated Bi_2O_2Se is prone to forming bonds with external molecules (like oxygen) during the reaction process. Recently, solution-assisted and salt-assisted (e.g., sodium chloride; NaCl) CVD methods have been adopted to produce high-quality Bi_2O_2Se with controlled growth across wafer scales[26]. The methods for fabricating Bi2O2Se films are categorized into three main groups: (1) atomic deposition (CVD, MBE), (2) chemical reaction (solution-assisted), and (3) mechanical exfoliation. This discussion

delves into a few newly developed synthesis techniques of Bi_2O_2Se, outlining their advantages and disadvantages in terms of mechanisms, structure, thickness, domain size, and quality.

1.2.1 Chemical vapor deposition

Chemical vapor deposition (CVD) is a widely used bottom-up technique for producing 2D materials. It requires optimization of various growth factors, including gas pressure, heating temperature, gas flow rate, precursor concentration, and more, to achieve the production of ultra-thin 2D films at the atomic level[24,27–29]. In this procedure, vaporous compounds are initially produced and carried by an inert gas to the desired substrate. Bi_2O_2Se thin films of superior quality, featuring customizable size, precise thickness control, and exceptional electronic characteristics, can be produced utilizing the CVD technique. In the initial phases of the research, Wu et al. and Li et al. successfully created large-area, high-mobility 2D Bi_2O_2Se crystals in thin film form on mica using Bi_2O_3 and Bi_2Se_3 as precursors[30,31]. This process is detailed in Fig. 2(b) The control over nucleation sites, thickness, domain sizes, and crystal phase transition of Bi_2O_2Se thin films was achieved by adjusting growth conditions. For instance, temperature control enabled the synthesis of planar and vertical Bi_2O_2Se nanosheets. Lower temperatures facilitated a kinetics-dominated growth, allowing for vertical growth unrestricted by the substrate. Conversely, at higher

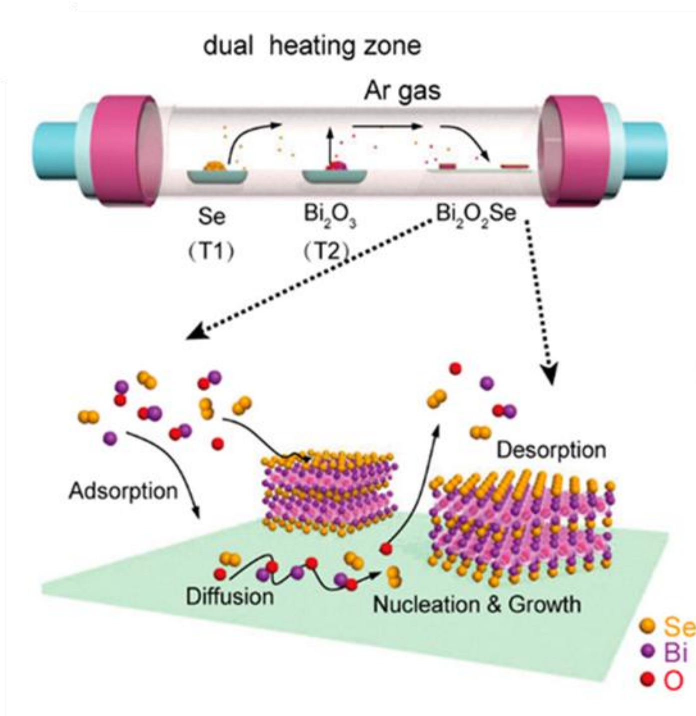

Figure 1.1. Schematic illustrating the Growth of Bi_2O_2Se using CVD . This image has been adapted with permission from Ref.[49] Copyright © 2019, American Chemical Society

temperatures, thermodynamics-controlled growth resulted in only laterally arranged Bi_2O_2Se due to increased adatom migration rates[31,32].

1.2.2 Pulsed laser deposition

The PLD method is utilized to create a thin film with identical stoichiometry to that of the source (target). This process involves directing a focused, intense laser beam onto the target to vaporize

the material within a high vacuum environment inside a chamber. The vaporized material then gets deposited onto the substrate. PVD is a widely utilized and extensively explored technique for depositing metal oxides and various other materials. Recent studies have documented the deposition of Bi_2O_2Se thin films using the PLD method[33,34]. Song et al. demonstrated the growth of a single-crystalline Bi_2O_2Se thin film on a $SrTiO_3$ substrate[34]. This method allows for the creation of Bi_2O_2Se at lower growth temperatures while maintaining precise control over thickness and stoichiometry.

1.2.3 Molecular beam epitaxy

Molecular beam epitaxy (MBE) presents an alternative method for producing Bi_2O_2Se through atomic deposition with precise control over thickness[35–37]. **In Fig 1.5b (left panel),** a diagram illustrates the process of preparing atomically thin Bi_2O_2Se films using the MBE technique. To grow Bi_2O_2Se films, Bi and Se sources are evaporated using standard effusion cells within a carefully regulated oxygen atmosphere[35]. The use of mica, with its insulating properties, and Nb-doped STO (with approximately 0.5% mismatch), known for its excellent conductivity, are well-matched substrates for this growth. Essential factors for successful MBE growth include maintaining control over the Se/Bi flux ratio, oxygen pressure, and growth temperature (T_G). It is crucial for T_G to be set between the evaporation temperatures of the two sources (e.g., $T_{Bi} > T_G > T_{Se}$) to ensure precise thickness control and prevent unwanted bulk crystal growth resulting from impurities like Se-rich or Se-poor conditions. By operating within the Se evaporation temperatures

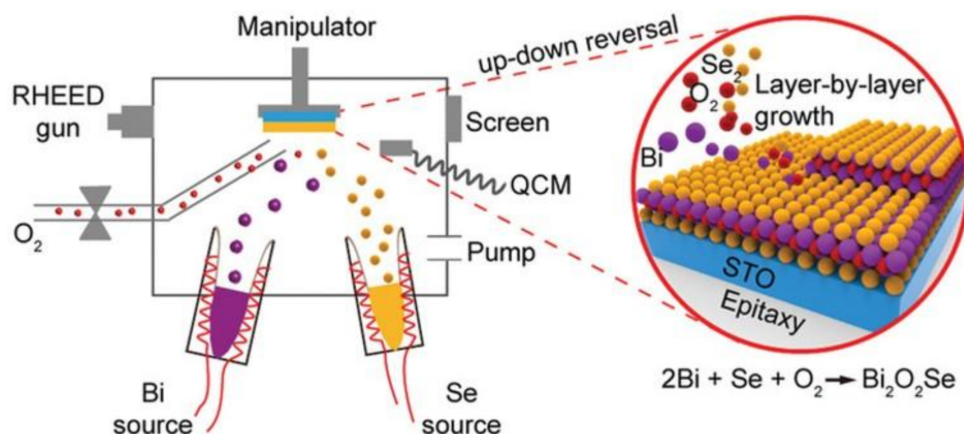

Figure 1.2 Schematic illustrating the Growth of Bi_2O_2Se using MBE . This image has been adapted with permission from Ref.[35] Copyright © 2019 Wiley-VCH

of 100 to 350 °C, it becomes feasible to achieve low-temperature growth of Bi_2O_2Se. A lower flux ratio (Se/Bi) coupled with higher oxygen pressure aids in the production of a pure Bi_2O_2Se phase, effectively avoiding Bi_2Se_3 impurities. Liang et al. successfully synthesized a pure Bi_2O_2Se phase equivalent to one unit cell on STO terraces at T_G = 290 °C[35]. The thickness of Bi_2O_2Se was tracked by varying the growth time, witnessing the merger of monolayer islands into uniform large-area growth. Continual growth over time allows numerous monolayers to merge electrostatically, facilitating multilayer growth. While this method enables the high-quality growth of 2D Bi_2O_2Se at low temperatures, its implementation is constrained by the requirement for sophisticated instrumentation, limiting its accessibility.

1.2.4 Solution-assisted method

Recently, Zhang et al. have developed a solution-assisted method for the easy, quick, and scalable synthesis of Bi_2O_2Se thin films on flexible muscovite substrates[38]. This method involves utilizing the selenization technique for Bi_2O_2Se growth. By using $Bi(NO_2)_3/(CH_2OH)_2$ as the source for the BiO layer and Se as the source for chalcogenide layers, they were able to grow layered Bi_2O_2Se. By adjusting the rotation speeds during spin-coating of a uniform layer of $Bi(NO_2)_3/(CH_2OH)_2$, the layer thickness can be controlled.

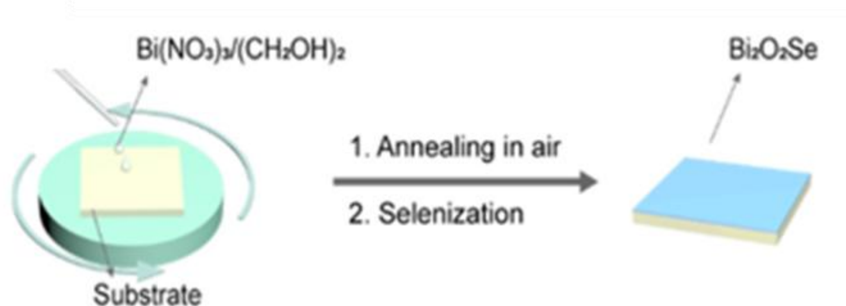

Figure 1.3 Schematic illustrating the Growth of Bi_2O_2Se using solution-assisted method. This image has been adapted with permission from Ref.[38] Copyright © 2020 American Chemical Society

In another study, Dang et al. optimized an ion template-assisted method in a KOH medium for the growth of a uniform few layers of Bi_2O_2Se with oxygen deficiencies. This well-known

hydro/solvothermal method can be tailored to produce Bi_2O_2Se nanostructures with various morphologies and defects to influence their electronic properties[39].

A simple technique for Bi_2O_2Se growth involves the self-assembly of BiO and Se layers through a chemical reaction using $Bi(NO_3)_2 \cdot 5H_2O$ as the source for the BiO layer and $Se(NH_2)_2$ for the Se layer. This method allows for the synthesis of free-standing Bi_2O_2Se nanosheets at room temperature under atmospheric conditions[25]. However, the presence of solvent and byproducts in this process may lower the quality of the flakes and introduce defects and impurities. Therefore, meticulous characterization is essential to understand the properties of pure Bi_2O_2Se produced through this method.

1.2.5 liquid-phase exfoliation method

Another method for producing 2D Bi_2O_2Se involves exfoliating the bulk powder, as depicted in Fig. 1.5d. Bi_2O_2Se nanosheets are derived from bulk Bi_2O_2Se using the liquid exfoliation method[40]. Bi_2O_2Se quantum dots can be created through conventional bath and probe sonication methods. Extremely small Bi_2O_2Se QDs can be achieved by following three steps: grinding the bulk to create a fine powder, bath sonication of the fine powder, and then ice bath probe sonication for several hours. For the preparation of Bi_2O_2Se QDs, the bulk powder is ground into fine powders and dispersed in N-methyl-2-pyrrolidone (NMP), followed by liquid exfoliation for a few hours

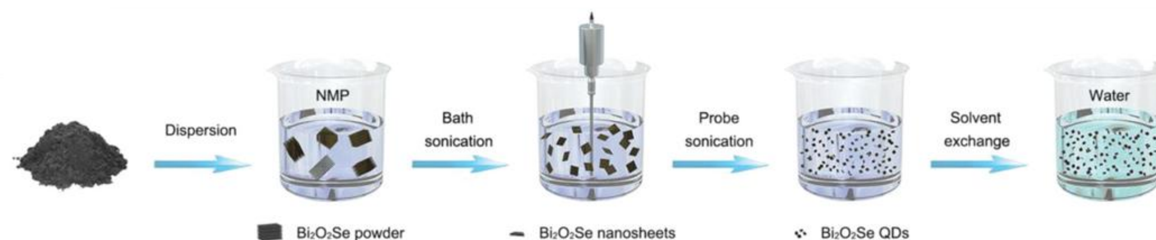

Figure 1.4 Schematic illustrating the Growth of Bi_2O_2Se using liquid-phase exfoliation method . This image has been adapted with permission from Ref.[40] Copyright © 2020 Wiley-VCH

involving ice-bath sonication and ultrasound-probe sonication[40]. Subsequently, to alter the solvent, centrifugal separation or solvent removal (using a magnetic stirrer on a hot plate) of the QDs must be performed and dispersed in the desired solvent.

1.3 Crystal Structure of Bi_2O_2Se

Bi_2O_2Se represents one of the charge-carrying quasi-2D semiconductors exhibiting inherent n-type characteristics. It features a layered body-centered tetragonal structure with lattice parameters a = b = 3.887 Å and c = 12.164 Å, belonging to the I4/mmm space group. Bi_2O_2Se consists of alternately charged layers along the c axis; specifically, positive $[Bi_2O_2]_n^{2n+}$ layers alternating with negative $[Se]_n^{2n-}$ layers[41]. The separation distance of 3.272 Å between Bi and Se is significantly greater than the combined effective ionic radii (3.01 Å) of Bi^{3+} (1.03 Å) and Se^{2-} (1.98 Å) as well

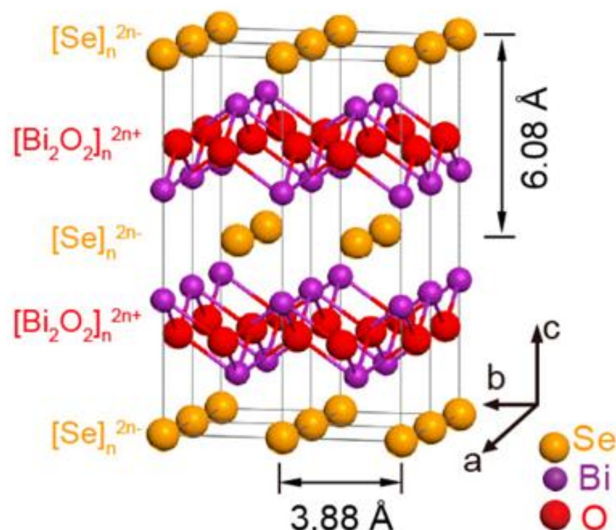

Figure 1.5. Schematic illustrating the crystal structure of Bi_2O_2Se. This image has been adapted with permission from Ref.[30] Copyright © 2017 American Chemical Society

as the covalent bond length of Bi_2Se_3[42]. This implies that the bonding interaction between the Bi and Se layers in Bi_2O_2Se is predominantly a weak electrostatic interaction. Conversely, the BiO bond within the Bi_2O_2 layer exhibits a significantly shorter bond length of 2.31 Å due to a strong Bi-O interaction, attributed to the higher electronegativity and smaller atomic radius of O^{2-} (0.14 nm) in comparison to Se^{2-} (0.198 nm). Bi_2O_2Se features an interlayer binding energy of 76.80 meV/A^2 [43] , surpassing that of conventional 2D materials, which makes it challenging to mechanically exfoliate in contrast to other 2D materials.

1.4 Electronic Band Structure of Bi_2O_2Se

Bi_2O_2Se can be seen as a variation of the topological insulator Bi_2Se_3. By replacing some heavy selenium atoms with lighter oxygen atoms in the chemical structure, Bi_2O_2Se lacks the zero-bandgap topological surface states present in Bi_2Se_3[44], resulting in its classification as a typical semiconductor. Nonetheless, Bi_2O_2Se exhibits a significant spin-orbit coupling effect, leading to predicted physical phenomena like Rashba splitting and enhanced magneto transport[42,45,46].

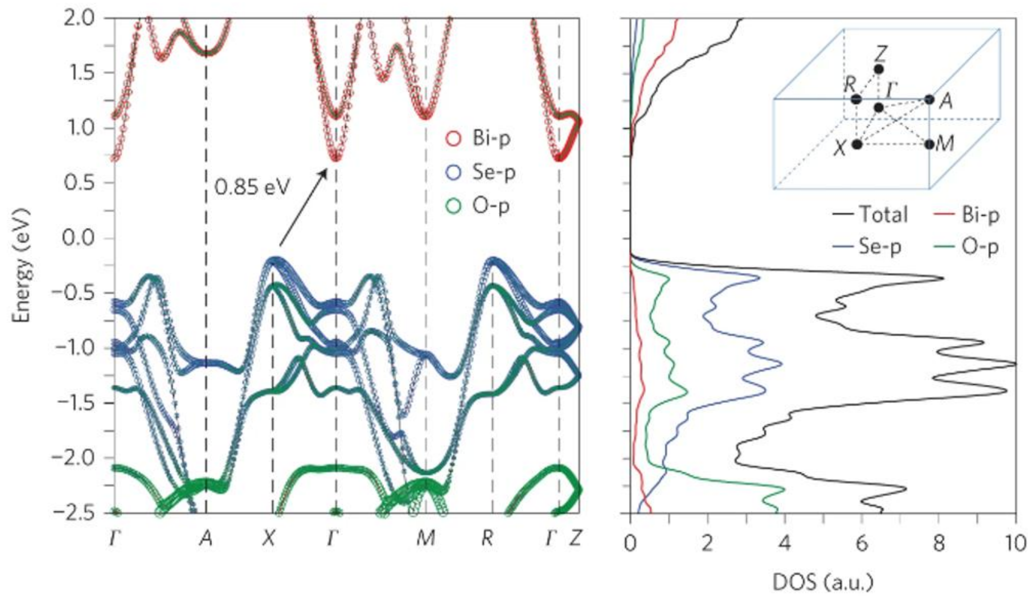

Figure 1.6. Calculated band structure and density of states (DOS) of Bi_2O_2Se with a bandgap of ~0.85 eV. This image has been adapted with permission from Ref.[42] Copyright © 2017, Nature Publishing Group .

According to DFT calculations[42], Bi_2O_2Se possesses an indirect bandgap of approximately 0.8 eV, with the valence band maximum (VBM) located at the X point and the conduction band minimum (CBM) at the Γ point. The conduction band near the Fermi level is predominantly influenced by Bi p orbitals with a blend of some Se p orbitals. The conduction band minimum (CBM) at the Γ point is primarily filled with Bi p_Z orbitals, while other points with lower symmetry, such as M and A, exhibit a combination of Bi py and Se pz orbitals[41]. The highly pronounced band curvature and significant band dispersion observed at the CBM imply a low effective mass and high electron mobility. In contrast, the valence bands are largely shaped by Se and O orbitals, with the Se component being closer to the Fermi level. The in-plane carrier effective mass at the CBM is around 0.14 m_e, which is lower than silicon (0.26 m_e), MoS_2 (0.4–0.6 m_e), and black phosphorus (0.15 m_e), suggesting very high electron mobility. Experimental studies by Wu et al. have shown that the electron mobility of 2D Bi_2O_2Se crystals exceeds 20,000 $cm^2V^{-1}s^{-1}$ at cryogenic temperatures.

Se vacancies are the predominant point defects in Bi_2O_2Se and typically function as electron donors[47–49]. Decreasing Se vacancies by introducing additional selenium can effectively lower the carrier concentration. However, the impact of such vacancies on electron mobility is minimal, as the ionized donor sites are spatially distant from conduction channels, minimizing scattering effects. Excessive selenium addition may lead to undesirable Se-Bi substitutions that could impede carrier mobility[47]. Tong et al. also observed reduced backward electron scattering in Bi_2O_2Se, a phenomenon common in nontrivial Dirac semimetals[50]. Due to its inherently high electron mobility and reduced scattering, It can accommodate very dense current flow[51].

1.5 Thesis Outline

The thesis is structured into the five chapters outlined below.

Chapter 1 provides a concise overview of the 2D materials family. It also touches on the preparation techniques, crystal structure, and electronic band structure of Bi_2O_2Se.

Chapter 2 describes the primary synthesis and characterization methods employed in the thesis for growing and analyzing the synthesized materials. The chapter also delves into the key device fabrication techniques utilized in creating active devices for the electrical characterization of these materials.

Chapter 3 discusses the CVD synthesis of Bi2O2Se nanosheets on F-mica and its characterization . Then it explores the electrical and optoelectronic properties of these nanosheets.

Chapter 4 explores the Metal insulator Transtion charcterisation and its expalination using percolation driven pathway .

Chapter 5 wraps up the thesis by detailing the future course of the research conducted in this thesis.

Bibliography

(1) Castro Neto, A. H.; Guinea, F.; Peres, N. M. R.; Novoselov, K. S.; Geim, A. K. The Electronic Properties of Graphene. *Rev Mod Phys* **2009**, *81* (1), 109–162. https://doi.org/10.1103/REVMODPHYS.81.109

(2) Novoselov, K. S.; Geim, A. K.; Morozov, S. V.; Jiang, D.; Zhang, Y.; Dubonos, S. V.; Grigorieva, I. V.; Firsov, A. A. Electric Field in Atomically Thin Carbon Films. *Science (1979)* **2004**, *306* (5696), 666–669. https://doi.org/10.1126/SCIENCE.1102896.

(3) Schmidt, H.; Giustiniano, F.; Eda, G. Electronic Transport Properties of Transition Metal Dichalcogenide Field-Effect Devices: Surface and Interface Effects. *Chem Soc Rev* **2015**, *44* (21), 7715–7736. https://doi.org/10.1039/C5CS00275C.

(4) Duan, X.; Wang, C.; Pan, A.; Yu, R.; Duan, X. Two-Dimensional Transition Metal Dichalcogenides as Atomically Thin Semiconductors: Opportunities and Challenges. *Chem Soc Rev* **2015**, *44* (24), 8859–8876. https://doi.org/10.1039/C5CS00507H.

(5) Xie, L. M. Two-Dimensional Transition Metal Dichalcogenide Alloys: Preparation, Characterization and Applications. *Nanoscale* **2015**, *7* (44), 18392–18401. https://doi.org/10.1039/C5NR05712D.

(6) Chhowalla, M.; Shin, H. S.; Eda, G.; Li, L. J.; Loh, K. P.; Zhang, H. The Chemistry of Two-Dimensional Layered Transition Metal Dichalcogenide Nanosheets. *Nature Chemistry 2013 5:4* **2013**, *5* (4), 263–275. https://doi.org/10.1038/nchem.1589.

(7) Wang, Q. H.; Kalantar-Zadeh, K.; Kis, A.; Coleman, J. N.; Strano, M. S. Electronics and Optoelectronics of Two-Dimensional Transition Metal Dichalcogenides. *Nature Nanotechnology 2012 7:11* **2012**, *7* (11), 699–712. https://doi.org/10.1038/nnano.2012.193.

(8) Butler, S. Z.; Hollen, S. M.; Cao, L.; Cui, Y.; Gupta, J. A.; Gutiérrez, H. R.; Heinz, T. F.; Hong, S. S.; Huang, J.; Ismach, A. F.; Johnston-Halperin, E.; Kuno, M.; Plashnitsa, V. V.; Robinson, R. D.; Ruoff, R. S.; Salahuddin, S.; Shan, J.; Shi, L.; Spencer, M. G.; Terrones, M.; Windl, W.; Goldberger, J. E. Progress, Challenges, and Opportunities in Two-Dimensional Materials beyond Graphene. *ACS Nano* **2013**, *7* (4), 2898–2926. https://doi.org/10.1021/NN400280C.

(9) Zeng, M.; Xiao, Y.; Liu, J.; Yang, K.; Fu, L. Exploring Two-Dimensional Materials toward the Next-Generation Circuits: From Monomer Design to Assembly Control. *Chem Rev* **2018**, *118* (13), 6236–6296. https://doi.org/10.1021/ACS.CHEMREV.7B00633.

(10) Pi, L.; Li, L.; Liu, K.; Zhang, Q.; Li, H.; Zhai, T.; Pi, L. J.; Li, L.; Liu, K. L.; Zhang, Q. F.; Li, H. Q.; Zhai, T. Y. Recent Progress on 2D Noble-Transition-Metal Dichalcogenides. *Adv Funct Mater* **2019**, *29* (51), 1904932. https://doi.org/10.1002/ADFM.201904932.

(11) Li, Y.; Gu, M.; Zhang, X.; Fan, J.; Lv, K.; Carabineiro, S. A. C.; Dong, F. 2D G-C3N4 for Advancement of Photo-Generated Carrier Dynamics: Status and Challenges. *Materials Today* **2020**, *41*, 270–303. https://doi.org/10.1016/J.MATTOD.2020.09.004.

(12) Pei, Y.; Zhang, X.; Hui, Z.; Zhou, J.; Huang, X.; Sun, G.; Huang, W. Ti3C2TXMXene for Sensing Applications: Recent Progress, Design Principles, and Future Perspectives. *ACS Nano* **2021**, *15* (3), 3996–4017. https://doi.org/10.1021/ACSNANO.1C00248.

(13) Luo, M.; Fan, T.; Zhou, Y.; Zhang, H.; Mei, L.; Luo, M.; Zhou, Y.; Mei, L.; Fan, T.; Zhang, H. 2D Black Phosphorus–Based Biomedical Applications. *Adv Funct Mater* **2019**, *29* (13), 1808306. https://doi.org/10.1002/ADFM.201808306.

(14) Zhang, K.; Feng, Y.; Wang, F.; Yang, Z.; Wang, J. Two Dimensional Hexagonal Boron Nitride (2D-HBN): Synthesis, Properties and Applications. *J Mater Chem C Mater* **2017**, *5* (46), 11992–12022. https://doi.org/10.1039/C7TC04300G.

(15) Prasanna, R.; Gold-Parker, A.; Leijtens, T.; Conings, B.; Babayigit, A.; Boyen, H. G.; Toney, M. F.; McGehee, M. D. Band Gap Tuning via Lattice Contraction and Octahedral Tilting in Perovskite Materials for Photovoltaics. *J Am Chem Soc* **2017**, *139* (32), 11117–11124. https://doi.org/10.1021/JACS.7B04981.

(16) Samal, R.; Sanyal, G.; Chakraborty, B.; Rout, C. S. Two-Dimensional Transition Metal Phosphorous Trichalcogenides (MPX3): A Review on Emerging Trends, Current State and Future Perspectives. *J Mater Chem A Mater* **2021**, *9* (5), 2560–2591. https://doi.org/10.1039/D0TA09752G.

(17) Ohta, T.; Bostwick, A.; Seyller, T.; Horn, K.; Rotenberg, E. Controlling the Electronic Structure of Bilayer Graphene. *Science (1979)* **2006**, *313* (5789), 951–954. https://doi.org/10.1126/SCIENCE.1130681.

(18) Schwierz, F. Graphene Transistors. *Nature Nanotechnology 2010 5:7* **2010**, *5* (7), 487–496. https://doi.org/10.1038/nnano.2010.89.

(19) Jariwala, D.; Sangwan, V. K.; Lauhon, L. J.; Marks, T. J.; Hersam, M. C. Emerging Device Applications for Semiconducting Two-Dimensional Transition Metal Dichalcogenides. *ACS Nano* **2014**, *8* (2), 1102–1120. https://doi.org/10.1021/NN500064S.

(20) Cui, X.; Lee, G. H.; Kim, Y. D.; Arefe, G.; Huang, P. Y.; Lee, C. H.; Chenet, D. A.; Zhang, X.; Wang, L.; Ye, F.; Pizzocchero, F.; Jessen, B. S.; Watanabe, K.; Taniguchi, T.; Muller, D. A.; Low, T.; Kim, P.; Hone, J. Multi-Terminal Transport Measurements of MoS2 Using a van Der Waals Heterostructure Device Platform. *Nature Nanotechnology 2015 10:6* **2015**, *10* (6), 534–540. https://doi.org/10.1038/nnano.2015.70.

(21) Duan, X.; Wang, C.; Pan, A.; Yu, R.; Duan, X. Two-Dimensional Transition Metal Dichalcogenides as Atomically Thin Semiconductors: Opportunities and Challenges. *Chem Soc Rev* **2015**, *44* (24), 8859–8876. https://doi.org/10.1039/C5CS00507H.

(22) Zhang, S.; Yang, J.; Xu, R.; Wang, F.; Li, W.; Ghufran, M.; Zhang, Y. W.; Yu, Z.; Zhang, G.; Qin, Q.; Lu, Y. Extraordinary Photoluminescence and Strong Temperature/Angle-Dependent Raman Responses in Few-Layer Phosphorene. *ACS Nano* **2014**, *8* (9), 9590–9596. https://doi.org/10.1021/NN503893J.

(23) Kumar Shringi, A.; Kumar, R.; Yan, F. Recent Advances in Bismuth Oxychalcogenide Nanosheets for Sensing Applications. *Nanoscale* **2024**, *16* (22), 10551–10565. https://doi.org/10.1039/D4NR00821A.

(24) Hossain, M. T.; Jena, T.; Giri, P. K. Recent Advances in the Growth Strategies, Multifunctional Properties, and Emerging Applications of Two-Dimensional Non-van Der Waals Bismuth Oxychalcogenides and Prospective Heterostructures. *Small Struct* **2024**, *5* (8), 2300511. https://doi.org/10.1002/SSTR.202300511.

(25) Ghosh, T.; Samanta, M.; Vasdev, A.; Dolui, K.; Ghatak, J.; Das, T.; Sheet, G.; Biswas, K. Ultrathin Free-Standing Nanosheets of Bi2O2Se: Room Temperature Ferroelectricity in Self-Assembled Charged Layered Heterostructure. *Nano Lett* **2019**, *19* (8), 5703–5709. https://doi.org/10.1021/ACS.NANOLETT.9B02312.

(26) Khan, U.; Nairan, A.; Khan, K.; Li, S.; Liu, B.; Gao, J.; Khan, U.; Nairan, A.; Gao, J.; Khan, K.; Li, S.; Liu, B. Salt-Assisted Low-Temperature Growth of 2D Bi2O2Se with Controlled Thickness for Electronics. *Small* **2023**, *19* (10), 2206648. https://doi.org/10.1002/SMLL.202206648.

(27) Yu, J.; Li, J.; Zhang, W.; Chang, H. Synthesis of High Quality Two-Dimensional Materials via Chemical Vapor Deposition. *Chem Sci* **2015**, *6* (12), 6705–6716. https://doi.org/10.1039/C5SC01941A.

(28) Ju-Xia Yi, S.; Zhang, R.-Z.; Zhang, Y.-Y.; Tao, H.; Wang, T.; Li, D.; Xing, J.; Li, G.; Tao, H. Y.; Wang, T. L.; Li, D. Y.; Xing, J.; Li, G. W. Preparation, Properties, and Applications of Bi2O2Se Thin Films: A Review. *Journal of Semiconductors* **2023**, *44* (3), 031001. https://doi.org/10.1088/1674-4926/44/3/031001.

(29) Sun, Y.; Zhang, J.; Ye, S.; Song, J.; Qu, J.; Sun, Y.; Zhang, J.; Ye, S.; Song, J.; Qu, J. Progress Report on Property, Preparation, and Application of Bi2O2Se. *Adv Funct Mater* **2020**, *30* (49), 2004480. https://doi.org/10.1002/ADFM.202004480.

(30) Wu, J.; Tan, C.; Tan, Z.; Liu, Y.; Yin, J.; Dang, W.; Wang, M.; Peng, H. Controlled Synthesis of High-Mobility Atomically Thin Bismuth Oxyselenide Crystals. *Nano Lett* **2017**, *17* (5), 3021–3026. https://doi.org/10.1021/acs.nanolett.7b00335.

(31) Li, J.; Wang, Z.; Wen, Y.; Chu, J.; Yin, L.; Cheng, R.; Lei, L.; He, P.; Jiang, C.; Feng, L.; He, J. High-Performance Near-Infrared Photodetector Based on Ultrathin Bi2O2Se Nanosheets. *Adv Funct Mater* **2018**, *28* (10), 1706437. https://doi.org/10.1002/ADFM.201706437.

(32) Wu, Z.; Liu, G.; Wang, Y.; Yang, X.; Wei, T.; Wang, Q.; Liang, J.; Xu, N.; Li, Z.; Zhu, B.; Qi, H.; Deng, Y.; Zhu, J.; Wu, Z.; Liu, G.; Wang, Y.; Yang, X.; Wei, T.; Wang, Q.; Liang, J.; Xu, N.; Li, Z.; Zhu, B.; Qi, H.; Deng, Y.; Zhu, J. Seed-Induced Vertical Growth of 2D Bi2O2Se Nanoplates by Chemical Vapor Transport. *Adv Funct Mater* **2019**, *29* (50), 1906639. https://doi.org/10.1002/ADFM.201906639.

(33) Park, J. C.; Kim, S.; Choi, H.; Jung, Y.; Oh, I.; Hwang, J. B.; Lee, S. Growth of Multilayer WSe2/Bi2O2Se Heterostructures for Photodetection without Lithography. *Cryst Growth Des* **2023**, *23* (4), 2092–2098. https://doi.org/10.1021/ACS.CGD.2C01029.

(34) Song, Y.; Li, Z.; Li, H.; Tang, S.; Mu, G.; Xu, L.; Peng, W.; Shen, D.; Chen, Y.; Xie, X.; Jiang, M. Epitaxial Growth and Characterization of High Quality Bi2O2Se Thin Films on SrTiO3 Substrates by Pulsed Laser Deposition. *Nanotechnology* **2020**, *31* (16), 165704. https://doi.org/10.1088/1361-6528/AB6686.

(35) Liang, Y.; Chen, Y.; Sun, Y.; Xu, S.; Wu, J.; Tan, C.; Xu, X.; Yuan, H.; Yang, L.; Chen, Y.; Gao, P.; Guo, J.; Peng, H.; Liang, Y.; Xu, S.; Wu, J.; Tan, C.; Gao, P.; Peng, H.; Chen, Y.; Yang, L.; Sun, Y.; Xu, X.; Guo, J.; Yuan, H. Molecular Beam Epitaxy and Electronic Structure of Atomically Thin Oxyselenide Films. *Advanced Materials* **2019**, *31* (39), 1901964. https://doi.org/10.1002/ADMA.201901964.

(36) Zhou, X.; Liang, Y.; Fu, H.; Zhu, R.; Wang, J.; Cong, X.; Tan, C.; Zhang, C.; Zhang, Y.; Wang, Y.; Xu, Q.; Gao, P.; Peng, H.; Zhou, X.; Liang, Y.; Wang, J.; Cong, X.; Tan, C.; Zhang, C.; Zhang, Y.; Wang, Y.; Xu, Q.; Peng, H.; Fu, H.; Zhu, R.; Gao, P. Step-Climbing Epitaxy of Layered Materials with Giant Out-of-Plane Lattice Mismatch. *Advanced Materials* **2022**, *34* (42), 2202754. https://doi.org/10.1002/ADMA.202202754.

(37) Wang, J.; Huang, J.; Kaplan, D.; Zhou, X.; Tan, C.; Zhang, J.; Jin, G.; Cong, X.; Zhu, Y.; Gao, X.; Liang, Y.; Zuo, H.; Zhu, Z.; Zhu, R.; Stern, A.; Liu, H.; Gao, P.; Yan, B.; Yuan, H.; Peng, H. Even-Integer Quantum Hall Effect in an Oxide Caused by a Hidden Rashba Effect. *Nature Nanotechnology 2024* **2024**, 1–8. https://doi.org/10.1038/s41565-024-01732-z.

(38) Zhang, C.; Wu, J.; Sun, Y.; Tan, C.; Li, T.; Tu, T.; Zhang, Y.; Liang, Y.; Zhou, X.; Gao, P.; Peng, H. High-Mobility Flexible Oxyselenide Thin-Film Transistors Prepared by a Solution-Assisted Method. *J Am Chem Soc* **2020**, *142* (6), 2726–2731. https://doi.org/10.1021/JACS.9B11668.

(39) Dang, L. Y.; Liu, M.; Wang, G. G.; Zhao, D. Q.; Han, J. C.; Zhu, J. Q.; Liu, Z. Organic Ion Template-Guided Solution Growth of Ultrathin Bismuth Oxyselenide with Tunable Electronic Properties for Optoelectronic Applications. *Adv Funct Mater* **2022**, *32* (31), 2201020. https://doi.org/10.1002/ADFM.202201020.

(40) Xie, H.; Liu, M.; You, B.; Luo, G.; Chen, Y.; Liu, B.; Jiang, Z.; Chu, P. K.; Shao, J.; Yu Xie, X.-F. H.; Luo, G.; Chen, Y.; Xie, H.; Jiang, Z.; Liu, M.; Liu, B.; You, B.; Shao, J.; Yu, X.; Chu, P. K. Biodegradable Bi2O2Se Quantum Dots for Photoacoustic Imaging-Guided Cancer Photothermal Therapy. *Small* **2020**, *16* (1), 1905208. https://doi.org/10.1002/SMLL.201905208.

(41) Ding, X.; Li, M.; Chen, P.; Zhao, Y.; Zhao, M.; Leng, H.; Wang, Y.; Ali, S.; Raziq, F.; Wu, X.; Xiao, H.; Zu, X.; Wang, Q.; Vinu, A.; Yi, J.; Qiao, L. Bi2O2Se: A Rising Star for Semiconductor Devices. *Matter* **2022**, *5* (12), 4274–4314. https://doi.org/10.1016/J.MATT.2022.11.005.

(42) Wu, J.; Yuan, H.; Meng, M.; Chen, C.; Sun, Y.; Chen, Z.; Dang, W.; Tan, C.; Liu, Y.; Yin, J.; Zhou, Y.; Huang, S.; Xu, H. Q.; Cui, Y.; Hwang, H. Y.; Liu, Z.; Chen, Y.; Yan, B.; Peng, H. High Electron Mobility and Quantum Oscillations in Non-Encapsulated Ultrathin Semiconducting Bi2O2Se. *Nature Nanotechnology 2017 12:6* **2017**, *12* (6), 530–534. https://doi.org/10.1038/nnano.2017.43.

(43) Wei, Q.; Li, R.; Lin, C.; Han, A.; Nie, A.; Li, Y.; Li, L. J.; Cheng, Y.; Huang, W. Quasi-Two-Dimensional Se-Terminated Bismuth Oxychalcogenide (Bi2O2Se). *ACS Nano* **2019**, *13* (11), 13439–13444. https://doi.org/10.1021/ACSNANO.9B07000.

(44) Li, T.; Peng, H. 2D Bi2O2Se: An Emerging Material Platform for the Next-Generation Electronic Industry. *Acc Mater Res* **2021**, *2* (9), 842–853. https://doi.org/10.1021/ACCOUNTSMR.1C00130.

(45) Meng, M.; Huang, S.; Tan, C.; Wu, J.; Jing, Y.; Peng, H.; Xu, H. Q. Strong Spin–Orbit Interaction and Magnetotransport in Semiconductor Bi2O2Se Nanoplates. *Nanoscale* **2018**, *10* (6), 2704–2710. https://doi.org/10.1039/C7NR08874D.

(46) Wu, M.; Zeng, X. C. Bismuth Oxychalcogenides: A New Class of Ferroelectric/Ferroelastic Materials with Ultra High Mobility. *Nano Lett* **2017**, *17* (10), 6309–6314. https://doi.org/10.1021/ACS.NANOLETT.7B03020

(47) Fu, H.; Wu, J.; Peng, H.; Yan, B. Self-Modulation Doping Effect in the High-Mobility Layered Semiconductor Bi2O2Se. *Phys Rev B* **2018**, *97* (24). https://doi.org/10.1103/PhysRevB.97.241203.

(48) Li, H.; Xu, X.; Zhang, Y.; Gillen, R.; Shi, L.; Robertson, J. Native Point Defects of Semiconducting Layered Bi2O2Se. *Scientific Reports 2018 8:1* **2018**, *8* (1), 1–8. https://doi.org/10.1038/s41598-018-29385-8.

(49) Wu, J.; Qiu, C.; Fu, H.; Chen, S.; Zhang, C.; Dou, Z.; Tan, C.; Tu, T.; Li, T.; Zhang, Y.; Zhang, Z.; Peng, L. M.; Gao, P.; Yan, B.; Peng, H. Low Residual Carrier Concentration and High Mobility in 2D Semiconducting Bi 2 O 2 Se. *Nano Lett* **2019**, *19* (1), 197–202. https://doi.org/10.1021/ACS.NANOLETT.8B03696

(50) Tong, T.; Zhang, M.; Chen, Y.; Li, Y.; Chen, L.; Zhang, J.; Song, F.; Wang, X.; Zou, W.; Xu, Y.; Zhang, R. Ultrahigh Hall Mobility and Suppressed Backward Scattering in Layered

Semiconductor Bi2O2Se. *Appl Phys Lett* **2018**, *113* (7), 72106. https://doi.org/10.1063/1.5042727/36581.

(51) Quhe, R.; Liu, J.; Wu, J.; Yang, J.; Wang, Y.; Li, Q.; Li, T.; Guo, Y.; Yang, J.; Peng, H.; Lei, M.; Lu, J.; Wu, J.; Yuan, H.; Meng, M.; Chen, C.; Sun, Y.; Chen, Z.; Dang, W.; Tan, C.; Liu, Y.; Yin, J.; Zhou, Y.; Huang, S.; Xu, H. Q.; Cui, Y.; Hwang, H. Y.; Liu, Z.; Chen, Y.; Yan, B.; Peng, H. High-Performance Sub-10 Nm Monolayer Bi2O2Se Transistors. *Nanoscale* **2019**, *11* (2), 532–540. https://doi.org/10.1039/C8NR08852G.

Chapter 2

Experimental Techniques

In this chapter, we will cover the experimental and characterization techniques used for material synthesis, device fabrication, and electrical measurements in this thesis. We will start by discussing the use of APCVD in the synthesis of Bi_2O_2Se nanosheets. Subsequently, we will delve into structural characterization techniques such as HRTEM, Raman Spectroscopy, and AFM. Following that, we will explore photolithography and PVD, which are used in device fabrication.

2.1 Material Synthesis

2.1.1 Chemical Vapor Deposition

Chemical vapor deposition (CVD) is a versatile method extensively used for growing various two-dimensional (2D) materials and is considered the most promising approach for large-scale production of monolayers over a large area[1]. It is a thermodynamic process where one or more volatile precursors react or decompose on the surface of the substrate to create a thin film. The process involves several steps, including the mass transport of precursors in the gas phase, diffusion through the boundary layer, adsorption of precursors on the substrate, surface diffusion to the growth sites, surface chemical reaction to form a thin film, desorption of byproducts, and removal of the byproducts from the reaction chamber[2]. The characteristics of 2D materials heavily

rely on factors such as their size, morphology, defects phase, and any interfaces, they contain. These aspects can be managed through strategic design and precise adjustment of the CVD growth processes. Therefore, comprehending the fundamental mechanisms of CVD growth, including how variables like precursor material, substrate type, pressure, and temperature impact mass and

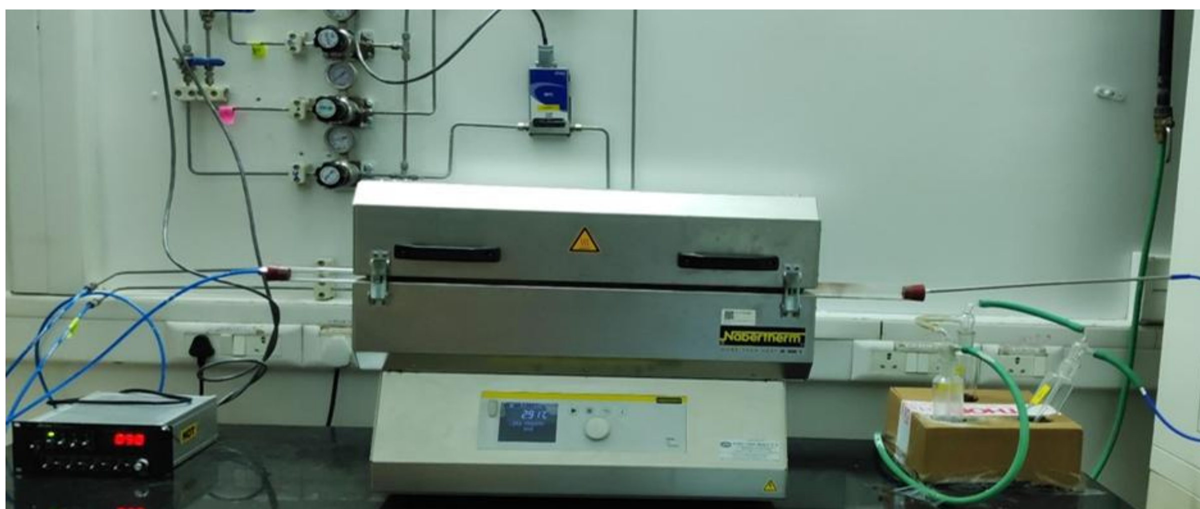

Figure 2.1 : Image of our Homebuilt CVD system used for synthesizing Bi_2O_2Se nanosheets.

heat flow, interface reactions, and consequently the material's growth, is crucial[3]. The impact of certain general parameters is outlined here.

Precursor

Solid precursors such Bi_2O_3 and Bi_2Se_3 are employed in the synthesis of Bi_2O_2Se. It is essential to maintain precise control over temperature when working with solid precursors due to their sensitivity to temperature variations. On the other hand, gaseous precursors offer superior control

over the quantity of reactant molecules, with the quality of the precursor playing a critical role in determining the sample purity.

Temperature

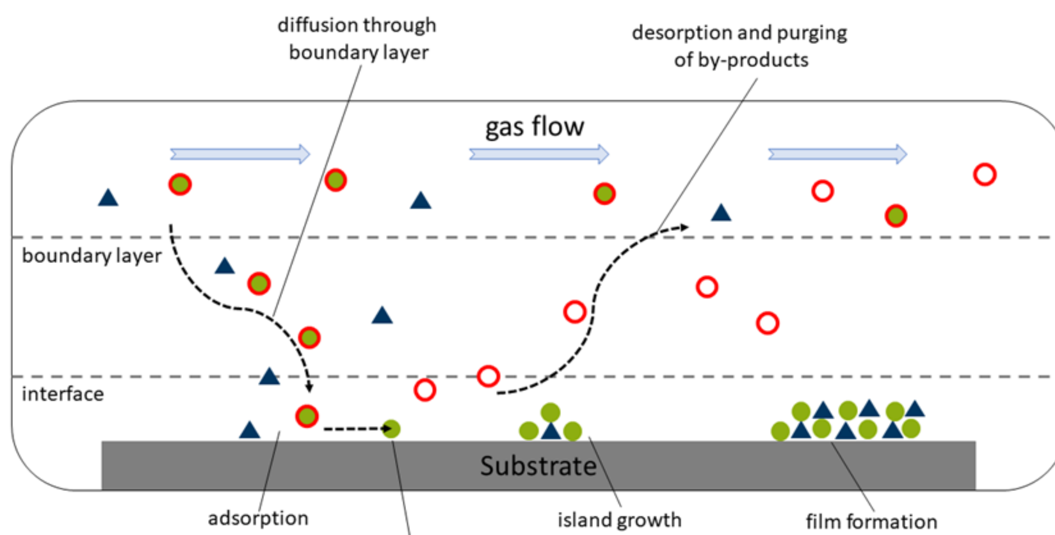

Figure 2.2 : Schematic of a CVD process. The figure has been adapted with permission from Reference [28] .

Temperature plays a crucial role in determining the uniformity and composition of 2D films. Even a slight variation in temperature can lead to significant changes in the saturation pressure of solid precursors in their vapor phase, impacting the growth process. Moreover, temperature regulates the reaction rate by influencing the mass transport of reactant species and reactions occurring at the substrate surface. As the temperature rises, the proportion of precursors in the gas phase also

increases. Consequently, growth becomes diffusion-limited at higher temperatures, while mass transport becomes the limiting factor at lower temperatures[3].

Pressure

The gas flow is influenced by the pressure within the reaction chamber. Opting for lower pressure levels allows for better control of the reaction due to higher reactant species velocity and lower precursor concentration. Monolayer growth is more favorable under reduced pressure conditions. Second-layer nucleation primarily takes place at grain boundaries when pressure is low. Conversely, higher pressures lead to arbitrary nucleation, resulting in a mix of monolayer and multilayer growth[3].

In this thesis, the CVD synthesis was conducted using a homebuilt atmospheric pressure CVD system. The setup comprises a quartz tube housed within a Nabertherm split zone furnace (Figure 2.1). The tube's inlet is connected to an Alicat mass flow controller (MFC), while the outlet is linked to a series of bubblers. Argon and Nitrogen served as carrier gases, with their flow rates regulated by the MFC. Any volatile byproducts were eliminated through the exit of the system. Precursors and substrates were positioned on a ceramic boat inside the quartz tube.

2.2 Characterization techniques

2.2.1 Raman Spectroscopy

Raman spectroscopy is a powerful and non-destructive analytical technique used to provide information about molecular vibrations, crystal structures, and material compositions. This method employs the concept of Raman scattering, which was identified by Sir C.V. Raman in 1928, and led to him receiving the Nobel Prize for Physics in 1930[4]. When light strikes a material, it is either absorbed, reflected, or scattered[5]. If the scattered light matches the frequency of the incident light, there is no energy transfer, resulting in an elastic collision process known as Rayleigh scattering. Usually, this is quite intense. The light that remains scatters weakly, displaying frequencies distinct from the incoming light in a phenomenon called Raman scattering. Antistokes scattering occurs with higher scattered frequencies, while Stokes scattering occurs with lower frequencies. This process involves energy transfer through inelastic scattering, providing insights into the vibrational modes of the system. The brightness of the scattered light increases with the quantity of scattering molecules. At standard room temperature when in thermal balance, the majority of molecules are in their lowest energy level, also known as the ground state. As a result, Stokes scattering tends to have a higher intensity compared to Antistokes scattering, resulting in Raman scattered light primarily being Stokes scattered. Raman spectroscopy is commonly employed in the analysis of 2D materials to glean insights into their vibrational characteristics, layer count, structural irregularities, doping levels, and strain effects[4] . In this thesis, we have employed raman spectroscopy to characterize our as grown samples. Raman spectroscopy was performed using a laser with a wavelength of 632.8 nm on a Raman Microscope (LabRAM HR) equipped with a 50X objective lens.

2.2.2 Atomic Force Microscopy

Atomic Force Microscopy (AFM) is a robust scanning probe microscopy method employed to acquire topographic images of the surfaces of samples. The AFM was invented in 1985 by G. Binnig and C. F. Quate at IBM through the amalgamation of the fundamentals of the scanning tunneling microscope and the stylus profilometer[6]. AFM setup comprises the subsequent elements: a micro-cantilever equipped with a probe, a micro-cantilever motion sensing unit, a feedback mechanism for tracking micro-cantilever movements, a piezoelectric ceramic scanning tool for sample scanning, and a computer-managed system for image acquisition, presentation, and analysis. It examines the surface structure and properties of the sample through the detection of extremely subtle interatomic interactions between the sample surface and the probe tip[7]. Figure 2.2 displays the schematic diagram of AFM working Principles. The AFM measurement entails scanning the surface with a sharp tip connected to a flexible cantilever. The interaction of atomic forces between the surface and the tip induces deflection in the tip. This deflection is quantified by directing a laser beam onto the reflective-coated tip of the flexible cantilever and detecting the reflected beam with a position-sensitive photodetector. The position-sensitive photodetector comprises several segments, and the placement of the laser spot on these segments offers insights into the deflection of the cantilever. By tracking the laser spot's position on the photodetector, it is possible to ascertain the displacement of the cantilever. It can be utilized in either tapping mode

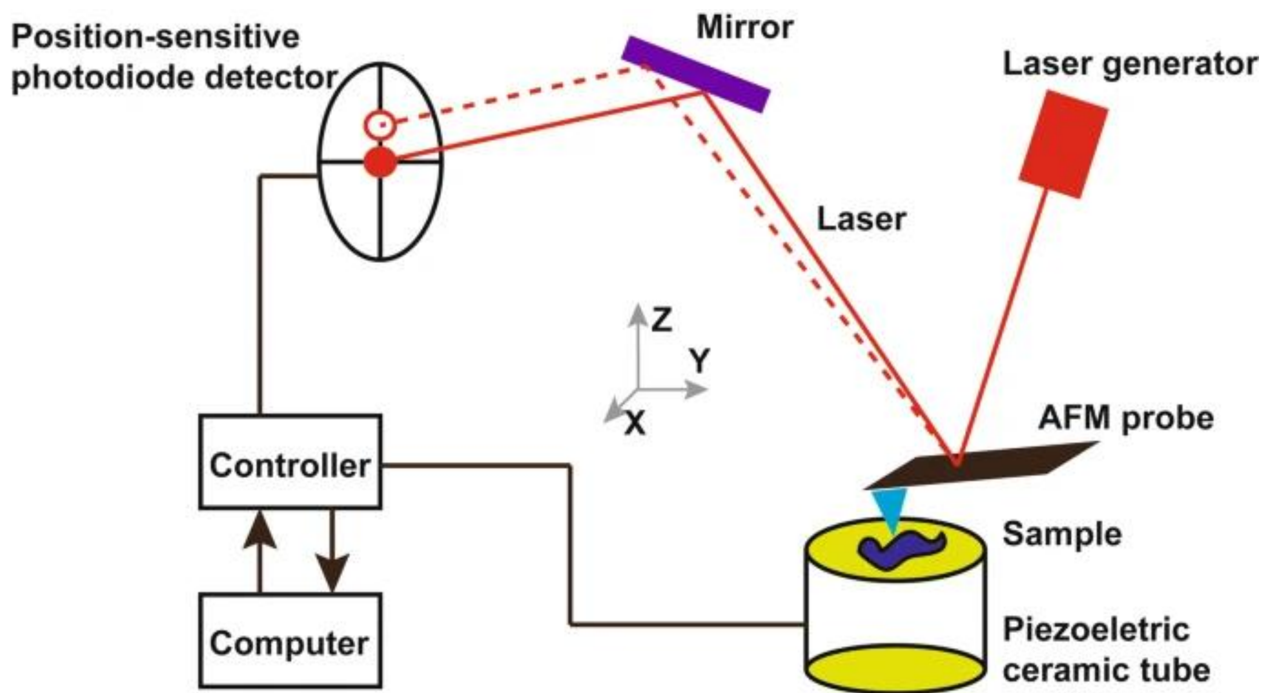

Figure 2.3 Schematic diagram of AFM Working Principles. The figure has been adapted with permission from Reference.[7]

or contact mode[8]. AFM provides atomic-level resolution and enables 3D topographic imaging, offering varying levels of detailed information based on the specific AFM tip utilized. With the advancement of new sophisticated AFM modes, information on different properties such as conductivity, surface potential, modulus, adhesion, permittivity, reflection, absorption, etc. can also be acquired[9,10]. Keysight 5500 AFM is used in this thesis to perform AFM measurements to determine the thickness and surface roughness of our samples.

2.2.3 Scanning Electron Microscopy

Scanning Electron Microscopy (SEM) is a powerful analytical tool widely used in materials science for imaging and analyzing the surface morphology and composition of materials at nanometer to micrometer scales. The SEM utilizes electron beams to capture images of sample surfaces with nanometer-scale resolution[11]. Electrons generated from an electron gun are organized into a beam and then directed to a specific spot through the use of electromagnetic fields and lenses. When an electron beam interacts with a specimen, it can produce different types of electrons such as backscattered or reflected electrons (BSEs), secondary electrons (SEs), Auger electrons, X-ray photons, and more[12]. Most SEM systems come with secondary electron and backscattered electron detectors, with the X-ray detector located externally to the microscope. SEs and BSEs are utilized to image the surface of the sample, while the X-ray signal is employed for analyzing the chemical composition[13,14]. SEs originate from the uppermost few layers of the sample, with a thickness of approximately 20 nm, and they localize at the point where primary incident electrons strike, enabling the provision of information on sample morphology. SEs typically exhibit low energy levels around 50 eV and can generate images with a resolution of 1 nm. In contrast, BSEs resulting from elastic scattering tend to originate from greater depths within the sample. The intensity of BSEs, which are generated by elastic scattering from atoms, varies based on the Z value of the elements in the specimen, facilitating the creation of contrast images for samples with diverse elemental distributions throughout the space. Auger electrons are released when an incoming electron beam generates electron vacancies in the innermost shells, such as K, L, M, and so on, which are subsequently filled by electrons from the outermost shell. As this

transition occurs, the resulting X-ray energy is passed on to another electron, which is then emitted. This emitted electron is known as the Auger electron. Auger electron microscopy utilizes these electrons to examine thin films and coatings. The X-ray signal obtained is generated from the depth of the specimen when the incident electron beam displaces the innermost shell electrons, creating vacancies that are filled by outer shell electrons, leading to the emission of characteristic X-ray signals. These distinct X-rays can be analyzed for elemental composition using either Wavelength-dispersive X-ray spectroscopy (WDS) or Energy-dispersive X-ray spectroscopy (EDS). The Ultra Ziess Plus microscope, along with the Oxford Inca EDX detector, was utilized in this thesis work.

2.2.4 Transmission Electron Microscopy

In Transmission Electron Microscopy (TEM), passing an electron beam through a thin sample leads to the formation of the sample's image under observation. Electrons with wavelengths 10^5 times shorter than visible light can reveal details as small as 0.05nm. TEM can be utilized in either image mode or diffraction mode[15]. Image mode yields details on the microstructure, while diffraction mode provides insights into the crystalline structure of the specimen. Electrons passing through the sample may either pass through without interaction or become diffracted based on the interaction. Detectors positioned at different angles capture these electrons. The higher the atomic number, the greater the number of scattered electrons. The Bright-Field (BF) method captures the fewest scattered electrons, while the High-Angle Annular Dark-Field (HAADF) detector gathers electrons scattered at wider angles. The HAADF image, also referred to as the Z-contrast image,

exhibits image contrast directly linked to variations in thickness or mass. Transmission Electron Microscopy (TEM) operates in two main modes: parallel beam and converging beam mode. In parallel beam mode, broad and parallel beams illuminating the sample generate high-resolution TEM (HRTEM) images. In converging mode, small converging beams sweep across the sample, recording scanning TEM (STEM) images[16]. Aberrations such as knock-on damage and image distortion are drawbacks of TEM. However, the introduction of aberration-corrected TEM, operating at lower acceleration voltages, has effectively addressed these issues[17]. TEM is widely employed for the analysis of 2D materials, offering the possibility of achieving atomic resolution imaging and revealing detailed information about the crystalline structure. High-resolution transmission electron microscope JEOL JEM 2200FS from Japan, which is fitted with a 200 KeV field emission gun (FEG) and an in-column energy filter (Omega filter), was utilized in this thesis for structural characterization of Bi_2O_2Se nanosheets.

2.3 Device Fabrication

2.3.1 Photolithography

Lithography methods are fundamental to semiconductor manufacturing, playing a crucial part in creating cutting-edge electronic devices. Photolithography is the predominant technique in the

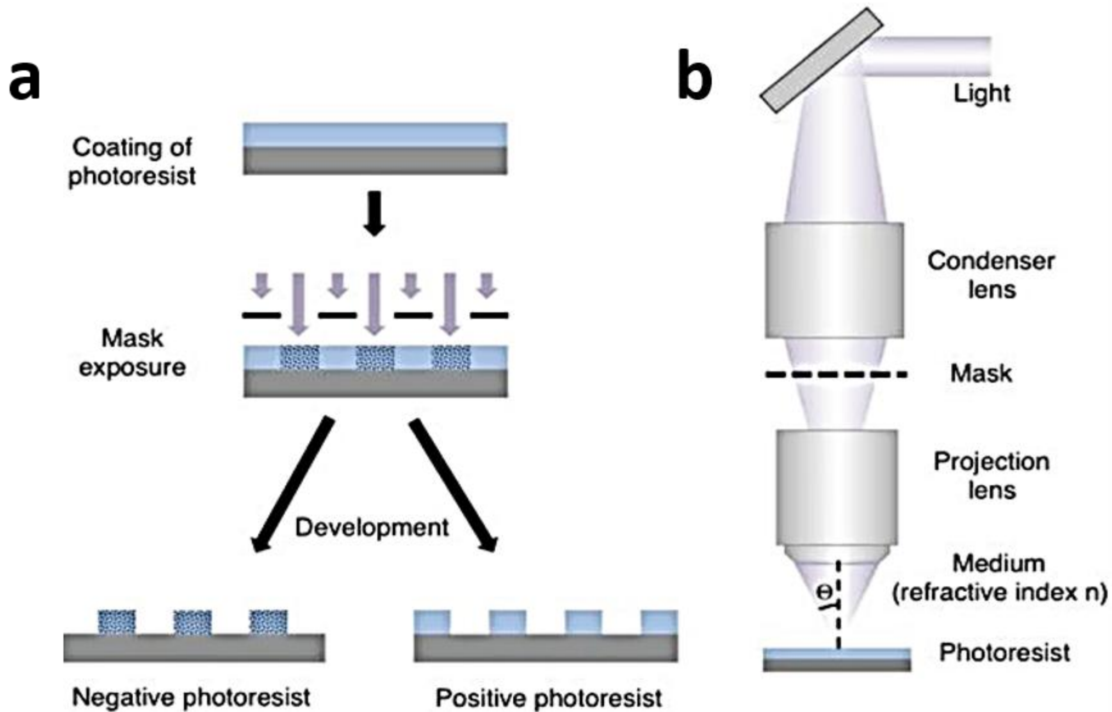

Figure 2.4 : (a) Illustration of a mask photolithographic process (contact/proximity) and (b) an optical projection system. The figure has been adapted with permission from Barrio et al [29]

semiconductor sector due to its high efficiency. This process utilizes a polymer called photoresist, a compound that, when exposed to light, undergoes a chemical transformation, determining whether it can be washed away in a developer solution[18]. There are two types of photoresists: positive and negative. In positive photoresists, the light-exposed regions are soluble and are

removed after developing. Conversely, in negative photoresists, the process is reversed. The exposed regions become insoluble, and the remaining portion is removed. When using a positive photoresist, the pattern on the substrate matches that of the mask. In contrast, when using a negative photoresist, the pattern formed on the substrate is the reverse of the mask. In optical lithography, light can be exposed using two methods: shadow printing and projection printing. In shadow printing, the mask either directly contacts the substrate or is in close proximity. Shadow printing can achieve a high resolution of approximately 1μm, but may face issues caused by dust particles on the mask or defects on the substrate. All device fabrications conducted in this thesis are implemented using the projection printing method. In this technique, the pattern from the mask is projected onto a substrate positioned centimeters away from the mask. The minimum line width (W) of the resulting pattern on the substrate is determined by $W = \lambda / NA$. Where λ represents the light wavelength and NA denotes the numerical aperture which is defined as $NA = n\sin\theta$. Here, n refers to the refractive index of the imaging medium (air) and θ signifies the half angle of the cone of light that converges to form a point image on the substrate. The depth of focus (DOF), a critical element in projection printing that measures how far the image plane can be displaced while still maintaining a sharp feature size, is expressed by $DOF = \lambda / NA^2$. To achieve higher resolution and a larger depth of focus, it is important to select an optimal value for NA.

2.3.2 Physical Vapor Deposition

Deposition methods are key in the fabrication of nanodevices and the deposition of thin films for various applications. These methods facilitate the precise application of materials onto surfaces, facilitating the production of thin films with specific properties and structures. When combined with lithographic methods, one can fabricate functional devices ranging from the nanoscale to the macro scale. Thermal vapor deposition (TVD) and magnetron sputter deposition stand out as commonly employed techniques among the various available deposition methods

2.3.2.1 Thermal Evaporation

Thermal evaporation is a technique within the realm of Physical Vapor Deposition (PVD) utilized to deposit thin layers of various materials onto a surface. In thermal vapor deposition, a solid target is heated until it melts and evaporates. The evaporation of the target leads to the generation of vapor pressure. This process occurs within a vacuum chamber since a low vacuum promotes the vapor's ascent. The evaporated substance transforms into a vapor stream that can flow freely without interacting or scattering against other atoms due to the vacuum, ultimately adhering to the substrate's surface. Its significant benefit is its capability to coat various materials like metals, organic compounds, and inorganic compounds with low vaporization points[19]. Many of these materials do not adhere well to commonly used glass or silicon substrates. An adhesive layer is typically created using a thin layer of Chromium. By fine-tuning deposition parameters like temperature, pressure, and deposition rate, precise management of film thickness can be attained. This flexibility facilitates the deposition of a range of materials, making it possible to create

functional films for a variety of applications. Gold was utilized as the contact material in this thesis, accompanied by Chromium serving as the adhesion layer.

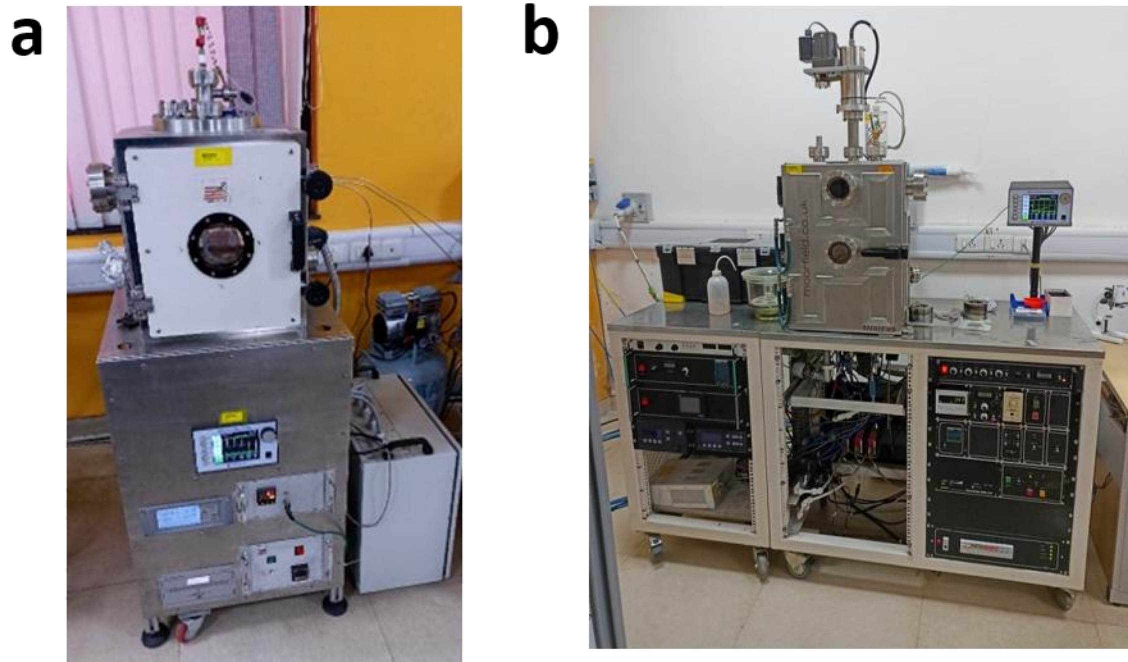

Figure 2.5: (a) Photograph of TVD and (b) Sputtering setup we used

2.3.2.2 Sputtering

Magnetron sputtering is a widely used PVD method increasingly used in industrial settings, especially in semiconductor manufacturing and vacuum deposition. This adaptable and advancing technology provides various benefits over alternative sputtering methods, such as the capability to plasma-sputter any material for deposition[20]. When bombarded by high-energy gas plasma, a sputtering target emits high-energy microparticles. The substrates are placed in a vacuum chamber

containing inert gas. These microparticles, emitted from the target materials, deposit onto the substrate, creating a thin layer of the material. This technique is utilized for coating both metals and oxides. In this thesis, Moorfield minilab magnetron sputter coating system in DC Sputtering mode is used to deposit metals like Palladium, Gold, Titanium, and platinum, and insulators like Silicon Nitride Si_3N_4 are deposited using RF sputtering mode.

2.3.3 Reactive Ion Etching

Reactive Ion Etching (RIE) represents a sophisticated plasma-based etching technique that finds widespread applications in the microfabrication of electronic devices. This method facilitates accurate material patterning at the nanometer scale[21]. It involves the use of chemically reactive plasma to etch materials. In contrast to wet etching techniques, RIE can generate anisotropic etch profiles and maintain satisfactory selectivity across a range of conditions including electrode geometry, radio frequency (RF) power, pressure, gas flow rate, and composition. RIE varies from sputter etching due to its incorporation of a chemical reaction that enhances selectivity and boosts the etching rates[22]. During a standard RIE procedure, gases are injected into the reaction chamber. RF energy is used to ionize the gas, leading to the acceleration of ionized molecules toward the surface of the substrate. Subsequently, a combination of mechanical and chemical interactions facilitates the removal of the topmost layer of material. In addition to ion bombardment, a radical substrate reaction occurs simultaneously. A volatile product is also generated by the bonding of

the radical with the substrate, and subsequently extracted by the vacuum pump[23]. This process is performed under low pressure.

Different designs can be formed by carefully shielding the intended regions with an etch mask

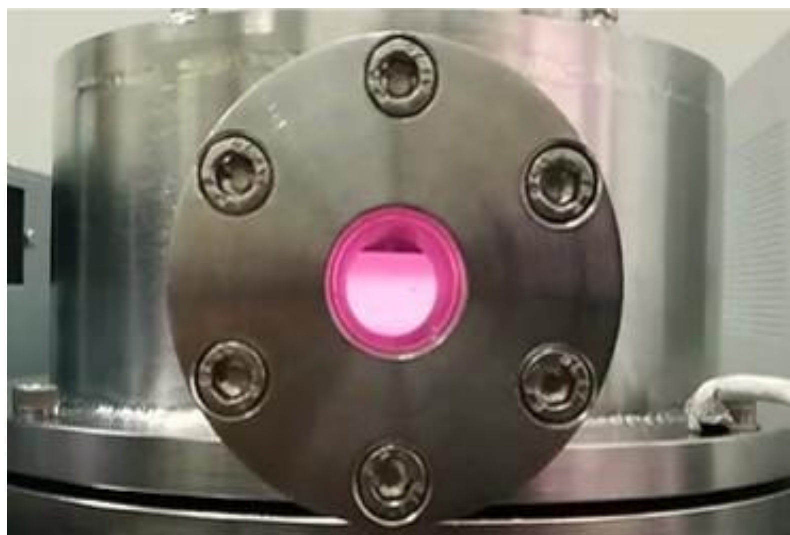

Figure 2.6 : Image of our Homebuilt RIE system used for etching.

during the etching process. Generally, the photoresist is used as an etch mask. Silicon nitride (Si_3N_4), Silicon dioxide (SiO_2), as well as metals like chromium (Cr) or aluminum (Al) are alternative materials utilized as etch masks[24]. RIE typically exhibits elevated selectivity. Optimal etching necessitates a significant quantity of low-energy ions and reduced pressure. However, this leads to a diminished etching speed as part of the balancing act for favorable selectivity, consistency, and etch profile[23]. In this thesis, RIE is used to etch h-BN for making edge contacts and also to etch platinum.

2.3.4 Wire Bonding

Wire bonding serves as a commonly utilized and dependable packaging technology within the semiconductor and microelectronics sectors. It holds a significant function in linking integrated circuit (IC) chips to power sources and enabling signal distribution among IC chips and microelectronic devices[25–27]. Wire bonding serves as a critical methodology in this thesis for creating electrical links between our microdevices and PCB. The PCB aids in placing the samples on holders for conducting low temperature measurements. In our wire bonding procedures, we employ wedge bonding, a technique that utilizes ultrasonic energy to facilitate the cold welding of metals. We have used Hybond model 626 wire bonder for Wire bonding.

Figure 2.7: Photograph of our Hybond model 626 wire bonder.

2.4 Interfacing of Instruments

We have interfaced our Polytronic electromagnet which can generate Magnetic built upto (-1.5T to 1.5 T). For this we have connected magnet power supply to NI PCI 6221 breakout box. Which is connected to NI PCI 6221 DAQ card that is installed in computer. Then we make a LabVIEW Program to control the magnet . For doing Low temperature Magnetotransport measurement we have interface a Lakeshore Cernox censor of our CCR and made some LabVIEW program to interface an electromagnet and a closed cycle refrigerator.

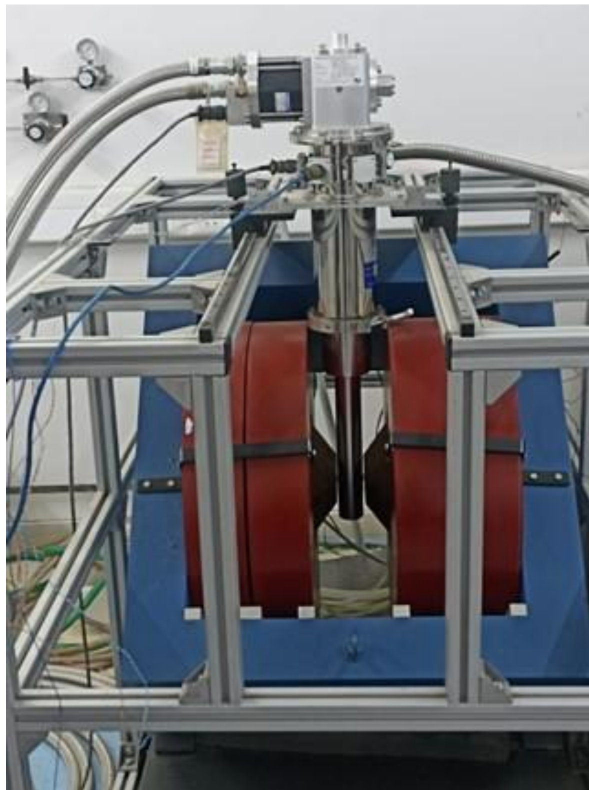

Figure 2.8: Photograph of our Magneto transport Set up .

For performing electrical measurements under Vacuum conditions, we have made one Insert. We paste our sample on PCB using silver paste and do wire bonding to connect our device with gold Pads of PCB. we mount the PCB on Female pin header. It has an Oxygen Free Copper Sample holder. which is connected to Stainless Steel Rod. It has Outer Vacuum Jacket Made of Nonmagnetic Stainless Steel. Coax Wire are used. It has 8 electrical connection. To Connect our SMU with our Insert I have made a break out Box. It can connect to the Insert with 19 pin female connectors. We can connect to our instrument with BNC cable. It has 8 female BNC Connector and a 19-pin female connector. We have also written some LabVIEW program to interface Lakeshore 335 and Keithley 2614B and other SMU to perform all our Transport measurement at different temperature with just one click of mouse.

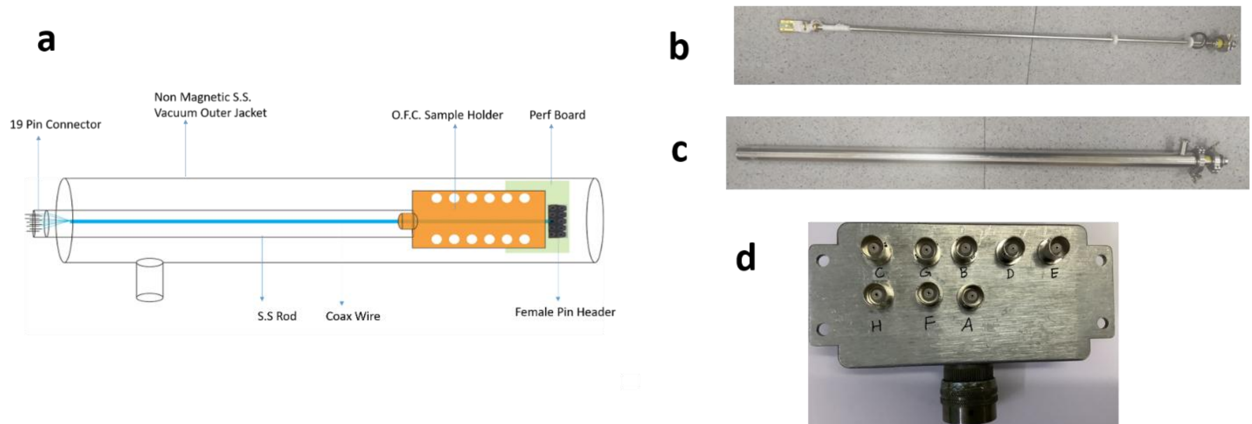

Figure 2.9: (a) Schematic of our Insert (b) Image of Insert (c) Image of Outer Vacuum Jacket of Insert (d) Image of Breakout Box.

Bibliography

(1) Li, H.; Li, Y.; Aljarb, A.; Shi, Y.; Li, L. J. Epitaxial Growth of Two-Dimensional Layered Transition-Metal Dichalcogenides: Growth Mechanism, Controllability, and Scalability. *Chem Rev* **2018**, *118* (13), 6134–6150. https://doi.org/10.1021/ACS.CHEMREV.7B00212.

(2) Bryant, W. A. The Fundamentals of Chemical Vapour Deposition. *J Mater Sci* **1977**, *12* (7), 1285–1306. https://doi.org/10.1007/BF00540843/METRICS.

(3) Cai, Z.; Liu, B.; Zou, X.; Cheng, H. M. Chemical Vapor Deposition Growth and Applications of Two-Dimensional Materials and Their Heterostructures. *Chem Rev* **2018**, *118* (13), 6091–6133. https://doi.org/10.1021/ACS.CHEMREV.7B00536

(4) Ferraro, J. R.; Nakamoto, K.; Brown, C. W. Introductory Raman Spectroscopy: Second Edition. *Introductory Raman Spectroscopy: Second Edition* **2003**, 1–434. https://doi.org/10.1016/B978-0-12-254105-6.X5000-8.

(5) Saito, R.; Tatsumi, Y.; Huang, S.; Ling, X.; Dresselhaus, M. S. Raman Spectroscopy of Transition Metal Dichalcogenides. *Journal of Physics: Condensed Matter* **2016**, *28* (35), 353002. https://doi.org/10.1088/0953-8984/28/35/353002.

(6) Binnig, G.; Quate, C. F.; Gerber, C. Atomic Force Microscope. *Phys Rev Lett* **1986**, *56* (9), 930–933. https://doi.org/10.1103/PHYSREVLETT.56.930.

(7) Deng, X.; Xiong, F.; Li, X.; Xiang, B.; Li, Z.; Wu, X.; Guo, C.; Li, X.; Li, Y.; Li, G.; Xiong, W.; Zeng, Z. Application of Atomic Force Microscopy in Cancer Research. *Journal of Nanobiotechnology 2018 16:1* **2018**, *16* (1), 1–15. https://doi.org/10.1186/S12951-018-0428-0.

(8) Zhang, H.; Huang, J.; Wang, Y.; Liu, R.; Huai, X.; Jiang, J.; Anfuso, C. Atomic Force Microscopy for Two-Dimensional Materials: A Tutorial Review. *Opt Commun* **2018**, *406*, 3–17. https://doi.org/10.1016/J.OPTCOM.2017.05.015.

(9) Nellist, M. R.; Chen, Y.; Mark, A.; Gödrich, S.; Stelling, C.; Jiang, J.; Poddar, R.; Li, C.; Kumar, R.; Papastavrou, G.; Retsch, M.; Brunschwig, B. S.; Huang, Z.; Xiang, C.; Boettcher, S. W. Atomic Force Microscopy with Nanoelectrode Tips for High Resolution Electrochemical, Nanoadhesion and Nanoelectrical Imaging. *Nanotechnology* **2017**, *28* (9), 095711. https://doi.org/10.1088/1361-6528/AA5839.

(10) Zhang, K.; Zhang, T.; Cheng, G.; Li, T.; Wang, S.; Wei, W.; Zhou, X.; Yu, W.; Sun, Y.; Wang, P.; Zhang, D.; Zeng, C.; Wang, X.; Hu, W.; Fan, H. J.; Shen, G.; Chen, X.; Duan, X.; Chang, K.;

Dai, N. Interlayer Transition and Infrared Photodetection in Atomically Thin Type-II MoTe2/MoS2 van Der Waals Heterostructures. *ACS Nano* **2016**, *10* (3), 3852–3858. https://doi.org/10.1021/ACSNANO.6B00980.

(11) Zhou, W.; Wang, Z. L. Scanning Microscopy for Nanotechnology: Techniques and Applications. *Scanning Microscopy for Nanotechnology: Techniques and Applications* **2007**, 1–522. https://doi.org/10.1007/978-0-387-39620-0/COVER.

(12) Akhtar, K.; Khan, S. A.; Khan, S. B.; Asiri, A. M. Scanning Electron Microscopy: Principle and Applications in Nanomaterials Characterization. *Handbook of Materials Characterization* **2018**, 113–145. https://doi.org/10.1007/978-3-319-92955-2_4.

(13) Humphreys, F. J. Grain and Subgrain Characterisation by Electron Backscatter Diffraction. *J Mater Sci* **2001**, *36* (16), 3833–3854. https://doi.org/10.1023/A:1017973432592/METRICS.

(14) Seiler, H. Secondary Electron Emission in the Scanning Electron Microscope. *J Appl Phys* **1983**, *54* (11), R1–R18. https://doi.org/10.1063/1.332840.

(15) Williams, D. B.; Carter, C. B. The Transmission Electron Microscope. *Transmission Electron Microscopy* **1996**, 3–17. https://doi.org/10.1007/978-1-4757-2519-3_1.

(16) Franken, L. E.; Grünewald, K.; Boekema, E. J.; Stuart, M. C. A.; Franken, L. E.; Grünewald, K.; Boekema, E. J.; Stuart, M. C. A. A Technical Introduction to Transmission Electron Microscopy for Soft-Matter: Imaging, Possibilities, Choices, and Technical Developments. *Small* **2020**, *16* (14), 1906198. https://doi.org/10.1002/SMLL.201906198.

(17) Chang, Y. Y.; Han, H. N.; Kim, M. Analyzing the Microstructure and Related Properties of 2D Materials by Transmission Electron Microscopy. *Appl Microsc* **2019**, *49* (1), 1–7. https://doi.org/10.1186/S42649-019-0013-5.

(18) Leuschner, R.; Pawlowski, G. Photolithography. *Handbook of Semiconductor Technology* **2008**, *2*, 177–263. https://doi.org/10.1002/9783527621828.CH4.

(19) Wasa, K.; Kitabatake, M.; Adachi, H. Thin Film Processes. *Thin Film Materials Technology* **2004**, 17–69. https://doi.org/10.1016/B978-081551483-1.50003-4.

(20) Yu, X.; Wang, C.; Liu, Y.; Yu, D.; Xing, T. Recent Developments in Magnetron Sputtering. *Plasma Science and Technology* **2006**, *8* (3), 337. https://doi.org/10.1088/1009-0630/8/3/20.

(21) Mansano, R. D.; Verdonck, P.; Maciel, H. S. Anisotropic Reactive Ion Etching in Silicon, Using a Graphite Electrode. *Sens Actuators A Phys* **1998**, *65* (2–3), 180–186. https://doi.org/10.1016/S0924-4247(97)01681-6.

(22) Pinto, R.; Babu, R. S.; Bhattacharya, P. K. Annealing of Si Damage Caused by Reactive Ion Etching in SF6 Gas Mixtures. *Appl Phys Lett* **1986**, *48* (21), 1427–1429. https://doi.org/10.1063/1.96878.

(23) Franssila, S.; Sainiemi, L. Reactive Ion Etching (RIE). *Encyclopedia of Microfluidics and Nanofluidics* **2008**, 1772–1781. https://doi.org/10.1007/978-0-387-48998-8_1344.

(24) Huff, M. Process Variations in Microsystems Manufacturing. **2020**. https://doi.org/10.1007/978-3-030-40560-1.

(25) Harman, G. G.; Albers, J. The Ultrasonic Welding Mechanism as Applied to Aluminum- and Gold-Wire Bonding in Microelectronics. *IEEE Transactions on Parts, Hybrids, and Packaging* **1977**, *13* (4), 406–412. https://doi.org/10.1109/TPHP.1977.1135225.

(26) Neppiras, E. A. Ultrasonic Welding of Metals. *Ultrasonics* **1965**, *3* (3), 128–135. https://doi.org/10.1016/S0041-624X(65)80003-8.

(27) Zulkifli, M. N.; Abdullah, S.; Othman, N. K.; Jalar, A. Some Thoughts on Bondability and Strength of Gold Wire Bonding. *Gold Bull* **2012**, *45* (3), 115–125. https://doi.org/10.1007/S13404-012-0060-Y/FIGURES/19.

(28) *CVD | Group Devi – Inorganic Materials Chemistry*. https://imc.ruhr-uni-bochum.de/fieldsofresearch/cvd/

(29) Del Barrio, J.; Sánchez-Somolinos, C.; Del Barrio, J.; Sánchez-Somolinos, C. Light to Shape the Future: From Photolithography to 4D Printing. *Adv Opt Mater* **2019**, *7* (16), 1900598. https://doi.org/10.1002/ADOM.201900598.

Chapter 3

Ultrahigh responsivity of non-van der Waals Bi_2O_2Se photodetector

This chapter is an adaption of the research article published in "Nanotechnology 35 075707". This chapter discusses the synthesis characterization transfer and optoelectronic properties of Bi_2O_2Se Nanosheets

3.1 Introduction

Recently, Bi_2O_2Se has emerged as a rising star in 2D materials due to its extremely high carrier mobility, excellent environmental stability, thickness-tunable indirect bandgap, and intrinsic ultrafast (1ps) photoresponse. This unique property has made 2D Bi_2O_2Se a promising semiconductor for various electronic and optoelectronics applications [1–6]. Bi_2O_2Se-based field-effect transistors (FETs) have shown excellent current on/off ratios of $>10^6$ with an almost ideal subthreshold swing (≈65 mV dec^{-1}), which is essential for low-power logic devices [1]. Bi_2O_2Se also offers a high dielectric constant native oxide with an atomic thickness and dangling bond-free surface, positioning it as a promising candidate for application within the semiconductor industry. [7,8]. Furthermore, Peng et al. have demonstrated wafer-scale 2D Bi_2O_2Se fin arrays integrated with epitaxial single-crystalline high-κ Bi_2SeO_5 dielectric, satisfying the most stringent requirements for future advanced transistors [9]. Tong et al. demonstrated a Bi_2O_2Se-based photodetector, which showed a broadband photoresponse of 360-1800 nm [10]. Zhang et al. introduced Bi_2O_2Se in a three-terminal memristor, simultaneously displaying long-term and short-term plasticity[11]. Bi_2O_2Se also

possesses a unique defect structure in which the donor state lies above the conduction band leading to unusual metallicity. Furthermore, there is a spatial separation of electrons from donor sites, suppressing the scattering caused by the donor sites resulting in high mobility [12]. So far, 2D Bi_2O_2Se has been synthesised in several ways, viz. Chemical Vapor Deposition (CVD) [1,2,5,13–18], molecular beam epitaxy [19], pulsed laser deposition (PLD) [20], mechanical exfoliation [21], and solution or wet chemical method synthesis [22–25]. Among these methods, CVD-grown samples on Fluorophlogopite mica (f-mica) provide large single-domain sizes with excellent chemical and structural uniformity. However, transferring Bi_2O_2Se from mica to the target substrate, such as silicon dioxide-coated silicon (SiO_2/Si), is challenging due to the strong electrostatic force between f-mica and Bi_2O_2Se. The conventional wet transfer method uses HF acid, which is extremely dangerous to handle and degrades the Bi_2O_2Se nanosheets [26]. Therefore, it is desirable to safely transfer these crystals from f-mica to a target substrate without the use of any corrosive substance to preserve the material properties of Bi_2O_2Se.

In this work, we synthesized nanosheets of single crystalline Bi2O2Se using Atmospheric Pressure chemical vapor deposition (APCVD). We employed a non-corrosive nail polish-assisted dry transfer method to transfer the nanosheets of Bi_2O_2Se to SiO_2/Si substrate without causing any damage to the crystal. The high quality of the Bi_2O_2Se nanosheets is substantiated by fabricating photodetectors out of the as transferred crystals. Under the illumination of 660 nm light, our photodetector shows ultrahigh responsivity of 1.16×10^6 A/W, specific detectivity of 2.55×10^{13} Jones, and gate tunable photoresponse time.

3.2 Experimental Details

3.2.1 Growth and Characterization

Bi_2O_2Se nanosheets were grown by homebuilt APCVD. 88 mg of Bi_2O_3 (99.999% Sigma Aldrich) and 45 mg of Bi_2Se_3 (99.995% Sigma Aldrich) were used as a precursor in an alumina crucible at a distance of 5 cm. Freshly cleaved Fluorphlogopite Mica (Continental Trade) was used as a substrate. The substrates were kept downstream at a distance of 7 cm. Argon was used as a carrier gas. The flow was set to 100 sccm with the help of Alicat mass flow controller. The temperature of the furnace (Nabertherm, Germany) was set to 700℃. The morphology of the as-grown sample was examined by an optical microscope (NIKON Eclipse LV150N). Raman spectroscopy was done with a laser of wavelength 632.8nm using a Raman Microscope (LabRAM HR) having a 50X objective lens. The thickness of the nanosheets was determined by Keysight 5500 AFM. HRTEM characterization was done using a JEOL JEM-2200FS Transmission electron microscope.

3.2.2 Transfer and device fabrication

A homebuilt transfer stage was used to transfer as grown Bi_2O_2Se. PDMS stamp was made by mixing PDMS liquid and the hardener in a 10:1 ratio and was subsequently cured at 90 °C for 30 min. This PDMS stamp was then attached to a clean glass slide. A drop of nail polish is placed on the surface of the PDMS. The glass slide is then baked on the hot plate at 90℃ to harden and cure

Nail polish, creating a solid, sticky surface for flake pickup. In our transfer stage, the flake of interest is aligned with the pickup slide and brought in contact at 55°C. Once the flake is completely laminated with nail polish, the temperature is lowered to 30°C. The slide is then raised, picking up the Mica and Bi_2O_2Se. The Mica layer also comes along with Bi_2O_2Se due to the high adhesivity of Nail polish, and then this slide is brought in contact with SiO_2 (300nm)/Si substrate and heated at 110°C to melt the nail polish. At 110°C, the slide can be retraced, and the nail polish will melt to the surface, leaving the stack on the substrate. The substrate with the transferred stack is then put in an acetone bath for 10 min to clean the nail polish away and then rinsed in an isopropyl alcohol bath and dried with nitrogen gas.

For device fabrication, source and drain contacts are patterned by Standard photolithography. (5/65) nm of Pd/Au was deposited by sputtering.

3.2.3 Electrical Measurement

Electrical measurements were done using Keithley 2450 and 2614B source-measure units. Time-resolved photoresponse was measured by turning on and off a 660 nm LED of intensity 666 $\mu W/cm^2$. All these measurements were done in vacuum (10^{-6} mbar). The spectral photoresponse of our devices were measured in the wavelength range from 400 nm to 1100 nm using a Xenon lamp as the light source and Horiba iHR 320 spectrometer with 600 groves/mm grating. The resulting photocurrent was measured in the ambient environment using a Keithley 2450 source-measure unit.

3.3 Results and Discussion

3.3.1 CVD Growth of Bi_2O_2Se

As a typical bismuth-based oxychalcogenide material, Bi_2O_2Se has a body-centered tetragonal lattice structure with an I4/mmm space group, where a negatively charged $[Se]^{2-}$ layer sandwiches a covalently bonded $[Bi_2O_2]^{2+}$ layer with a weak electrostatic force instead of the van der wall interaction as observed in typical 2D materials such as Graphene, MoS_2, etc. [2]. The top view of the crystal structure of Bi_2O_2Se is shown in Figure 3.1a. The blue, green, and red balls are Bi, Se, and O atoms, respectively. Two-dimensional Bi_2O_2Se nanosheets were synthesized using a home-built atmospheric pressure chemical vapor deposition (APCVD) system equipped with a horizontal tube furnace and 25 mm inner diameter quartz tube. Figure 3.1b shows the schematic of our APCVD setup, in which the precursors, Bi_2O_3 powder and Bi_2Se_3 powder, were placed in two alumina boats with a separation of 7 cm between them. Atomically flat f-mica, with its intrinsically layered structure, and high thermal stability, is used as a substrate for growth. Furthermore, the electrostatic interaction of the K^+ layer of f-mica with the Se^{2-} layer in Bi_2O_2Se results in the planar growth of Bi_2O_2Se nanosheets [27] Freshly cleaved f-mica substrates were kept at a distance of 7 cm downstream from the Bi_2O_3 precursor. The growth temperature used in our study ranges from

660°C to 700°C. Argon is used as a carrier gas, and the flow was set to 100 cm with the help of the Alicat mass flow controller. The typical growth time used in this study is around 60 minutes. Figure 3.1c shows the optical microscope (OM) image of as-synthesized 2D Bi_2O_2Se showing rectangular flakes of sizes up to a few tens of micrometers. Depending upon the growth conditions like flow rate and temperature, as-grown samples can have different morphologies [28,29].

3.3.2 Characterisation of as-grown Bi_2O_2Se

Thickness of the samples were determined using Atomic Force Microscope (AFM). Figure 3.2 shows the AFM image of the Bi_2O_2Se sheet having a thickness of 6 nm. In Raman spectroscopy, done with an excitation wavelength (λex) of 632.8 nm, we observed the characteristic A_{1g} peak at 160.2 cm^{-1} (Figure 3.1d), which corresponds to out-of-plane vibration of Bi atoms, consistent with prior reports [26,28,30]. Energy Dispersive Spectroscopy (EDS) shows the elemental distribution of

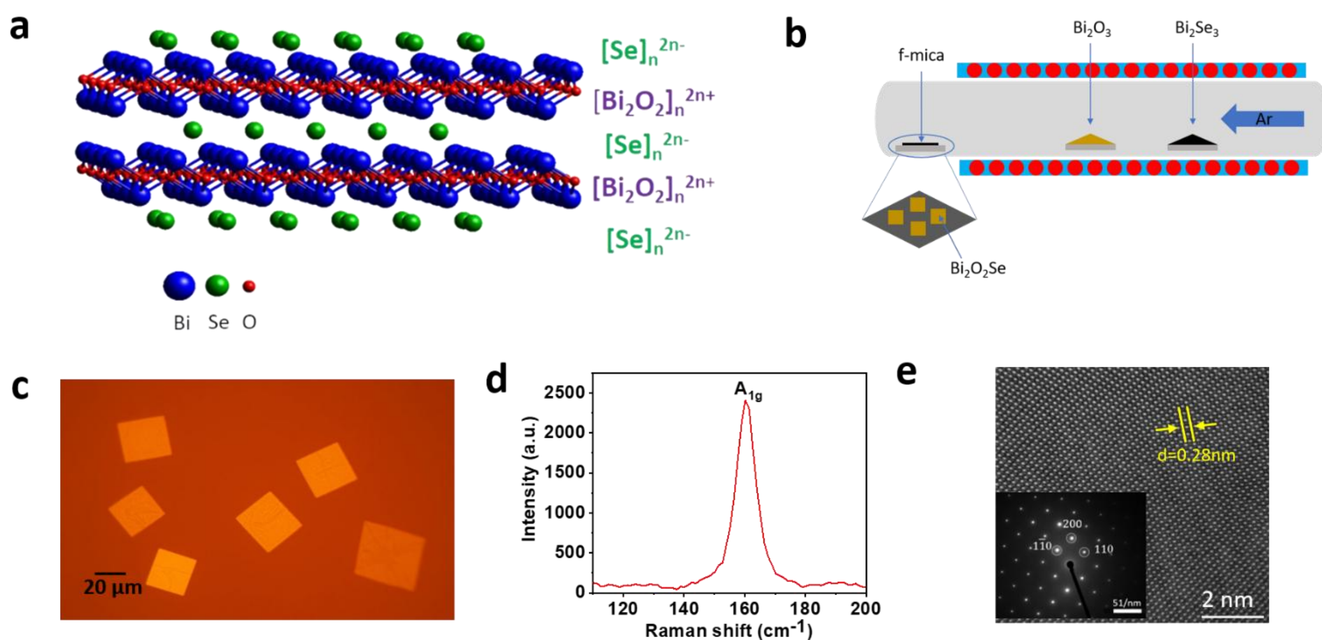

Figure 3.1 : **(a)** Schematic of layered Bi_2O_2Se crystal structure with tetragonal $[Bi_2O_2]_n$ layers and[$Se]_n$ layers alternately stacked along the c axis. For clarity, the weak electrostatic interactions between [Se] and the $[Bi_2O_2]$ layer in Bi_2O_2Se are not shown. **(b)** Schematic illustration of our APCVD setup to grow Bi_2O_2Se on Mica with Bi_2Se_3 and Bi_2O_3 as co-evaporation sources. **(c)** Representative optical microscope image of as-synthesised Bi_2O_2Se nanosheet on Mica is shown. **(d)** Raman spectrum of as-grown Bi_2O_2Se shows the characteristic peak at 160.2cm^{-1}. **(e)** SAED pattern indexed using the Bi_2O_2Se crystal structure of I4/mmm space group. HRTEM lattice image showing lattice parameter = 0.28nm corresponding to (110) plane.

Bi_2O_2Se with 1:1.94 chemical stoichiometry between Se and Bi atoms (Figure 3.3), while the O content is inaccurate under the EDS measurement. We have done High-resolution transmission

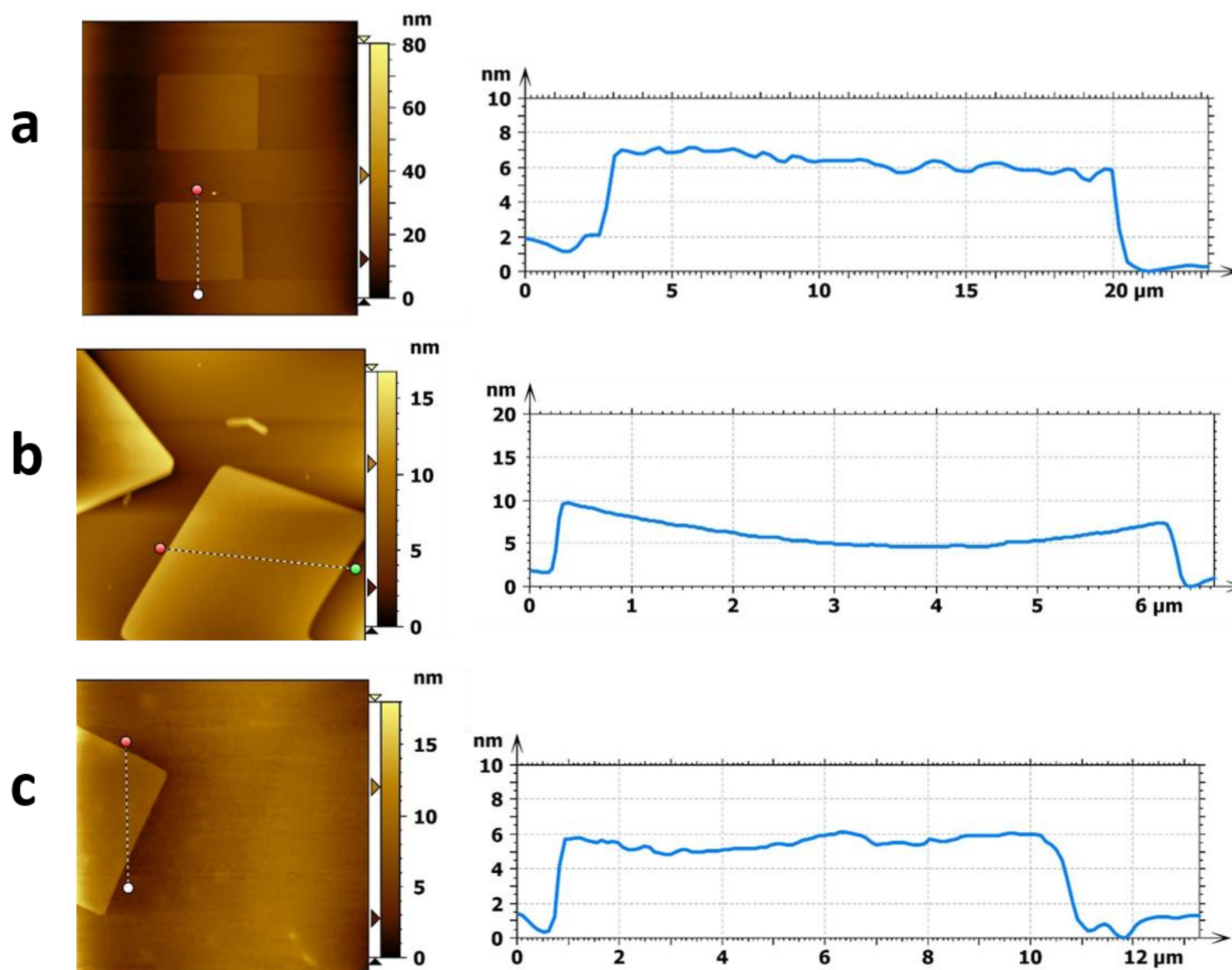

Figure 3.2 : Atomic Force Microscopy Image of as grown Bi_2O_2Se of three different flakes.

electron microscopy (HRTEM) to further analyze the crystal structure and lattice parameter. The as-grown Bi_2O_2Se nanosheets were transferred from the f-mica substrate onto a carbon-supported Cu grid by the polystyrene-assisted transfer method [26]. The selected area electron diffraction (SAED) pattern shows the single crystalline nature of Bi_2O_2Se flakes. The square arrangement of

diffraction spots at (200), (110), and $(1\bar{1}0)$ in the SAED pattern corresponds to the tetragonal structure of Bi_2O_2Se. In Figure 3.1e, the HRTEM lattice image shows the interatomic distance of 0.28 nm, corresponding to the (110) plane, which is close to the theoretical value of 0.27nm [31].

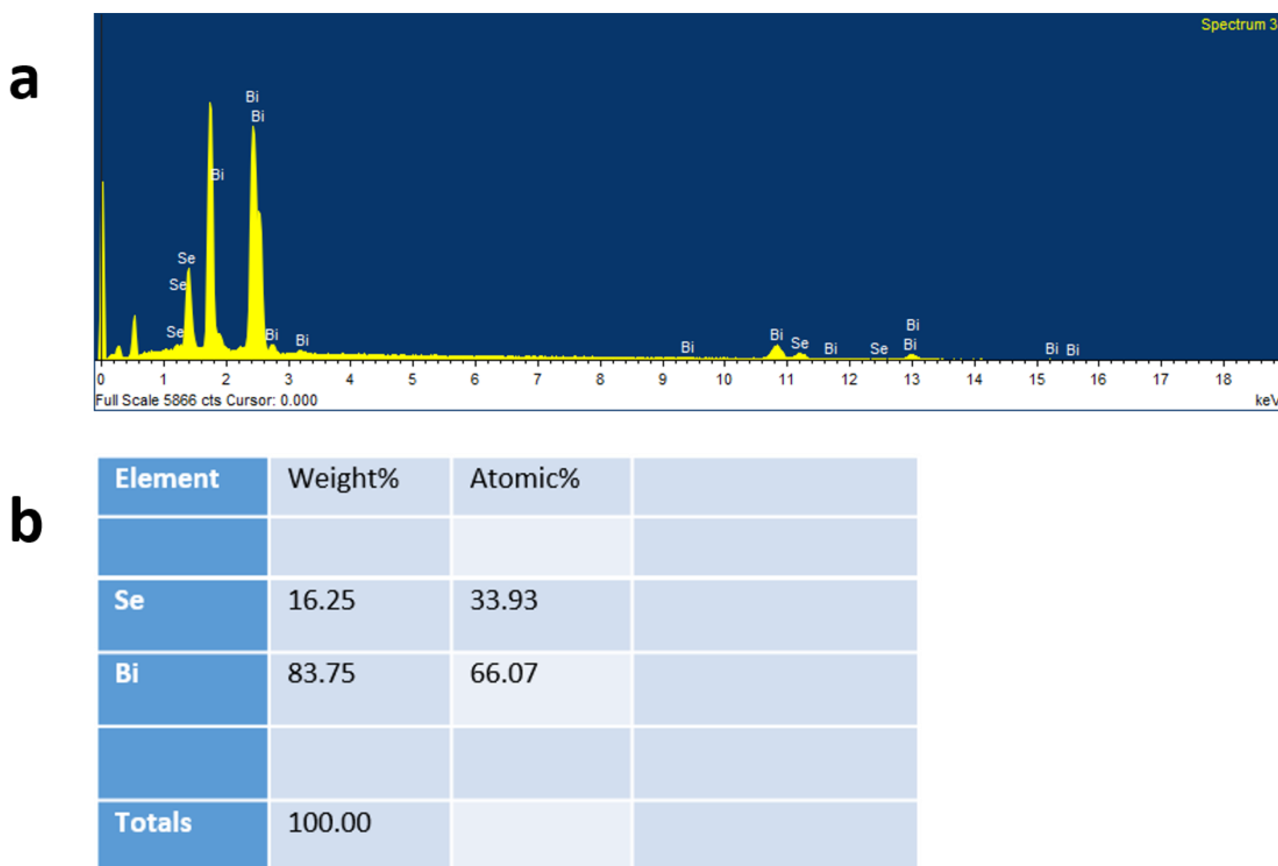

Element	Weight%	Atomic%	
Se	16.25	33.93	
Bi	83.75	66.07	
Totals	100.00		

Figure 3.3 : (a) EDX spectrum of as grown Bi_2O_2Se b) Its Corresponding Elemental Composition.

3.3.3 Nail Polish Assisted Transfer and Electrical Characterisation

To study the electrical properties of as-grown Bi_2O_2Se nanosheets, we have transferred them onto a 300 nm SiO_2-coated Si substrate. Because of the strong electrostatic interaction between f-mica and Bi_2O_2Se, it is challenging to transfer thin sheets of Bi_2O_2Se. We used the non-corrosive nail polish-assisted dry transfer method [32] to transfer our nanosheets. The schematic of our transfer process is illustrated in (Figure 3.4a), and the details have been discussed in the experimental section. Figure 3.4b shows the OM image of transferred Bi_2O_2Se on the SiO_2/Si substrate. During the transfer process, sometimes few layers of mica also came underneath of very thin Bi_2O_2Se due to the highly adhesive nature of the nail polish. Slightly thicker samples get easily transferred without peeling off the mica sheet. Using this method, we transferred the as-grown crystals without any associated contamination or crystal damage caused by chemical etching, thereby ensuring the quality of the transferred crystal. We also performed AFM (Figure 3.5) on the transferred crystals and did not observe any noticeable damage to them after the transfer

We fabricated back-gated field effect transistor (FET) of Bi_2O_2Se using photolithography and metal deposition (Pd/Au -5/65nm) to study their electrical transport properties. A Schematic of the

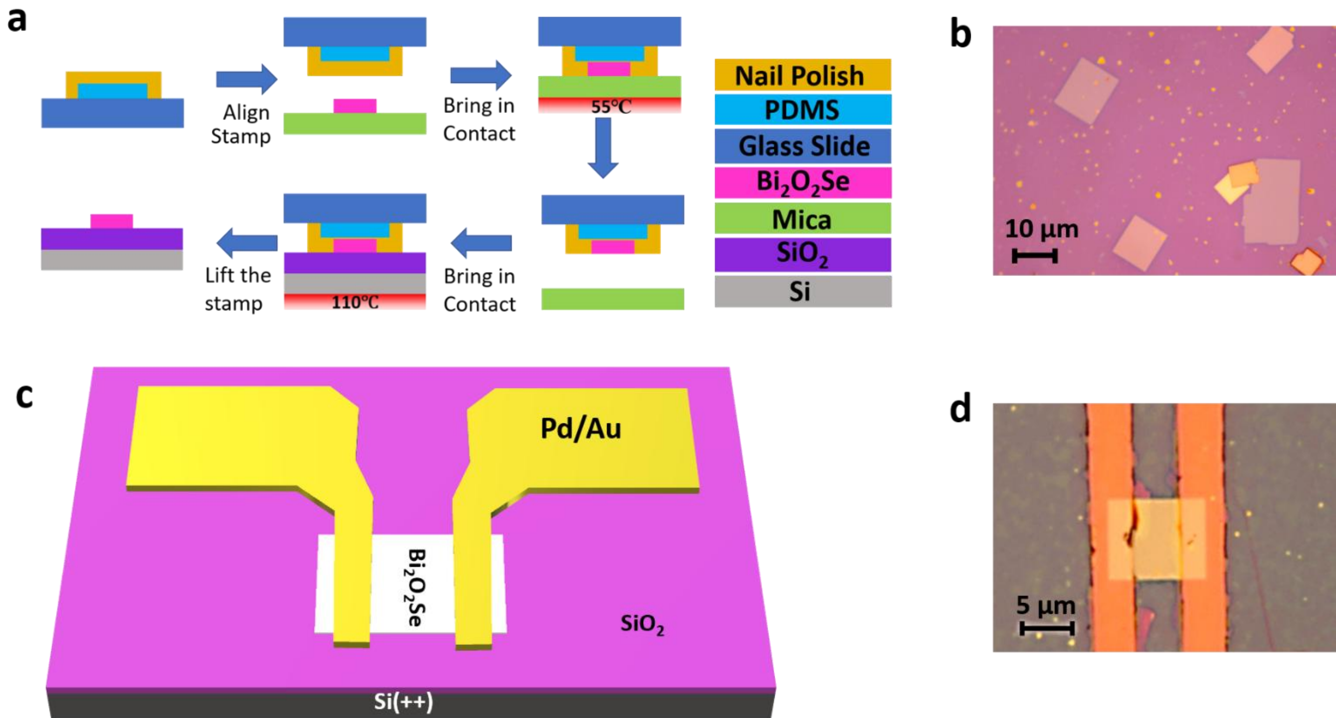

Figure 3.4 : (a) Schematic showing the subsequent steps of the transfer process involved in our homebuilt transfer stage. (b) OM image of the as-transferred Bi_2O_2Se on SiO_2/Si substrate. Schematic of the FET geometry is shown in (c) and an OM image of our FET device is shown in (d).

FET device is shown in Figure 3.4c, and an optical microscope image of a representative device is shown in Figure 2d. The current-voltage (*I-V*) characteristics were measured in vacuum condition (see experimental section for details). Figure 3.6a shows the source-drain current (I_{sd}) as

a function of source-drain voltage (V_{sd}) for different back-gate bias (V_g) (output characteristics) of the device measured at room temperature. The source-drain characteristics were measured across a range of back gate voltages spanning from 0 to 100 V, incrementally increasing in steps of 10 V.

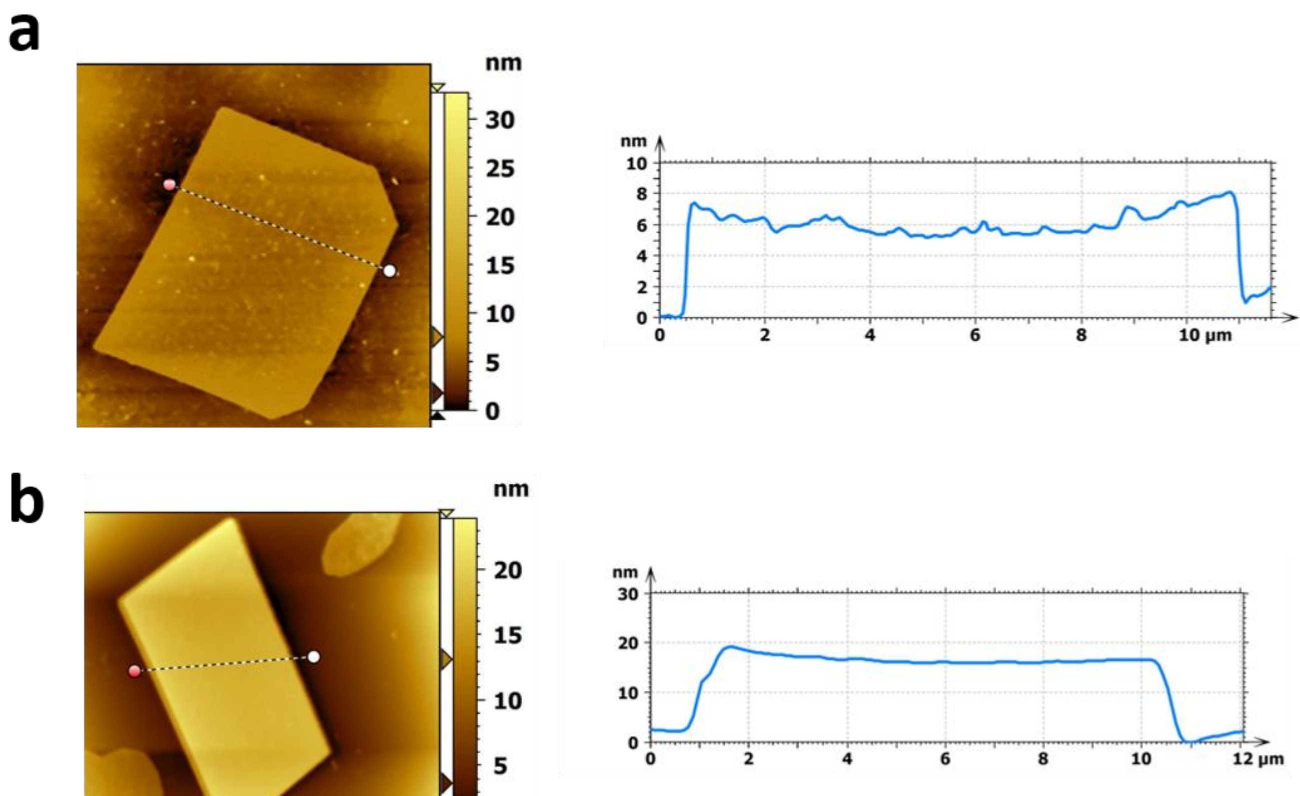

Figure 3.5 AFM topography image of nail polish assisted transferred Bi_2O_2Se nanosheet of thickness 7 nm showing RMS roughness 3.3 Å . b) AFM topography of a pristine Bi_2O_2Se on f -mica of thickness 18nm showing RMS roughness of 2 Å.

The *I-V* characteristics show linear behaviour at low drain-source bias confirming the formation of Ohmic contact between the Bi_2O_2Se and metal electrodes. It can be seen from Figure 3.6a that drain current is strongly dependent on V_g, which indicates the efficient gate controllability of our devices. Transfer characteristics (I_{sd} vs. V_g) of Bi_2O_2Se at different V_{sd}, show typical n-type

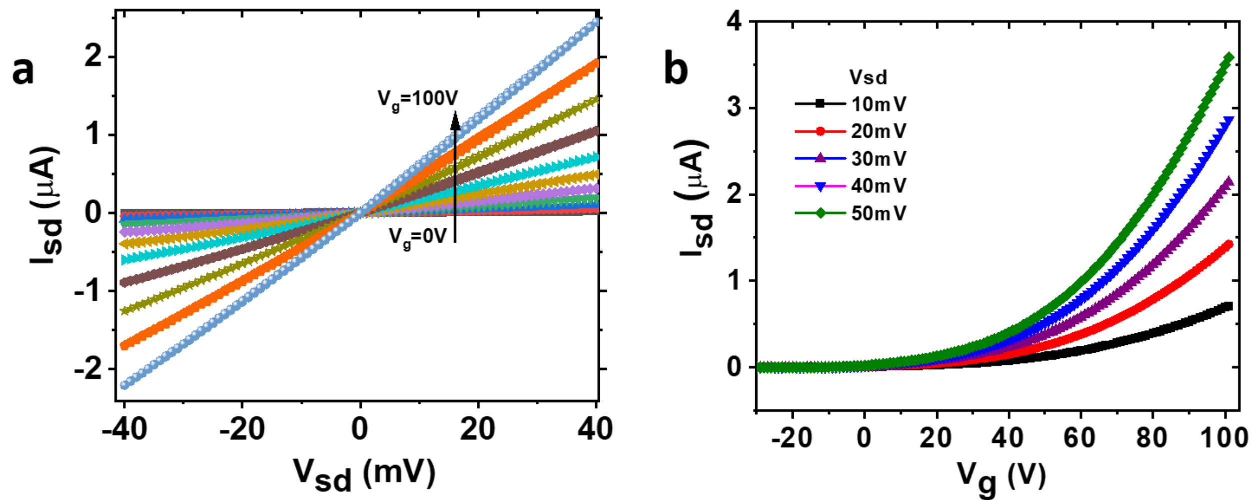

Figure 3.6 : Electrical characterization of as transferred Bi_2O_2Se: (a) Output characteristics curve (I_{sd}-V_{sd}) of the device at different back gate voltage (V_g) is shown. The linear nature indicates Ohmic contact. (b)Transfer Characteristics curve (I_{ds} -V_g) is shown as a function of various V_g, for different V_{sd}.

behaviour in which I_{sd} increases with increasing V_g. (Figure 3.6b). We extracted the field effect mobility (μ) by linear fitting of the transfer curve and using the equation of $\mu = (L/W)(1/C_g)(1/V_{ds})(dI_{ds}/dV_g)$ where L is the channel length, W is the channel width. C_g is the gate capacitance per unit area. In case if a thin layer of mica is present under the device then $C_g = (C_{mica} \times C_{SiO_2})/(C_{mica} + C_{SiO_2})$, where C_{SiO_2} and C_{mica} are the capacitance per unit area of the SiO_2 and mica

layer. In this study, the thickness of SiO_2 and f-mica were 300 nm (confirmed using thin film reflectometric technique) and 136 nm (measured using AFM) respectively. For all the calculations, the static dielectric constant (ε) of SiO_2 and f-mica were taken as 3.9 and 5.6, respectively. Using these values, we found that for a typical 10 nm thick Bi_2O_2Se, the value of μ of as transferred device is 102 $cm^2\ V^{-1}\ s^{-1}$ with an on/off ratio of 10^4. We also tried to study the electrical properties of thicker (thickness more than 100 nm) samples, but they did not show any field effect characteristics or detectable photoresponse.

3.3.4 Optoelectronic properties

Figure 3.7a displays the responsivity versus wavelength scan of the device within the spectral range of 400 nm to 1100 nm. Our investigation reveals that the device demonstrates a remarkably high responsivity throughout the scan range, reaching a maximum value of more than 12,000 A/W at 460 nm. Notably, even at wavelengths above 850 nm, the device's responsivity is still considerably high. To cross-verify the photoresponse in NIR region, we studied the time-resolved photoresponse of our device at the NIR region using an LED having a wavelength of 940 nm and an intensity of 1.8 mW/cm^2 (Figure 3.7b). The device showed a decent photocurrent on-off ratio of 2.

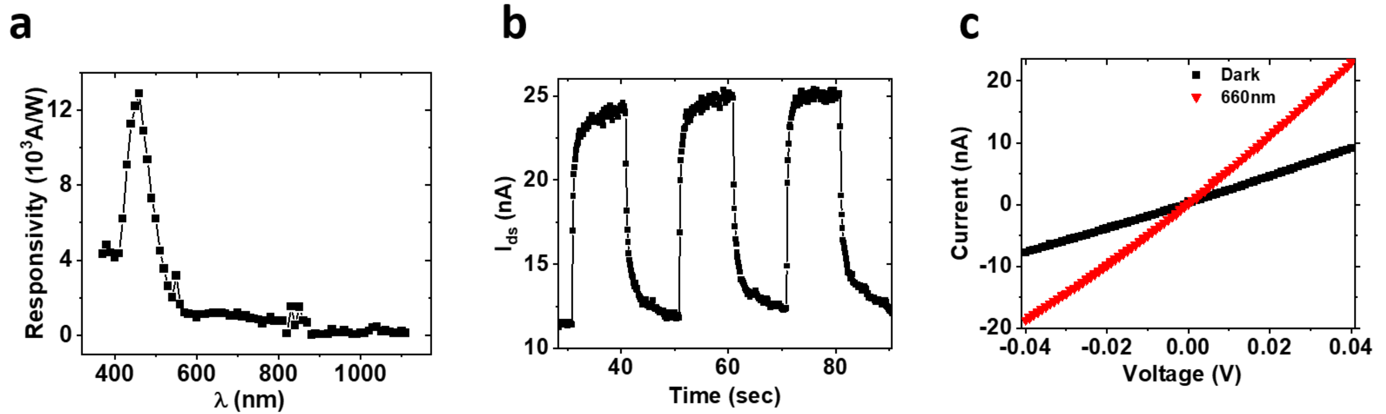

Figure 3.7 : (a) Responsivity versus wavelength scan of the device within the spectral range of 400 nm to 1100 nm is shown. (b) I-t response of our device under the illumination of 940nm LED with intensity 1.8mW/cm^2. (c) I-V characteristics of the FET device in the absence and presence of light (660 nm LED of intensity 666μW/cm^2).

For further studies of the optoelectronic properties, the devices were illuminated using a 660 nm LED. The selection of the 660 nm wavelength was made due to its position within a responsivity region that exhibited comparability across a wide spectrum of wavelengths, encompassing 570 nm - 800 nm. The source intensity values corresponding to specific wavelengths, as well as the corresponding device photocurrent data, are given in the (Figure 3.8).

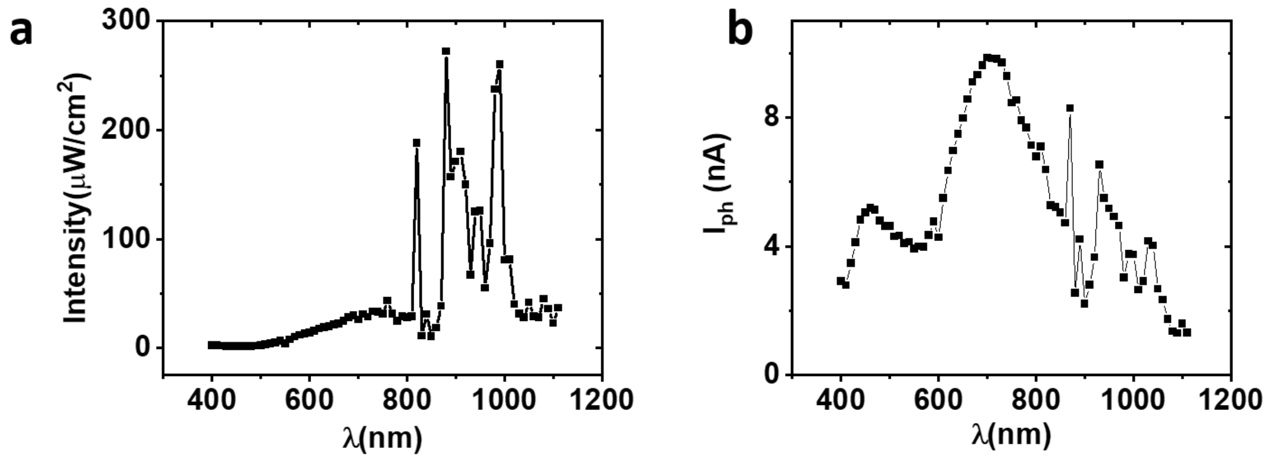

Figure 3.8 : (a) Intensity Vs Wavelength plot of the light source(Xeneon Lamp) used for spectral responsivity study b) Corresponding Photocurrent I_{ph} Vs wavelength of the device.

Figure 3.7c shows the *I-V* characteristics of light in the absence and presence of light (660 nm LED of intensity 666 μW/cm^2), which shows current increases in the presence of light due to the photoconductive effect. The time-resolved photoresponse of the device is shown in Figure 3.9a, which shows that the device has a stable switching behaviour after several cycles. It shows a rise time of ~100 ms and a decay time of ~105 ms. Here the rise time is the time for the photocurrent (I_{ph}) to increase from 10% I_{ph} (max) to 90% I_{ph} (max), and the decay time is the time taken to reach from 90% I_{ph} (max) to 10% I_{ph} (max). By changing the gate voltage, we can tune the response time of our device, as shown in Figure 3.9b. The decay time of our back-gated device increases from 85 ms to 4.98 sec when V_g changed from -80V to 30V (Figure 3.10). In order to understand this

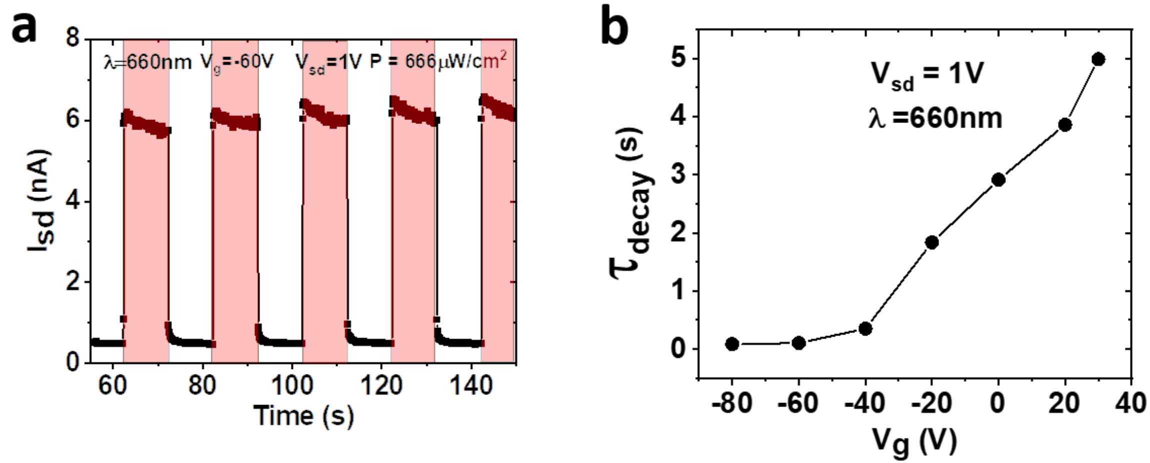

Figure 3.*9* (a) Time-resolved photoresponse of the device at V_g=-60V, V_{sd} =1V is presented. Temporal Photoresponse of our device at different gate voltage is shown in (b)

phenomenon, it is important to distinguish between recombination centres and trap states [10,33]. Recombination centres are located at the midgap and promote the recombination of electron-hole pairs, while trap states only trap one type of photocarrier, allowing the other to circulate for a longer period of time. When $V_g > V_{Th}$ (threshold voltage), the Fermi level is close to the conduction band, causing most electron trap states to be filled and leaving only a few recombination centres. Consequently, there are fewer recombination centres in this scenario, and the detrapping process

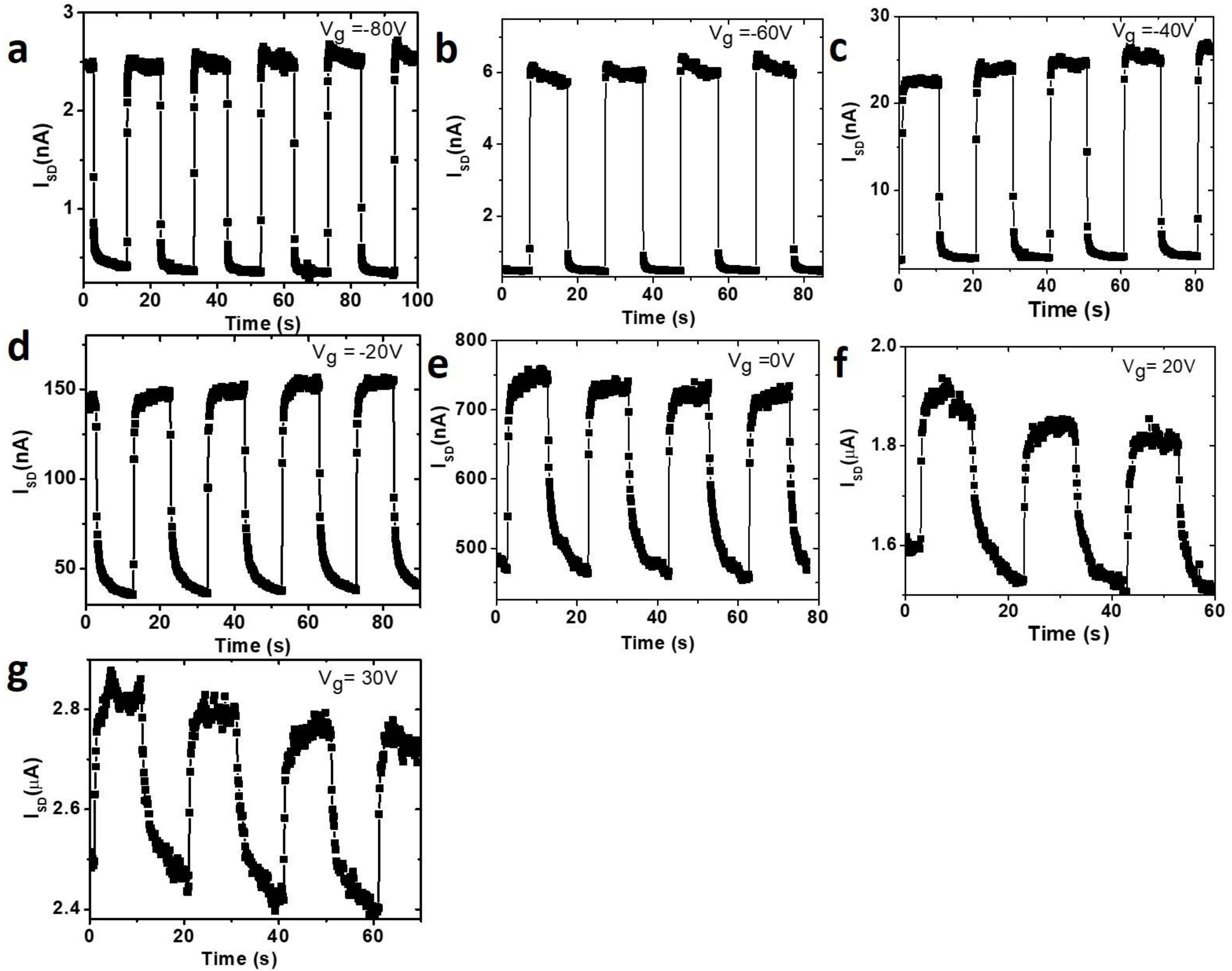

Figure 3.10 I-t response of our device at V_{sd} =1V and at different back gate Voltage a) V_g =-80V b) V_g =-60V c) V_g =-40V d) V_g =-20V e) V_g = 0V f) V_g =20V g) V_g = 30V under the illumination of 660nm LED with intensity 666μW/cm^2.

takes a long time, resulting in a long decay time. However, when $V_g < V_{Th}$, the Fermi level moves

away from the conduction band, causing only a few trap states to be occupied [34]. In addition, there are unoccupied states above the Fermi level that can serve as recombination centers, promoting electron-hole pair recombination. As a result, the decay time decreases in this case [10].

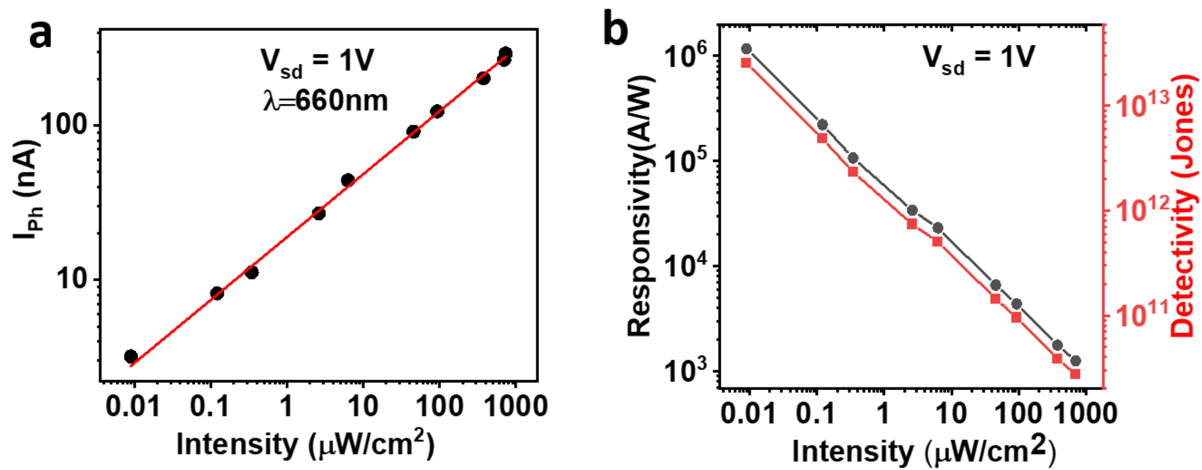

Figure 3.11 (a) Photocurrent vs. power of incident light is shown in log-log scale. (b) Shows the plot of Responsivity and Detectivity vs. Power of incident light.

To analyze the dependence of photoresponse on the power of incident illumination intensity, the photocurrent $I_{ph} = I_{light} - I_{dark}$ was measured at $V_{ds} = 1V$ as a function of LED power density. We observe that photocurrent increases sublinearly with an increase in light intensity, as shown in Figure 4e. Fitting the data using a power law, $I_{ph} \approx P^{\alpha}$, we found the value of α to be 0.40 (Figure 3.11a). The nonunity exponent is attributed to the complex processes, which relate to the trap states caused by the defect or impurities in Bi_2O_2Se or Bi_2O_2Se-substrate interface [26]. These traps might

account for the sublinear power dependence where more traps could be filled by photoinduced charge carriers as the light intensity increases, leading to the saturation of photocurrent. This phenomenon was also observed in other 2D materials [35–37].

To evaluate the performance of a Photodetector, Responsivity,

$$R = \frac{I_{ph}}{P \times A}$$

and Specific detectivity,

$$D = \frac{A^{1/2} \times R}{(2 \times q \times I_d)^{1/2}}$$

are the two important figures of merit. Where I_{ph} is the photocurrent, A is the effective area, P is the incident power, and q is the charge. In the expression of specific detectivity, we have assumed that Dark current is the major contributor to the shot noise. We calculated both responsivity and specific detectivity as a function of incident power by using the above expression. We found that both responsivity and specific detectivity decrease with increasing power density (Figure 3.11b). This is because of the presence of trap states in the Bi_2O_2Se or the Bi_2O_2Se-substrate interface. At lower power density of incident light, electrons and holes are trapped by the trap states, resulting in reduced recombination and an increase in lifetime, leading to higher R and D. As the power density increases, the number of available trap states decreases, resulting in the saturation of

photoresponse [38]. We got an ultrahigh responsivity of 1.16×10^6 A/W, specific detectivity 2.55×10^{13} Jones, at an incident power of 9nW, which is one of the highest among the 2D materials (Table 3.1).

Table 3.1:Performance comparison of Bi_2O_2Se Optoelectronic devices

Material	Synthesis method	Mobility ($cm^2V^{-1}s^{-1}$)	Wavelength (nm)	Responsivity (AW^{-1})	Specific Detectivity (Jones)	Rise Time (ms)	Decay Time (ms)
Bi_2O_2Se[14]	CVD	-	808	6.5	8.3×10^{11}	3.2	4.6
Bi_2O_2Se[4]	CVD	-	1200	65	3×10^9	-	-
Bi_2O_2Se[39]	CVD		1260	3.5			
Bi_2O_2Se[26]	CVD	107	532	3.5×10^4	9×10^{13}	0.308	0.448
Bi_2O_2Se[40]	CVD		500	1.2	7×10^{11}		
Bi_2O_2Se[41]	CVD	243	532	2000	-		
Bi_2O_2Se[42]	CVD		900	101	1.9×10^{10}	30	60
Bi_2O_2Se[15]	VS	150	660	2.2×10^4	3.4×10^{15}	6	20
Bi_2O_2Se[43]	MOCVD	127	405	45134	3.3×10^{13}	4.6	5.3
Bi_2O_2Se[44]	CVD	-	640	6	1.3×10^8	0.036	0.016

Bi_2O_2Se[13]	CVD	1400	450	60	2.4×10^{10}	5	7
Bi_2O_2Se[45]	Solution Method		520	6.1	-	0.368	0.592
Bi_2O_2Se[25]	Solution Method	334.7	532	842.91	8.18×10^{12}	-	-
Bi_2O_2Se	This Work	100	660	1.16×10^{6}	2.55×10^{13}	100.8	105.2

3.4. Summary

We have successfully synthesized high-quality Bi_2O_2Se nanosheets using APCVD. As-grown thin sheets of Bi_2O_2Se on f-mica were transferred to SiO_2/Si substrate using a nail polish-assisted dry transfer method without any chemical etching or damage. The back-gated Bi_2O_2Se FET showed decent mobility of 100 $cm^2V^{-1}s^{-1}$ and a good current on/off ratio of 10^4. Our devices showed high responsivity of 1.16×10^6 A/W and a specific detectivity of 2.55×10^{13} Jones, which makes it a very good photodetector. Moreover, our devices exhibited a broadband spectral photoresponse and gate-tunable response time. Our study suggests the potential use of Bi_2O_2Se in future electronics and optoelectronics applications.

Bibliography

(1) Wu, J.; Yuan, H.; Meng, M.; Chen, C.; Sun, Y.; Chen, Z.; Dang, W.; Tan, C.; Liu, Y.; Yin, J.; Zhou, Y.; Huang, S.; Xu, H. Q.; Cui, Y.; Hwang, H. Y.; Liu, Z.; Chen, Y.; Yan, B.; Peng, H. High Electron Mobility and Quantum Oscillations in Non-Encapsulated Ultrathin Semiconducting Bi2O2Se. Nature Nanotechnology 2017 12:6 2017, 12 (6), 530–534. https://doi.org/10.1038/nnano.2017.43.

(2) Wu, J.; Tan, C.; Tan, Z.; Liu, Y.; Yin, J.; Dang, W.; Wang, M.; Peng, H. Controlled Synthesis of High-Mobility Atomically Thin Bismuth Oxyselenide Crystals. Nano Lett 2017, 17 (5), 3021–3026. https://doi.org/10.1021/acs.nanolett.7b00335.

(3) Li, T.; Tu, T.; Sun, Y.; Fu, H.; Yu, J.; Xing, L.; Wang, Z.; Wang, H.; Jia, R.; Wu, J.; Tan, C.; Liang, Y.; Zhang, Y.; Zhang, C.; Dai, Y.; Qiu, C.; Li, M.; Huang, R.; Jiao, L.; Lai, K.; Yan, B.; Gao, P.; Peng, H. A Native Oxide High-κ Gate Dielectric for Two-Dimensional Electronics. Nature Electronics 2020 3:8 2020, 3 (8), 473–478. https://doi.org/10.1038/s41928-020-0444-6.

(4) Yin, J.; Tan, Z.; Hong, H.; Wu, J.; Yuan, H.; Liu, Y.; Chen, C.; Tan, C.; Yao, F.; Li, T.; Chen, Y.; Liu, Z.; Liu, K.; Peng, H. Ultrafast and Highly Sensitive Infrared Photodetectors Based on Two-Dimensional Oxyselenide Crystals. Nature Communications 2018 9:1 2018, 9 (1), 1–7. https://doi.org/10.1038/s41467-018-05874-2.

(5) Wu, J.; Qiu, C.; Fu, H.; Chen, S.; Zhang, C.; Dou, Z.; Tan, C.; Tu, T.; Li, T.; Zhang, Y.; Zhang, Z.; Peng, L.-M.; Gao, P.; Yan, B.; Peng, H. Low Residual Carrier Concentration and High Mobility in 2D Semiconducting Bi2O2Se. Nano Lett 2018. https://doi.org/10.1021/ACS.NANOLETT.8B03696.

(6) Tan, C.; Tang, M.; Wu, J.; Liu, Y.; Li, T.; Liang, Y.; Deng, B.; Tan, Z.; Tu, T.; Zhang, Y.; Liu, C.; Chen, J. H.; Wang, Y.; Peng, H. Wafer-Scale Growth of Single-Crystal 2D Semiconductor on Perovskite Oxides for High-Performance Transistors. Nano Lett 2019, 19 (3), 2148–2153. https://doi.org/10.1021.

(7) Zhang, C.; Tu, T.; Wang, J.; Zhu, Y.; Tan, C.; Chen, L.; Wu, M.; Zhu, R.; Liu, Y.; Fu, H.; Yu, J.; Zhang, Y.; Cong, X.; Zhou, X.; Zhao, J.; Li, T.; Liao, Z.; Wu, X.; Lai, K.; Yan, B.; Gao, P.; Huang, Q.; Xu, H.; Hu, H.; Liu, H.; Yin, J.; Peng, H. Single-Crystalline van Der Waals Layered Dielectric with High Dielectric Constant. Nature Materials 2023 2023, 1–6. https://doi.org/10.1038/s41563-023-01502-7.

(8) Tu, T.; Zhang, Y.; Li, T.; Yu, J.; Liu, L.; Wu, J.; Tan, C.; Tang, J.; Liang, Y.; Zhang, C.; Dai, Y.; Han, Y.; Lai, K.; Peng, H. Uniform High-k Amorphous Native Oxide Synthesized by Oxygen Plasma for Top-Gated Transistors. Nano Lett 2020, 20 (10), 7469–7475. https://doi.org/10.1021/ACS.NANOLETT.0C02951/ASSET/IMAGES/LARGE/NL0C02951_0005.JPEG.

(9) Tan, C.; Yu, M.; Tang, J.; Gao, X.; Yin, Y.; Zhang, Y.; Wang, J.; Gao, X.; Zhang, C.; Zhou, X.; Zheng, L.; Liu, H.; Jiang, K.; Ding, F.; Peng, H. 2D Fin Field-Effect Transistors Integrated with Epitaxial High-k Gate Oxide. Nature 2023 616:7955 2023, 616 (7955), 66–72. https://doi.org/10.1038/s41586-023-05797-z.

(10) Tong, T.; Chen, Y.; Qin, S.; Li, W.; Zhang, J.; Zhu, C.; Zhang, C.; Yuan, X.; Chen, X.; Nie, Z.; Wang, X.; Hu, W.; Wang, F.; Liu, W.; Wang, P.; Wang, X.; Zhang, R.; Xu, Y. Sensitive and Ultrabroadband Phototransistor Based on Two-Dimensional Bi2O2Se Nanosheets. Adv Funct Mater 2019, 29 (50), 1905806. https://doi.org/10.1002/ADFM.201905806.

(11) Zhang, Z.; Li, T.; Wu, Y.; Jia, Y.; Tan, C.; Xu, X.; Wang, G.; Lv, J.; Zhang, W.; He, Y.; Pei, J.; Ma, C.; Li, G.; Xu, H.; Shi, L.; Peng, H.; Li, H. Truly Concomitant and Independently Expressed Short- and Long-Term Plasticity in a Bi2O2Se-Based Three-Terminal Memristor. Advanced Materials 2019, 31 (3), 1805769. https://doi.org/10.1002/ADMA.201805769.

(12) Fu, H.; Wu, J.; Peng, H.; Yan, B. Self-Modulation Doping Effect in the High-Mobility Layered Semiconduct Bi2O2Se. Phys Rev B 2018, 97 (24), 241203. https://doi.org/10.1103/PhysRevB.97.241203.

(13) Yang, X.; Zhang, Q.; Song, Y.; Fan, Y.; He, Y.; Zhu, Z.; Bai, Z.; Luo, Q.; Wang, G.; Peng, G.; Zhu, M.; Qin, S.; Novoselov, K. High Mobility Two-Dimensional Bismuth Oxyselenide Single Crystals with Large Grain Size Grown by Reverse-Flow Chemical Vapor Deposition. ACS Appl Mater Interfaces 2021, 13 (41), 49153–49162. https://doi.org/10.1021/ACSAMI.1C13491.

(14) Li, J.; Wang, Z.; Wen, Y.; Chu, J.; Yin, L.; Cheng, R.; Lei, L.; He, P.; Jiang, C.; Feng, L.; He, J. High-Performance Near-Infrared Photodetector Based on Ultrathin Bi2O2Se Nanosheets. Adv Funct Mater 2018, 28 (10). https://doi.org/10.1002/ADFM.201706437.

(15) Khan, U.; Luo, Y.; Tang, L.; Teng, C.; Liu, J.; Liu, B.; Cheng, H. M. Controlled Vapor–Solid Deposition of Millimeter-Size Single Crystal 2D Bi2O2Se for High-Performance Phototransistors. Adv Funct Mater 2019, 29 (14), 1807979. https://doi.org/10.1002/ADFM.201807979.

(16) Luo, P.; Zhuge, F.; Wang, F.; Lian, L.; Liu, K.; Zhang, J.; Zhai, T. PbSe Quantum Dots Sensitized High-Mobility Bi2O2Se Nanosheets for High-Performance and Broadband Photodetection Beyond 2 Mm. ACS Nano 2019, 13 (8), 9028–9037. https://doi.org/10.1021/ACSNANO.9B03124.

(17) Hong, C.; Tao, Y.; Nie, A.; Zhang, M.; Wang, N.; Li, R.; Huang, J.; Huang, Y.; Ren, X.; Cheng, Y.; Liu, X. Inclined Ultrathin Bi2O2Se Films: A Building Block for Functional van Der Waals Heterostructures. ACS Nano 2020, 14 (12). https://doi.org/10.1021/acsnano.0c05300.

(18) Hossain, M. T.; Giri, P. K. Temperature-Dependent Raman Studies and Thermal Conductivity of Direct CVD Grown Non-van Der Waals Layered Bi2O2Se. J Appl Phys 2021, 129 (17), 175102. https://doi.org/10.1063/5.0049368.

(19) Liang, Y.; Chen, Y.; Sun, Y.; Xu, S.; Wu, J.; Tan, C.; Xu, X.; Yuan, H.; Yang, L.; Chen, Y.; Gao, P.; Guo, J.; Peng, H. Molecular Beam Epitaxy and Electronic Structure of Atomically Thin Oxyselenide Films. Advanced Materials 2019, 31 (39), 1901964. https://doi.org/10.1002/ADMA.201901964.

(20) Song, Y.; Li, Z.; Li, H.; Tang, S.; Mu, G.; Xu, L.; Peng, W.; Shen, D.; Chen, Y.; Xie, X.; Jiang, M. Epitaxial Growth and Characterization of High Quality Bi2O2Se Thin Films on SrTiO3 Substrates by Pulsed Laser Deposition. Nanotechnology 2020, 31 (16), 165704. https://doi.org/10.1088/1361-6528/AB6686.

(21) Gao, M.; Wei, W.; Han, T.; Li, B.; Zeng, Z.; Luo, L.; Zhu, C. Defect Engineering in Thickness-Controlled Bi2O2Se-Based Transistors by Argon Plasma Treatment. ACS Appl Mater Interfaces 2022. https://doi.org/10.1021/ACSAMI.1C24260.

(22) Tian, X.; Luo, H.; Wei, R.; Zhu, C.; Guo, Q.; Yang, D.; Wang, F.; Li, J.; Qiu, J. An Ultrabroadband Mid-Infrared Pulsed Optical Switch Employing Solution-Processed Bismuth Oxyselenide. Advanced Materials 2018, 30 (31), 1801021. https://doi.org/10.1002/ADMA.201801021.

(23) Ghosh, T.; Samanta, M.; Vasdev, A.; Dolui, K.; Ghatak, J.; Das, T.; Sheet, G.; Biswas, K. Ultrathin Free-Standing Nanosheets of Bi2O2Se: Room Temperature Ferroelectricity in Self-Assembled Charged Layered Heterostructure. Nano Lett 2019, 19 (8), 5703–5709. https://doi.org/10.1021/ACS.NANOLETT.9B02312.

(24) Li, M. Q.; Dang, L. Y.; Wang, G. G.; Li, F.; Han, M.; Wu, Z. P.; Li, G. Z.; Liu, Z.; Han, J. C. Bismuth Oxychalcogenide Nanosheet: Facile Synthesis, Characterization, and Photodetector Application. Adv Mater Technol 2020, 5 (7), 2000180. https://doi.org/10.1002/ADMT.202000180.

(25) Dang, L. Y.; Liu, M.; Wang, G. G.; Zhao, D. Q.; Han, J. C.; Zhu, J. Q.; Liu, Z. Organic Ion Template-Guided Solution Growth of Ultrathin Bismuth Oxyselenide with Tunable Electronic Properties for Optoelectronic Applications. Adv Funct Mater 2022, 32 (31), 2201020. https://doi.org/10.1002/ADFM.202201020.

(26) Fu, Q.; Zhu, C.; Zhao, X.; Wang, X.; Chaturvedi, A.; Zhu, C.; Wang, X.; Zeng, Q.; Zhou, J.; Liu, F.; Tay, B. K.; Zhang, H.; Pennycook, S. J.; Liu, Z. Ultrasensitive 2D Bi2O2Se Phototransistors on Silicon Substrates. Advanced Materials 2019, 31 (1), 1804945. https://doi.org/10.1002/ADMA.201804945.

(27) Wu, Z.; Liu, G.; Wang, Y.; Yang, X.; Wei, T.; Wang, Q.; Liang, J.; Xu, N.; Li, Z.; Zhu, B.; Qi, H.; Deng, Y.; Zhu, J. Seed-Induced Vertical Growth of 2D Bi2O2Se Nanoplates by Chemical Vapor Transport. Adv Funct Mater 2019, 29 (50). https://doi.org/10.1002/ADFM.201906639.

(28) Kim, U. J.; Nam, S. H.; Seo, J.; Yang, M.; Fu, Q.; Liu, Z.; Son, H.; Lee, M.; Hahm, M. G. Visualizing Line Defects in Non-van Der Waals Bi2O2Se Using Raman Spectroscopy. ACS Nano 2022, 16 (3), 3637–3646. https://doi.org/10.1021/ACSNANO.1C06598.

(29) Han, M.; Wu, S.; Zhao, X.; He, Q.; Zhang, B.; Xiong, W.; Luo, X.; Zheng, Y. Raman Spectroscopy of the Trapezoidal Bi2O2Se. Adv Opt Mater 2023, 11 (15), 2300344. https://doi.org/10.1002/ADOM.202300344.

(30) Cheng, T.; Tan, C.; Zhang, S.; Tu, T.; Peng, H.; Liu, Z. Raman Spectra and Strain Effects in Bismuth Oxychalcogenides. Journal of Physical Chemistry C 2018, 122 (34), 19970–19980. https://doi.org/10.1021/ACS.JPCC.8B05475.

(31) Wu, J.; Tan, C.; Tan, Z.; Liu, Y.; Yin, J.; Dang, W.; Wang, M.; Peng, H. Controlled Synthesis of High-Mobility Atomically Thin Bismuth Oxyselenide Crystals. Nano Lett 2017, 17 (5), 3021–3026. https://doi.org/10.1021/ACS.NANOLETT.7B00335.

(32) Haley, K. L.; Cloninger, J. A.; Cerminara, K.; Sterbentz, R. M.; Taniguchi, T.; Watanabe, K.; Island, J. O. Heated Assembly and Transfer of Van Der Waals Heterostructures with Common Nail Polish. Nanomanufacturing 2021, Vol. 1, Pages 49-56 2021, 1 (1), 49–56. https://doi.org/10.3390/NANOMANUFACTURING1010005.

(33) Kufer, D.; Konstantatos, G. Highly Sensitive, Encapsulated MoS2 Photodetector with Gate Controllable Gain and Speed. Nano Lett 2015, 15 (11), 7307–7313. https://doi.org/10.1021/ACS.NANOLETT.5B02559.

(34) Fan, S.; Yang, W.; Yang, H.; Wu, Y.; Deng, J.; Zhang, J.; Liu, X. Out-of-Plane Bi2O2Se Nanoflakes for Sensitive Gate-Tunable Phototransistors. Adv Opt Mater 2023, 2300740. https://doi.org/10.1002/ADOM.202300740.

(35) Lopez-Sanchez, O.; Lembke, D.; Kayci, M.; Radenovic, A.; Kis, A. Ultrasensitive Photodetectors Based on Monolayer MoS2. Nature Nanotechnology 2013 8:7 2013, 8 (7), 497–501. https://doi.org/10.1038/nnano.2013.100.

(36) Tamalampudi, S. R.; Lu, Y. Y.; Kumar U., R.; Sankar, R.; Liao, C. Da; Moorthy B., K.; Cheng, C. H.; Chou, F. C.; Chen, Y. T. High Performance and Bendable Few-Layered InSe Photodetectors with Broad Spectral Response. Nano Lett 2014, 14 (5), 2800–2806. https://doi.org/10.1021/NL500817G.

(37) Zhou, X.; Gan, L.; Tian, W.; Zhang, Q.; Jin, S.; Li, H.; Bando, Y.; Golberg, D.; Zhai, T.; Zhou, X.; Gan, L.; Zhang, Q.; Li, H.; Zhai, T.; Tian, W.; Jin, S.; Bando, Y.; Golberg, D. Ultrathin SnSe2 Flakes Grown by Chemical Vapor Deposition for High-Performance Photodetectors. Advanced Materials 2015, 27 (48), 8035–8041. https://doi.org/10.1002/ADMA.201503873.

(38) Narayanan P., V.; Gokul, M. A.; Chowdhury, T.; Singh, C. K.; Chaubey, S. K.; Taniguchi, T.; Watanabe, K.; Kabir, M.; Kumar, G. V. P.; Rahman, A. Giant Photoresponse Enhancement in Mixed-Dimensional Van Der Waals Heterostructure through Dielectric Engineering. Adv Mater Interfaces 2022, 9 (9), 2102054. https://doi.org/10.1002/ADMI.202102054.

(39) Wu, J.; Wei, M.; Mu, J.; Ma, H.; Zhong, C.; Ye, Y.; Sun, C.; Tang, B.; Wang, L.; Li, J.; Xu, X.; Liu, B.; Li, L.; Lin, H. High-Performance Waveguide-Integrated Bi2O2Se Photodetector for Si Photonic Integrated Circuits. ACS Nano 2021, 15 (10), 15982–15991. https://doi.org/10.1021/ACSNANO.1C04359.

(40) Han, J.; Fang, C.; Yu, M.; Cao, J.; Huang, K. A High-Performance Schottky Photodiode with Asymmetric Metal Contacts Constructed on 2D Bi2O2Se. Adv Electron Mater 2022, 8 (7), 2100987. https://doi.org/10.1002/AELM.202100987.

(41) Wu, J.; Liu, Y.; Tan, Z.; Tan, C.; Yin, J.; Li, T.; Tu, T.; Peng, H. Chemical Patterning of High-Mobility Semiconducting 2D Bi2O2Se Crystals for Integrated Optoelectronic Devices. Advanced Materials 2017, 29 (44), 1704060. https://doi.org/10.1002/ADMA.201704060.

(42) Yang, H.; Chen, W.; Zheng, X.; Yang, D.; Hu, Y.; Zhang, X.; Ye, X.; Zhang, Y.; Jiang, T.; Peng, G.; Zhang, X.; Zhang, R.; Deng, C.; Qin, S. Near-Infrared Photoelectric Properties of Multilayer Bi2O2Se Nanofilms. Nanoscale Res Lett 2019, 14 (1), 1–6. https://doi.org/10.1186/S11671-019-3179-4.

(43) Kang, M.; Chai, H. J.; Jeong, H. B.; Park, C.; Jung, I. Y.; Park, E.; Çiçek, M. M.; Lee, I.; Bae, B. S.; Durgun, E.; Kwak, J. Y.; Song, S.; Choi, S. Y.; Jeong, H. Y.; Kang, K. Low-Temperature and High-Quality Growth of Bi2O2Se Layered Semiconductors via Cracking Metal-Organic Chemical Vapor Deposition. ACS Nano 2021, 15 (5), 8715–8723. https://doi.org/10.1021/ACSNANO.1C00811.

(44) Liu, X.; Li, R.; Hong, C.; Huang, G.; Pan, D.; Ni, Z.; Huang, Y.; Ren, X.; Cheng, Y.; Huang, W. Highly Efficient Broadband Photodetectors Based on Lithography-Free Au/Bi2O2Se/Au Heterostructures. Nanoscale 2019, 11 (43), 20707–20714. https://doi.org/10.1039/C9NR06723J.

(45) Pang, X.; Zhao, Y.; Gao, X.; Wang, G.; Sun, H.; Yin, J.; Zhu, J. Two-Step Colloidal Synthesis of Micron-Scale Bi2O2Se Nanosheets and Their Electrostatic Assembly for Thin-Film Photodetectors with Fast Response. Chinese Chemical Letters 2021, 32 (10), 3099–3104. https://doi.org/10.1016/J.CCLET.2021.03.039.

Chapter 4

Carrier Density Induced Metal-Insulator Transition in Bi_2O_2Se Nanosheets

4.1 Introduction.

Metal-insulator transition in two-dimensional systems is an intriguing phenomenon that has raised significant challenges to longstanding theories while also prompting several questions aimed at comprehensively grasping its fundamental origins[1,2]. Numerous experimental and theoretical investigations have revealed the emergence of two primary theories regarding the microscopic genesis of the 2D MIT: disorder-driven classical percolation-based transition[3–10], wherein disorder acts to dampen interactions and the interaction-based quantum phase transition (QPT)[1,2,11–18]. Typically, due to strong carrier-carrier interactions, the QPT happens at 0K between the metallic state (having non-zero conductivity) and the insulating state (zero conductivity). This transition is governed by various external factors like carrier density, magnetic field, and pressure[6,10]. However, it has been recently demonstrated by various research groups that QPT can occur even at elevated temperatures[13–15,19,20]. On the other hand, in case of percolation driven MIT in 2D systems, disorder and screening play a crucial role. Disorder generally originates within these 2D system from defects and charged impurities, which are present within the bulk semiconductors and traps, which are located at the interface between the substrate and semiconductor[3–6,10]. In 2D systems, with decreasing carrier density, the screening effect gradually reduces and becomes highly nonlinear.

Even a slight reduction in carrier density significantly decreases screening, resulting in a highly inhomogeneous 2D system where the electron gas can no longer effectively screen the disorder potential. As opposed to the high carrier density homogeneous scenario, this leads to the creation of a disorder potential landscape with varying strength, causing carriers to be pushed away from high potential points and gather at low potential areas. When the size and number of the disordered regions with depleted carrier density become such that the formation of conducting paths crossing the 2D system is not possible, metal-insulator transition takes place. Depending on the threshold percolation density (n_{th}), the system can behave as an effective metal ($n > n_{th}$) or insulator ($n<n_{th}$)[3].

Recently discovered 2D layered materials are now being more widely acknowledged as strong contenders for studying interactions between carriers and disorder-induced 2D Metal-Insulator Transition (MIT). Research has indicated that modifying the film thickness, using surface passivation, and designing the substrate can allow for the adjustment of carrier-carrier interaction strength and disorder[6,7,13–16,21,22]. For example, interactions between carriers that lead to two-dimensional metal-insulator transitions (2D MITs) have been identified in multilayer WSe_2[14], MoS_2[15,16,22], and ReS_2[13]. while a percolation-based 2D MIT has been discovered in monolayer MoS_2[8]. Intriguingly, a percolation-based 2D MIT was similarly observed in multilayer MoS_2[9]. These conflicting observations regarding 2D MITs in transition metal dichalcogenides (TMDs) prompt questions about their underlying origins, compelling us to delve deeper into the microscopic mechanisms driving these transitions. Thus far, research into 2D MIT in TMDs has been constrained, particularly at low temperatures, due to challenges posed by non-Ohmic contacts and high contact resistance (R_C)[23]. Notably, at lower temperatures, the hindrance of thermal

emission current and thermally assisted tunneling across the Schottky barrier results in elevated R_C and non-Ohmic contact behavior, thereby constraining the exploration of 2D MIT in TMDs[18]. Recently synthesized Bismuth oxyselenide (Bi_2O_2Se) has emerged as a fascinating 2D material due to its exceptionally high mobility, strong environmental stability, moderate bandgap, and high dielectric constant of its native oxide[24–26]. It also features a distinct defect structure where the donor state is positioned above the conduction band, resulting in unique metallicity[27]. Additionally, there is a spatial segregation of electrons from donor sites, mitigating scattering caused by these sites and thereby enhancing mobility[27]. Bi_2O_2Se also has low contact resistance and exhibits ohmic behavior with many contact materials[28], which makes it promising for the exploration of the 2D MIT phenomenon.

In this work, we have studied the electronic transport properties of a few nanometer-thin Bi_2O_2Se nanosheets placed on SiO_2/Si substrates and observed the phenomenon of MIT placed on SiO_2/Si substrates by changing carrier density via back-gate bias. At high carrier density, σ shows n_{2D}^{α} , type dependence with $\alpha \approx 1$, indicating the existence of screened Coulomb impurity scattering. As we decrease the electron density, $n_{2D} < n_{th}$, the system's homogeneity breaks down, resulting in the development of significant charge inhomogeneity and triggering a percolation-based MIT in our system. In the insulating phase, the transport is well described by the thermal activation mechanism. As we increase the carrier density, the Fermi level transitions through the localized trap states below the conduction band to eventually reach the conduction band, resulting in metallic behavior

4.2 Experimental Details

Ultrathin nanosheets of Bi_2O_2Se were grown on f-mica substrate using home-built APCVD. 88 mg of Bi_2O_3 and 44 mg of Bi_2Se_3 mg were used as precursors, which are kept at a separation of 5 cm, and placed in an alumina crucible. The temperature of the CVD furnace was maintained at 700°C during growth for 30 minutes. As grown, Bi_2O_2Se nanosheets were transferred to SiO_2/Si substrate for electrical studies using a nail polish-assisted transfer method, as mentioned in our previous work. For device fabrication, contacts were patterned using standard photolithography using S1813 photoresist and developed by MF319 developer. A (5/60) nm layer of Pd/Au was deposited using sputtering followed by lift-off in acetone. Temperature-dependent electronic transport measurements were performed in a cryo-free closed-cycle cryostat (Janis Research) system from 300 K (room temperature) down to 12 K. Temperature was controlled with the help of Lakeshore 335 temperature controller. Keithley 2614B source meter was used to do the electrical measurements.

4.3 Results and Discussion

4.3.1 Electrical Characterisation at Room Temperature

We have grown Bi_2O_2Se ultrathin nanosheets on f-mica substrates using our homebuilt Atmospheric pressure chemical vapor deposition (APCVD) system, as mentioned in Chapter 3. For studying electrical transport properties, we have transferred as-grown Bi_2O_2Se nanosheets on f-mica to SiO_2/Si substrates using a nail polish-assisted transfer technique and fabricated back-gated devices using photolithography followed by metal deposition (Pd/Au) using sputtering. Figure 4.1a shows the optical microscope (OM) image of our representative back-gated device. All the devices were vacuum annealed at 200℃ for 2 hours, as it improved the electrical properties significantly. In Figure 4.1b, Linear I-V demonstrates ohmic contacts between Pd and Bi_2O_2Se.

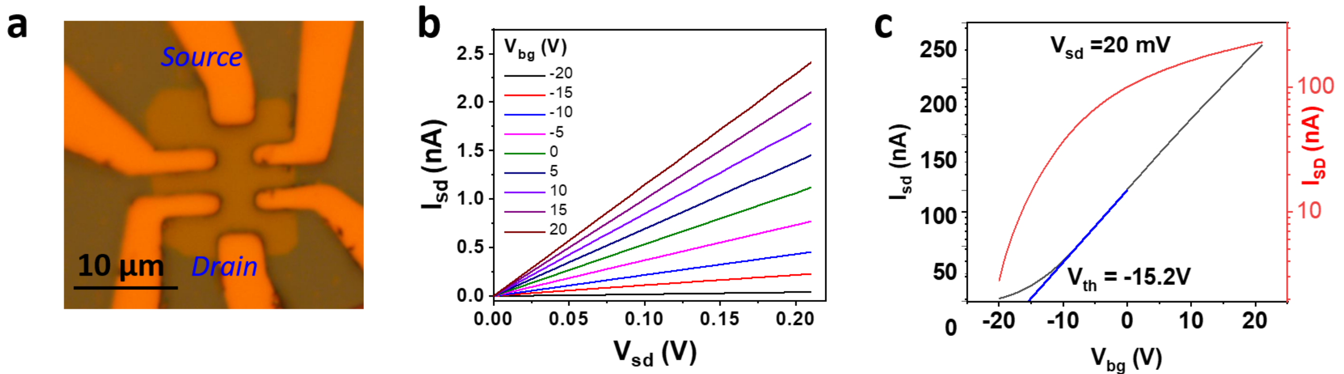

Figure 4.1: (a) OM image of our representative device in which Pd/Au are used as contacts. (b) Source drain current (Isd) as a function of source-drain voltage (V_{sd}) at different back gate voltage (-20V<Vg>20V) (c) I_{ds} as a function of V_g at constant V_{sd} of 20mV. The Y-axis (Black) corresponds to the linear scale, whereas the Y-axis red corresponds to the log scale.

Figure 4.1c displays the gate scan of our device at 300 K. Our back gated device shows n-type

behavior, an on /off ratio of 10^2, and a threshold voltage of -15.2V. The threshold voltage (Vth) has been extracted from the linear portion of the transfer curve as shown in figure 4.1c.

Subthreshold swing (SS) was determined from the subthreshold region (Vg < Vth) of transfer characteristics using the following equation, and it was found to be 6.2V /decade.

$$SS = \left[\left| \frac{\partial \log I_d}{\partial V_g} \right| \right]^{-1}$$

SS should ideally be 60 meV at room temperature[29], with any departure from this value ascribed to defects or impurities in the channel-substrate interface or in the channel itself. This deviation leads to the creation of a midgap state that functions as a localized state for trapping charge carriers [6,30,31]. Localized trap states are essential for the operation of various electronic and optoelectronic devices as they have the ability to capture and confine charge carriers, which can be subsequently released through the application of additional energy (such as light or thermal energy) or through processes like and thermally activated hopping and tunneling between localized states[6]. The density of the localized state can be determined from SS, and for our system, it was found to be 7.2×10^{12} cm^{-2} ev^{-1}. Field effect mobility (μ) is extracted from the linear portion of the transfer characteristics in the super threshold region (Vg >Vth) with the expression $\mu = (L/W)\ (1/C_g)\ (1/V_{ds})\ (dI_{ds}/dV_g)$ where W is the channel width, L is the channel length and C_g is the gate capacitance per unit area. We estimated $\mu \approx 86.5\ cm^{-2}V^{-1}s^{-1}$.

All the devices were vacuum annealed at 200°C for 2 hours, which significantly improved their electrical properties. Figures 4.2a and 4.2b display the IV characteristics of our device before and

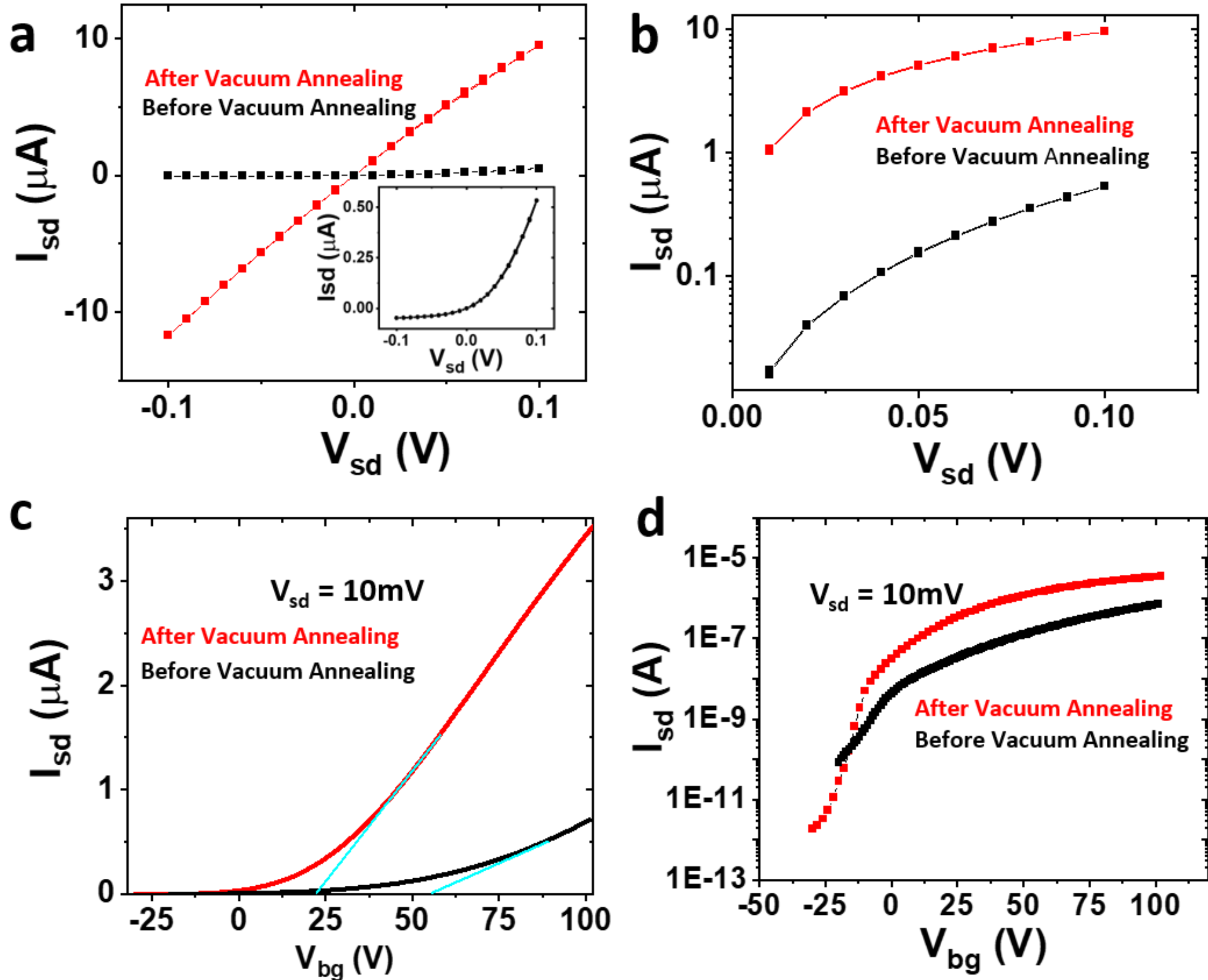

Figure 4.2 (a) IV characteristic before and after Vacuum Annealing at 200°C for 2 hours of our 10nm thick Bi_2O_2Se device. The inset shows the IV without back gate bias before Vacuum annealing. Before vacuum annealing, IV characteristics showed Schottky behaviour, which became linear after vacuum annealing. (b) IV characteristics before and after vacuum annealing were measured on a semi-log scale. (**c**) Transfer characteristics before and after the Vacuum Annealing of our device. (d) Transfer characteristics before and after the Vacuum Annealing in semi-log scale.

after vacuum annealing in linear and semi-log scales, respectively. Prior to vacuum annealing, the

IV characteristics exhibited Schottky behavior, which transitioned to linear behavior after the annealing process (Figure 4.2a). Additionally, Source- Drain current I_{sd}, increased by 2 orders of magnitude after vacuum annealing (Figure 4.2b). The field effect mobility also increased from 100 to 260 $cm^2V^{-1}s^{-1}$ (Figure 4.2c). Furthermore, the on-off ratio in the transfer characteristics increased from 10^4 to 10^6 before and after vacuum annealing (Figure 4.2d).

4.3.2 Temperature Dependent Electronic Transport Properties

Figure 4.3 presents the temperature dependence of transport characteristics of our devices of thickness 3 nm and 10 nm S1 and S2, respectively, measured across a broad temperature range (12K-300K**).** Transfer characteristics of devices S1 and S2 at various temperatures are illustrated in Figure 4.3a and Figure 4.3b, respectively. A more negative threshold voltage is observed for device 1 compared to device 2, indicating that it is more n-doped than device 1. Notably, the transfer characteristics exhibit n-type behavior throughout the entire temperature range, attributed to the presence of selenium vacancies. Our devices do not exhibit any gate hysteresis in transfer characteristics. An observed crossover in transfer characteristics across a range of temperatures is linked to the transition between insulating and metallic behavior induced by carrier density[13,32]. Figure 4.4 displays the output characteristics of our devices at different Temperatures. We have done four probe IV measurements at 25 K and 298 K and compared them with two probe Measurements on the same device (Figure A2). Both show linear behavior with the same

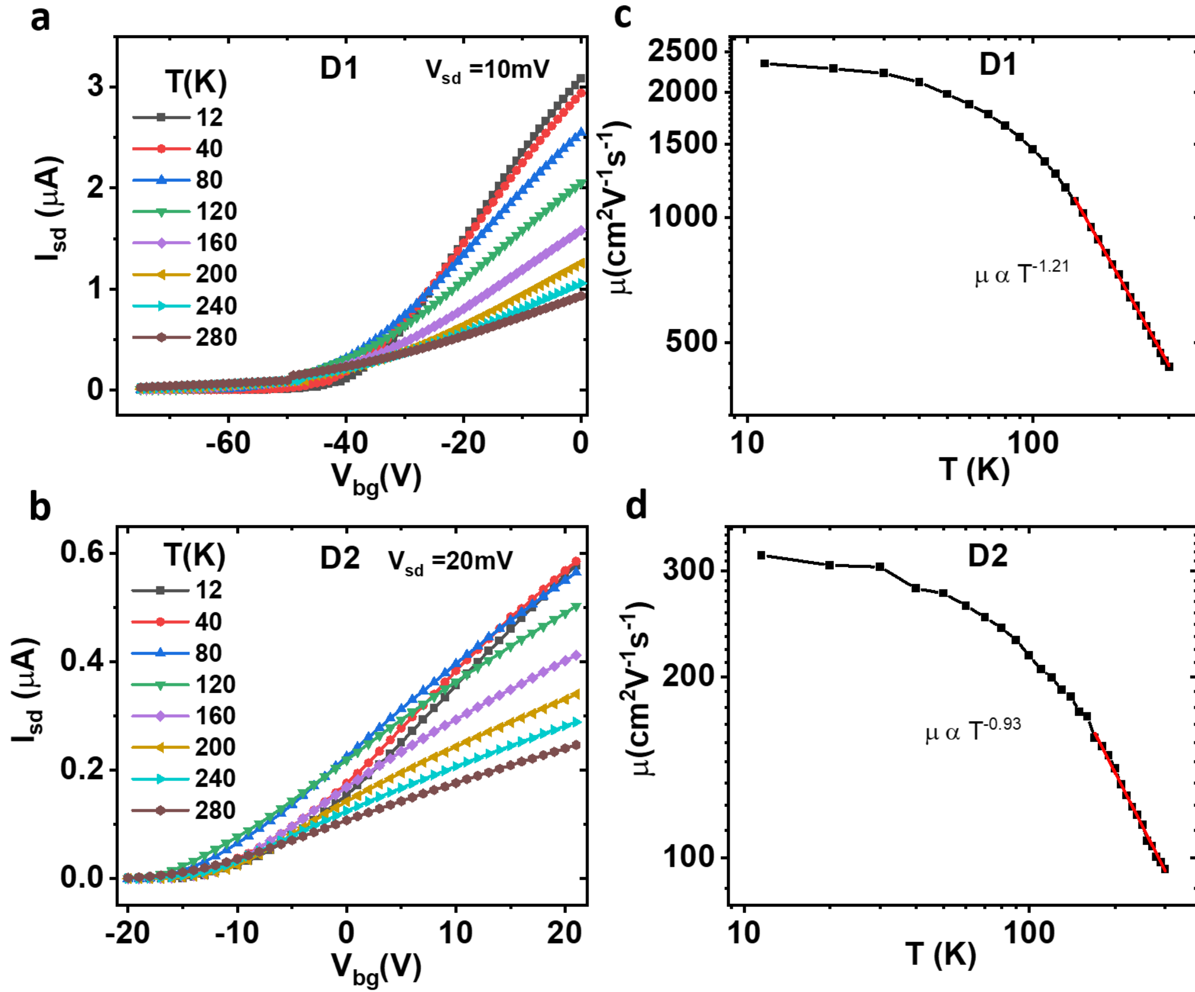

Figure 4.3: (a) Transfer characteristics (I_{sd} Vs V_{bg}) under constant Vsd =10mV of device D1 for temperatures ranging from 12K to 300K. (b) Transfer characteristics (I_{sd} Vs V_{bg}) under constant V_{sd} =20mV of device D2 for temperatures ranging from 12K to 300K (c) and (d) Plot of Field effect mobility as a function of temperature in log-log scale of Device D1 and D2 respectively.

conductance value. Our devices show linear IV even at low temperatures, implying ohmic contact in contrast to Schottky behavior generally observed in TMDs. Figure 4.3c displays the two probe Field effect mobility (μ) as a function of temperature in a log-log scale. Our devices display strong

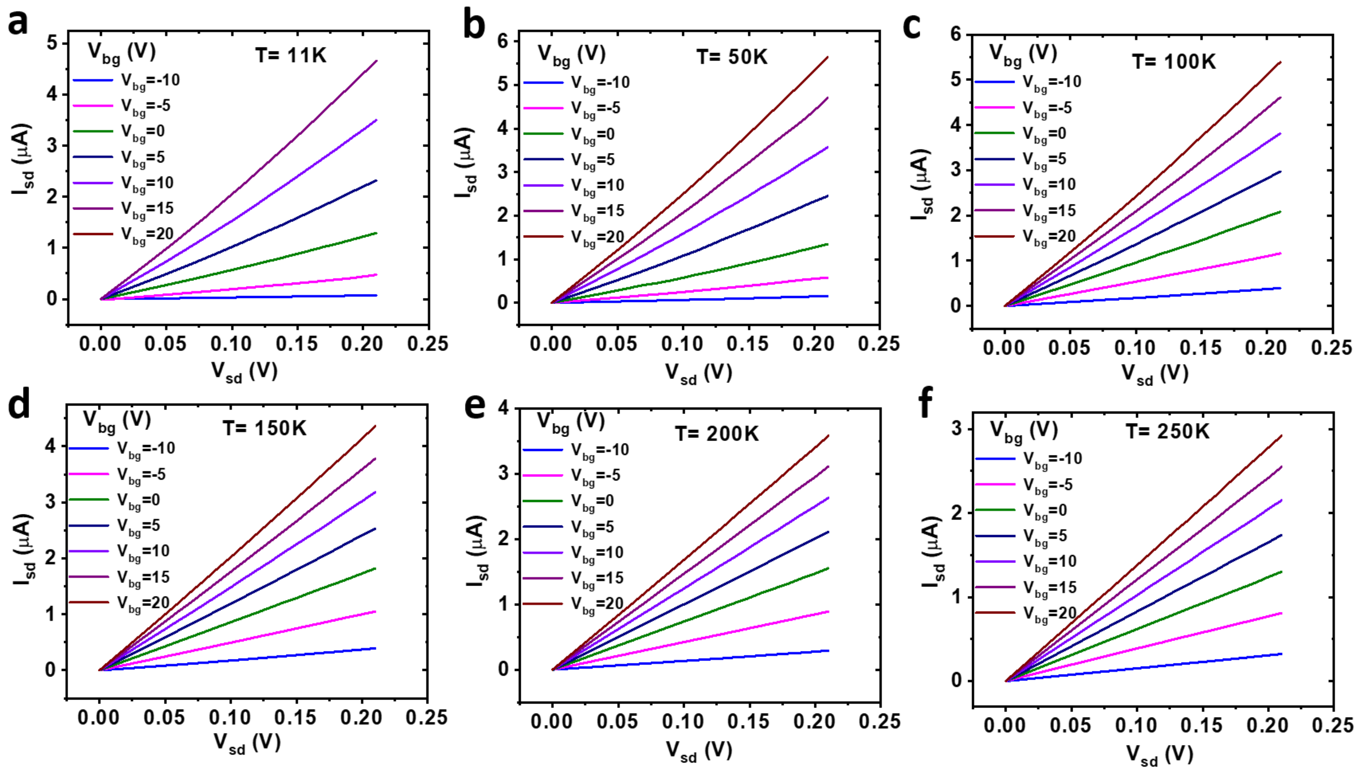

Figure 4.4: Output characteristic of our device at (a) 11K, (b) 50K, (c) 100K, (d) 150K, (e) 200K, and (f) 250K. IV characteristics is linear at all temperature even at 11 K rules out the effect of contact resistance on the transport properties of our devices.

temperature dependence on mobility. For temperatures exceeding 100 K, field-effect mobility increases as temperature decreases. We have fitted the mobility Vs temperature plot to a power law $\mu \propto T^{-\gamma}$ where the value of exponent γ denotes the strength of the phonon scattering mechanism[13]. From this fitting, we extracted $\gamma = 1.21$, which corresponds to electron-phonon scattering. Electron mobility of a 2D channel FET typically depends upon multiple scattering mechanisms. The maximum electron mobility is theoretically limited by intrinsic electron-phonon scattering, known as phonon-limited mobility. However, in advanced devices, observed mobility

values are predominantly restricted by external influences such as charge traps, coulomb impurities, defects, and surface optical phonons, which lead to values significantly below the theoretically predicted phonon-limited values. Over time, various methods have been used to lessen the impact of electron scattering caused by these external factors[6].

4.3.3 Metal-Insulator Transition

Figure 4.5a displays the behavior of the two probe conductivity of our device as a function of temperature at different back gate voltages. We have observed metal-insulator transition in our devices by tuning carrier density using back gate voltage. At low back gate bias or lower carrier density, two probe conductivity increases with temperature (12K<T<110K), showing insulating behavior. After 110K, it decreases with increasing temperature (110K<T<210K), showing metallic behavior again at higher temperatures (210K<T<300K), conductivity increases with increasing temperature, displaying insulating behavior. At higher gate voltage, conductivity decreases with increasing temperature over the entire temperature range, displaying metal like behavior.

The MIT behavior in our system was analyzed through the lens of the thermal activation behavior and temperature scaling percolation theory. In the low-temperature regime (12K<T<110K), conductivity in the insulating regime can be well modeled by thermally activated behavior. Activation energies have been determined by fitting sheet conductivity (G) with the expression $G = G_0 \exp\left(\frac{-E_a}{k_B T}\right)$, where G_0 is a constant, Ea is the activation energy, and k_B is the Boltzmann

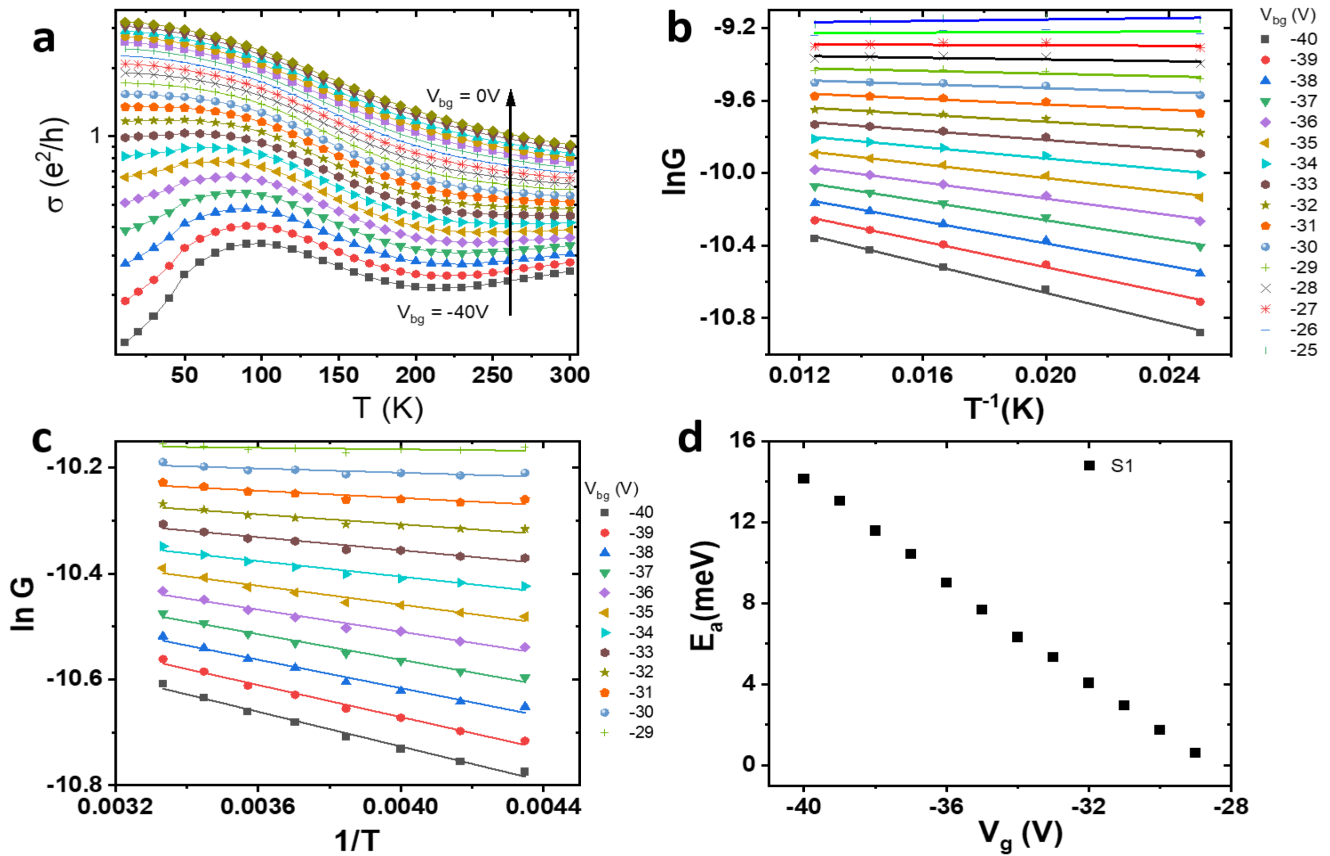

Figure 4.5: (a) Two probe conductivity $\sigma = (I_{sd}/V_{sd})(L/W)$ in units of e^2/h as a function of temperature (b) Plot of ln G vs 1/T for the device at the different back gate voltage in the low-temperature regime (12K<T<110K) (c) In the high-temperature regime (210K<T <300K) linear fitting of the plot tells the transport is well described by thermal Activation mechanism (d) Activation energy extracted from the figure 4c as a function of back gate voltage.

constant [33]. This Activation energy corresponds to the thermal activation of electrons into the conduction band edge (E_C) from the Fermi level (E_F). Figure 4.5b shows the plot of ln G vs 1/T at

different back gate voltages. The linear fitting confirms thermal activation behavior. Activation energy decreases as the gate voltage increases, and the Fermi level moves slowly through the localized trap state[34]. After increasing the gate voltage further, the Fermi level goes to the conduction band, and carriers show metal-like behavior. Above 110K, phonon scattering increases with an increase in temperature. As a result, conductivity decreases with an increase in temperature, which results in metal like behavior.

In the Temperature range (210K<T<300K), thermally activated transport can also explain conductivity in the insulating regime. Figure 4.5c shows the plot of ln G vs. T. The linear fitting confirms activated behavior. Figure 4.5d shows the plot of ln G vs. T. As discussed earlier, with increasing gate voltage, activation energy decreases, and further increment of the gate voltage results in moving the Fermi level into the conduction band through the localized trap states, resulting in metallic behavior. Activation energy is significantly higher than the low temperature for this temperature range. The density of these trap states (N_F) is determined by analyzing the gate voltage dependency of the thermal activation energy (Figure 4.3d) and taking into account the quantum capacitance C_d[33,35,36] using the following relation.

$$\frac{dE_F}{dV_g} = \frac{-dE_a}{dV_g} = \frac{eC_g}{C_g + C_d}$$

Where $C_d = e^2N_F$, In our case $N_F = 4.7 \times 10^{12} eV^{-1}cm^{-2}$.

4.3.4 Percolation Driven Transition

Various 2D materials have shown MIT due to electrostatic doping[13,15,22,32,37]. In the presence of localized states, the strength of Coulomb interaction is characterized by Weigner-Seitz radius (r_s), which is defined as the ratio of potential (Coulomb, E_C) and kinetic (Fermi, E_F) energy by following relation.

$$r_s = \frac{E_C}{E_F} = \frac{n_v}{a_B^* \sqrt{n_{2D}}} = \frac{n_v m^* e^2}{4\pi\varepsilon\hbar^2 \sqrt{\pi n_{2D}}}$$

Where n_v is the number of valleys, e is the electronic charge, m* is the effective mass of the electron, and ε is the static dielectric constant. Previously, both experimental and theoretical studies have demonstrated that, in the presence of weak disorder and strong interaction where $r_s >$ 1, a 2D system can transition from an insulating to a metallic regime as the charge carrier density (n_{2D}) is raised above a threshold density (n_{th})[38,39] monolayer MoS_2 have an effective mass of electron $m^* = 0.45m_e$ and static dielectric constant of $\varepsilon = 7.3\varepsilon_0$, using these $r_s \sim 4.2$ satisfies for high threshold density of $n_{th} \sim 10^{13}$ cm^{-2}, which requires the use of high-κ dielectric (HfO_2) for the observation of MIT[22]. Bi_2O_2Se has a low effective mass $m^* = 0.14m_e$ [24] and high static dielectric constant ($\varepsilon = 195\varepsilon_0$)[40], and the condition $r_s > 1$ can be fulfilled at a relatively lower threshold carrier density of $n_{th} \sim 10^{10}$ cm^{-2}, which suggests the potential for an MIT in Bi_2O_2Se using a conventional SiO_2 dielectric back gate.

We have examined the behavior of MIT in Bi_2O_2Se through the lens of percolation-driven MIT. In our system, at higher carrier densities, the conductivity follows the following relationship $\sigma = n_{2D}^{\alpha}$. Our device exhibits an α value close to 1 (see Figure 4.6f) across all temperatures, indicating

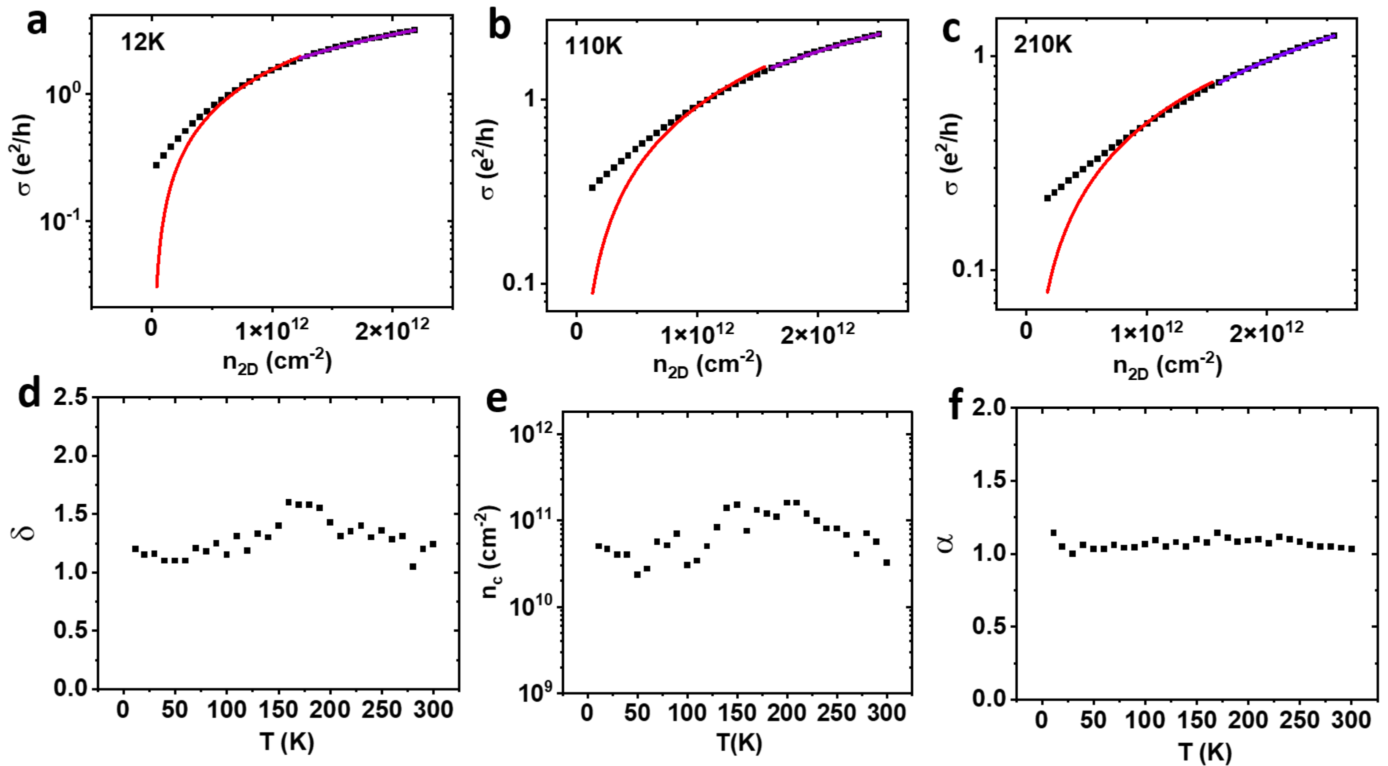

Figure 4.6: Plot for 2 probe conductivity of our device as a function of carrier density at (a) 10K, (b)110K, and (c) 210K red line indicates the 2D percolation fitting to $\sigma = A\,(n_{2D} - n_{th})^{\delta}$ and violet line indicates the Boltzmann theory fit to $\sigma = n_{2D}^{\alpha}$. (d) percolation exponent δ, (e) percolation threshold density n_{th} and (f) conductivity exponent α as a function of temperature.

high conductivity behavior consistent with classical Boltzmann theory. This suggests that linearly screened Coulomb impurity scattering is the primary limiter of conductivity. the exponent α is

significantly influenced by n_{2D} at lower carrier densities. This discrepancy suggests that the screening in a homogeneous electron gas does not fully account for the conductivity behavior at lower carrier densities, although at higher carrier densities it provides qualitatively accurate predictions.

Prior theoretical investigations have revealed that the homogeneous screening of charge impurities in 2D systems deteriorates rapidly at low carrier density, resulting in pronounced charge inhomogeneity. This phenomenon leads to a transition when $n_{2D} = n_{th}$ driven by percolation. During such transition, the carrier density (n_{2D}) dependence of conductivity for 2D systems can be expressed as $\sigma(n_{2D}) = A(n_{2D} - n_{th})^{\delta}$, where δ is a percolation exponent having value 1.33 for the 2D system[3,5]. At $n_{2D} < n_{th}$, the continuity of the conducting pathways is disrupted by charge inhomogeneities due to the formation of charge puddles in the potential valleys. This process is responsible for the emergence of the insulating states.

The measured two-probe conductivity as a function of n_{2D} for different temperatures is depicted in Figure 4. The value of n_{2D} was calculated with the help of a parallel plate capacitor model using the expression $n_{2D} = C_{ox}\Delta V_g/e$ with C_{ox} representing the oxide capacitance and ΔV_g denoting, $\Delta V_g = V_g - V_{th}$[22]. Both Boltzmann fit and percolation critical behavior analyses were conducted for all measured conductivities across the temperature range under investigation. Some of these curves are shown in Figures 4.6a, 4.6b, and 4.6c. while Figures 4.6d, 4.6e, and 4.6f display the extracted values of δ , n_{th} and α, respectively. The extracted average value of percolation exponent $\delta = 1.28$

in our devices matches well with the theoretical value of 1.33, confirming percolation-based MIT in Bi_2O_2Se nanosheets.

4.4 Summary

By tuning the carrier density, we observed the novel phenomena of MIT in our multilayer Bi_2O_2Se back-gated FETs. At high carrier density, we performed Boltzmann fitting $\sigma = n_{2D}^{\alpha}$, our system displayed $\alpha \approx 1$, over the entire studied temperature range, indicating the existence of linearly screened charged impurity scattering. At low density ($n_{2D} < n_{th}$), this homogeneous screening of electron gas breaks down, resulting in the development of strong charge inhomogeneity, which leads to a percolation-based MIT transition in our system. At low density, we performed percolation fitting and extracted value of average percolation exponent $\delta = 1.28$ are in excellent agreement with the theoretical value of 1.33 for 2D electron system. In the insulating phase, the transport behavior is explained by using thermal activation mechanism. Increasing the carrier density causes the Fermi level to transition from localized trap states located below the conduction band to the conduction band itself, resulting in metallic behavior.

Bibliography

(1) Kravchenko, S. V.; Kravchenko, G. V.; Furneaux, J. E.; Pudalov, V. M.; D'Iorio, M. Possible Metal-Insulator Transition at B=0 in Two Dimensions. *Phys Rev B* **1994**, *50* (11), 8039–8042. https://doi.org/10.1103/PhysRevB.50.8039.

(2) Kravchenko, S. V.; Mason, W. E.; Bowker, G. E.; Furneaux, J. E.; Pudalov, V. M.; Diorio, M. Scaling of an Anomalous Metal-Insulator Transition in a Two-Dimensional System in Silicon at B=0. *Phys Rev B* **1995**, *51* (11), 7038–7045. https://doi.org/10.1103/PhysRevB.51.7038.

(3) Das Sarma, S.; Lilly, M. P.; Hwang, E. H.; Pfeiffer, L. N.; West, K. W.; Reno, J. L. Two-Dimensional Metal-Insulator Transition as a Percolation Transition in a High-Mobility Electron System. *Phys Rev Lett* **2005**, *94* (13). https://doi.org/10.1103/PHYSREVLETT.94.136401.

(4) Manfra, M. J.; Hwang, E. H.; Das Sarma, S.; Pfeiffer, L. N.; West, K. W.; Sergent, A. M. Transport and Percolation in a Low-Density High-Mobility Two-Dimensional Hole System. *Phys Rev Lett* **2007**, *99* (23). https://doi.org/10.1103/PHYSREVLETT.99.236402.

(5) Meir, Y. Percolation-Type Description of the Metal-Insulator Transition in Two Dimensions. *Phys Rev Lett* **1999**, *83* (17), 3506. https://doi.org/10.1103/PhysRevLett.83.3506.

(6) Patil, P. D.; Ghosh, S.; Wasala, M.; Lei, S.; Vajtai, R.; Ajayan, P. M.; Ghosh, A.; Talapatra, S. Gate-Induced Metal-Insulator Transition in 2D van Der Waals Layers of Copper Indium Selenide Based Field-Effect Transistors. *ACS Nano* **2019**. https://doi.org/10.1021/ACSNANO.9B06846.

(7) Ali, F.; Ali, N.; Taqi, M.; Ngo, T. D.; Lee, M.; Choi, H.; Park, W. K.; Hwang, E.; Yoo, W. J. Metal–Insulator Transition Driven by Traps in 2D WSe2 Field-Effect Transistor. *Adv Electron Mater* **2022**, *8* (9), 2200046. https://doi.org/10.1002/AELM.202200046.

(8) Moon, B. H.; Bae, J. J.; Han, G. H.; Kim, H.; Choi, H.; Lee, Y. H. Anomalous Conductance near Percolative Metal-Insulator Transition in Monolayer MoS2 at Low Voltage Regime. *ACS Nano* **2019**, *13* (6), 6631–6637. https://doi.org/10.1021/ACSNANO.9B00755.

(9) Chen, X.; Wu, Z.; Xu, S.; Wang, L.; Huang, R.; Han, Y.; Ye, W.; Xiong, W.; Han, T.; Long, G.; Wang, Y.; He, Y.; Cai, Y.; Sheng, P.; Wang, N. Probing the Electron States and Metal-Insulator Transition Mechanisms in Molybdenum Disulphide Vertical Heterostructures. *Nature Communications 2015 6:1* **2015**, *6* (1), 1–8. https://doi.org/10.1038/ncomms7088.

(10) Ali, N.; Lee, M.; Ali, F.; Ngo, T. D.; Park, H.; Shin, H.; Yoo, W. J. Percolation-Based Metal-Insulator Transition in Black Phosphorus Field Effect Transistors. *ACS Appl Mater Interfaces* **2023**, *15* (10), 13299–13306. https://doi.org/10.1021/ACSAMI.2C22046.

(11) Kravchenko, S. V.; Sarachik, M. P. Metal-Insulator Transition in Two-Dimensional Electron Systems. *Reports on Progress in Physics* **2004**, *67* (1), 1–44. https://doi.org/10.1088/0034-4885/67/1/R01.

(12) Vučičević, J.; Terletska, H.; Tanasković, D.; Dobrosavljević, V. Finite-Temperature Crossover and the Quantum Widom Line near the Mott Transition. *Phys Rev B Condens Matter Mater Phys* **2013**, *88* (7). https://doi.org/10.1103/PHYSREVB.88.075143.

(13) Pradhan, N. R.; Mccreary, A.; Rhodes, D.; Lu, Z.; Feng, S.; Manousakis, E.; Smirnov, D.; Namburu, R.; Dubey, M.; Hight Walker, A. R.; Terrones, H.; Terrones, M.; Dobrosavljevic, V.; Balicas, L. Metal to Insulator Quantum-Phase Transition in Few-Layered ReS 2. *Nano Lett* **2015**, *15*, 2024. https://doi.org/10.1021/acs.nanolett.5b04100.

(14) Stanley, L. J.; Chuang, H. J.; Zhou, Z.; Koehler, M. R.; Yan, J.; Mandrus, D. G.; Popovic, D. Low-Temperature 2D/2D Ohmic Contacts in WSe2 Field-Effect Transistors as a Platform for the 2D Metal-Insulator Transition. *ACS Appl Mater Interfaces* **2021**, *13* (8), 10594–10602. https://doi.org/10.1021/acsami.0c21440.

(15) Moon, B. H.; Bae, J. J.; Joo, M. K.; Choi, H.; Han, G. H.; Lim, H.; Lee, Y. H. Soft Coulomb Gap and Asymmetric Scaling towards Metal-Insulator Quantum Criticality in Multilayer MoS2. *Nature Communications 2018 9:1* **2018**, *9* (1), 1–8. https://doi.org/10.1038/s41467-018-04474-4.

(16) Moon, B. H.; Han, G. H.; Radonjić, M. M.; Ji, H.; Dobrosavljević, V. Quantum Critical Scaling for Finite-Temperature Mott-like Metal-Insulator Crossover in Few-Layered MoS2. *Phys Rev B* **2020**, *102* (24). https://doi.org/10.1103/PhysRevB.102.245424.

(17) Shashkin, A. A.; Kravchenko, S. V. Chapter 2 Metal-Insulator Transition in a Strongly Correlated Two-Dimensional Electron System. *Strongly Correlated Electrons in Two Dimensions* **2017**, 47–64. https://doi.org/10.4324/9781315364575-2.

(18) Ali, N.; Lee, M.; Ali, F.; Shin, H.; Ngo, T. D.; Watanabe, K.; Taniguchi, T.; Oh, B.; Yoo, W. J. Gate-Controlled Metal to Insulator Transition in Black Phosphorus Nanosheet-Based Field Effect Transistors. *ACS Appl Nano Mater* **2022**, *5* (12), 18376–18384. https://doi.org/10.1021/ACSANM.2C04200.

(19) Sato, Y.; Kawasugi, Y.; Suda, M.; Yamamoto, H. M.; Kato, R. Critical Behavior in Doping-Driven Metal–Insulator Transition on Single-Crystalline Organic Mott-FET. *Nano Lett* **2017**, *17* (2), 708–714. https://doi.org/10.1021/acs.nanolett.6b03817.

(20) Furukawa, T.; Miyagawa, K.; Taniguchi, H.; Kato, R.; Kanoda, K. Quantum Criticality of Mott Transition in Organic Materials. *Nature Physics 2014 11:3* **2015**, *11* (3), 221–224. https://doi.org/10.1038/nphys3235.

(21) Moon, B. H. Metal-Insulator Transition in Two-Dimensional Transition Metal Dichalcogenides. *Emergent Mater* **2021**, *4* (4), 989–998. https://doi.org/10.1007/S42247-021-00202-9.

(22) Radisavljevic, B.; Kis, A. Mobility Engineering and a Metal–Insulator Transition in Monolayer MoS2. *Nature Materials 2013 12:9* **2013**, *12* (9), 815–820. https://doi.org/10.1038/nmat3687.

(23) Allain, A.; Kang, J.; Banerjee, K.; Kis, A. Electrical Contacts to Two-Dimensional Semiconductors. *Nature Materials 2015 14:12* **2015**, *14* (12), 1195–1205. https://doi.org/10.1038/nmat4452.

(24) Wu, J.; Yuan, H.; Meng, M.; Chen, C.; Sun, Y.; Chen, Z.; Dang, W.; Tan, C.; Liu, Y.; Yin, J.; Zhou, Y.; Huang, S.; Xu, H. Q.; Cui, Y.; Hwang, H. Y.; Liu, Z.; Chen, Y.; Yan, B.; Peng, H. High Electron Mobility and Quantum Oscillations in Non-Encapsulated Ultrathin Semiconducting Bi2O2Se. *Nature Nanotechnology 2017 12:6* **2017**, *12* (6), 530–534. https://doi.org/10.1038/nnano.2017.43.

(25) Li, T.; Tu, T.; Sun, Y.; Fu, H.; Yu, J.; Xing, L.; Wang, Z.; Wang, H.; Jia, R.; Wu, J.; Tan, C.; Liang, Y.; Zhang, Y.; Zhang, C.; Dai, Y.; Qiu, C.; Li, M.; Huang, R.; Jiao, L.; Lai, K.; Yan, B.; Gao, P.; Peng, H. A Native Oxide High-κ Gate Dielectric for Two-Dimensional Electronics. *Nature Electronics 2020 3:8* **2020**, *3* (8), 473–478. https://doi.org/10.1038/s41928-020-0444-6.

(26) Wu, J.; Tan, C.; Tan, Z.; Liu, Y.; Yin, J.; Dang, W.; Wang, M.; Peng, H. Controlled Synthesis of High-Mobility Atomically Thin Bismuth Oxyselenide Crystals. *Nano Lett* **2017**, *17* (5), 3021–3026. https://doi.org/10.1021/acs.nanolett.7b00335.

(27) Fu, H.; Wu, J.; Peng, H.; Yan, B. Self-Modulation Doping Effect in the High-Mobility Layered Semiconductor Bi2O2Se. *Phys Rev B* **2018**, *97* (24). https://doi.org/10.1103/PhysRevB.97.241203.

(28) Khan, U.; Luo, Y.; Tang, L.; Teng, C.; Liu, J.; Liu, B.; Cheng, H. M. Controlled Vapor–Solid Deposition of Millimeter-Size Single Crystal 2D Bi2O2Se for High-Performance Phototransistors. *Adv Funct Mater* **2019**, *29* (14), 1807979. https://doi.org/10.1002/ADFM.201807979.

(29) Sze, S. M.; Ng, K. K. Physics of Semiconductor Devices. *Physics of Semiconductor Devices* **2006**. https://doi.org/10.1002/0470068329.

(30) Kim, H. J.; Kim, D. H.; Jeong, C. Y.; Lee, J. H.; Kwon, H. I. Determination of Interface and Bulk Trap Densities in High-Mobility p-Type WSe2 Thin-Film Transistors. *IEEE Electron Device Letters* **2017**, *38* (4), 481–484. https://doi.org/10.1109/LED.2017.2673854.

(31) Kalb, W. L.; Batlogg, B. Calculating the Trap Density of States in Organic Field-Effect Transistors from Experiment: A Comparison of Different Methods. *Phys Rev B Condens Matter Mater Phys* **2010**, *81* (3). https://doi.org/10.1103/PhysRevB.81.035327.

(32) Li, X.; Grassi, R.; Li, S.; Li, T.; Xiong, X.; Low, T.; Wu, Y. Anomalous Temperature Dependence in Metal-Black Phosphorus Contact. *Nano Lett* **2018**, *18* (1), 26–31. https://doi.org/10.1021/acs.nanolett.7b02278.

(33) Stankiewicz, J.; Sesé, J.; Balakrishnan, G.; Fisk, Z. Electrical Transport Properties of CaB6. *Phys Rev B Condens Matter Mater Phys* **2014**, *90* (15), 8174–8181. https://doi.org/10.1103/PhysRevB.90.155128.

(34) Ayari, A.; Cobas, E.; Ogundadegbe, O.; Fuhrer, M. S. Realization and Electrical Characterization of Ultrathin Crystals of Layered Transition-Metal Dichalcogenides. *J Appl Phys* **2007**, *101* (1), 14507. https://doi.org/10.1063/1.2407388/917096.

(35) Zhu, W.; Low, T.; Lee, Y. H.; Wang, H.; Farmer, D. B.; Kong, J.; Xia, F.; Avouris, P. Electronic Transport and Device Prospects of Monolayer Molybdenum Disulphide Grown by Chemical Vapour Deposition. *Nature Communications 2014 5:1* **2014**, *5* (1), 1–8. https://doi.org/10.1038/ncomms4087.

(36) Xue, J.; Huang, S.; Wang, J. Y.; Xu, H. Q. Mott Variable-Range Hopping Transport in a MoS2 Nanoflake. *RSC Adv* **2019**, *9* (31), 17885–17890. https://doi.org/10.1039/C9RA03150B.

(37) Moon, B. H.; Bae, J. J.; Han, G. H.; Kim, H.; Choi, H.; Lee, Y. H. Anomalous Conductance near Percolative Metal-Insulator Transition in Monolayer MoS2 at Low Voltage Regime. *ACS Nano* **2019**, *13* (6), 6631–6637. https://doi.org/10.1021/acsnano.9b00755.

(38) Belitz, D.; Kirkpatrick, T. R. The Anderson-Mott Transition. *Rev Mod Phys* **1994**, *66* (2), 261. https://doi.org/10.1103/RevModPhys.66.261.

(39) Castellani, C.; Di Castro, C.; Lee, P. A.; Ma, M. Interaction-Driven Metal-Insulator Transitions in Disordered Fermion Systems. *Phys Rev B* **1984**, *30* (2), 527. https://doi.org/10.1103/PhysRevB.30.527.

(40) Zhu, Z.; Yao, X.; Zhao, S.; Lin, X.; Li, W. Giant Modulation of the Electron Mobility in Semiconductor Bi2O2Se via Incipient Ferroelectric Phase Transition. *J Am Chem Soc* **2022**, *144* (10), 4541–4549. https://doi.org/10.1021/JACS.1C12681.

Chapter 5

Conclusion and Future Directions

5.1 Conclusion

In conclusion, this thesis focuses on synthesizing and studying the electrical transport properties of multilayer Bi_2O_2Se nanosheets for future electronics and optoelectronic applications. We have successfully optimized the growth conditions for synthesizing high-quality Bi_2O_2Se nanosheets using APCVD, and the quality of these samples was characterized using Raman spectroscopy, AFM, OM, and HRTEM. As-grown samples were transferred to SiO_2/Si substrate with the assistance of nail polish without any chemical etching or damage. This way, the devices fabricated with a back-gated structure demonstrated good opto-electrical performance. Moreover, our devices exhibited a broadband spectral photoresponse and gate-tunable response time. Our study suggests the potential use of Bi_2O_2Se in future electronics and optoelectronics applications. In chapter 4 of the thesis, we studied the temperature-dependent electronic transport of as-grown multilayer Bi_2O_2Se nanosheets, in which we discovered and characterized the metal-insulator transition. We found out that in high carrier, the conductivity dependence on carrier density follows classical Boltzmann theory, indicating the existence of linearly screened charged impurity scattering. At low density, this homogeneous screening of electron gas breaks down, resulting in the development of strong charge inhomogeneity, which leads to a percolation-based MIT transition in our system. Charge transport in this insulating regime can be described by the thermal activation

of trapped carriers in the localized states, highlighting the significant role of disorder in this material.

5.2 Future Directions

5.2.1 Encapsulated Bi_2O_2Se

To screen out the role of charged impurities, we have encapsulated Bi_2O_2Se using an HBN dielectric. In Figure 5.1a, the schematic of our device geometry is portrayed. We transferred Bi_2O_2Se to the SiO_2/Si substrate and exfoliated h-BN and graphene on SiO_2/Si. Initially, we picked up h-BN using our Nail Polish assisted transfer method and then placed graphene from this h-BN onto Bi_2O_2Se. Subsequently, we used photolithography, RI, and metal deposition to make edge contacts with the graphene. Figure 5.1c illustrates the schematics of our fabrication process, while Figure 5.1b displays the OM image of this device. Up to this point, we have studied its IV characteristics under an ambient environment. In Figure 5.1d, the linear IV indicates ohmic contacts with graphene. In our Future directions, we plan to investigate its optoelectronic and temperature-dependent electronic transport properties.

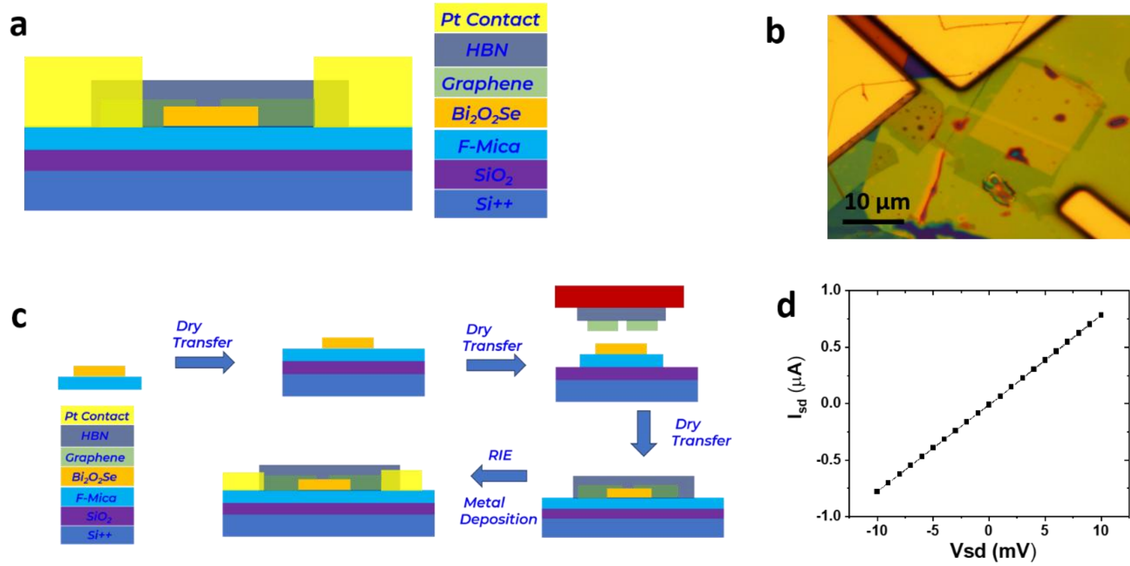

Figure 5.1 (a) Schematic of the Encapsulated Device. (b) OM image of the encapsulated device (c) Schematic depicting the subsequent steps of the fabrication process (d) IV characteristic of the encapsulated device under ambient conditions.

5.2.2 Dual-Gated Bi_2O_2Se

We have fabricated the Dual gate Bi_2O_2Se using h-BN and Si_3N_4 as a top dielectric. Figure 5.2a shows the schematic of our dual gate device where we have used h-BN as a dielectric and graphene is used as a contact. Using our Nail polish assisted dry transfer technique, we transferred as grown Bi_2O_2Se to SiO_2/Si substrate. Then, we picked up exfoliated h-BN from nail polish and exfoliated graphene from h-BN and transferred the h-BN graphene assembly to Bi_2O_2Se. Then,

photolithography and metal deposition are used to make Pt contacts with graphene and a pre-patterned gate contact. Then, we transfer exfoliated graphene over HBN and gate electrode to give a gate connection. As graphene is transparent, using graphene as a gate, contact allows us to do

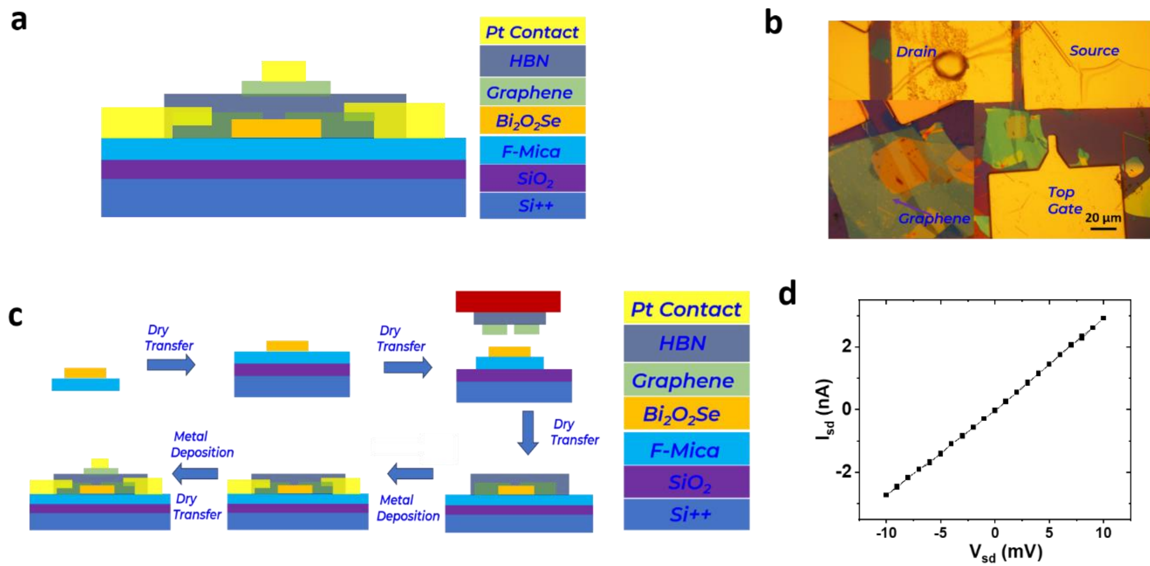

Figure 5.2 (a) Schematic of the dual Gated device in which h-BN is used as a dielectric for top gate and graphene is used as a contact. (b) OM image of the dual gated device. (c) Schematic depicting the subsequent steps of the fabrication process (d) IV characteristic of this device under ambient conditions.

optoelectronic measurements in contrast to opaque metals. Figure 5.2c shows the schematic of the subsequent steps of our transfer process. **Figure 5.2b** is the OM image of the h-BN topgated Device. We have studied its electrical properties in the ambient environment. Figure 5.2d shows

the IV characteristics of our device under ambient conditions. We plan to study its optoelectronic and temperature-dependent electronic properties in future work.

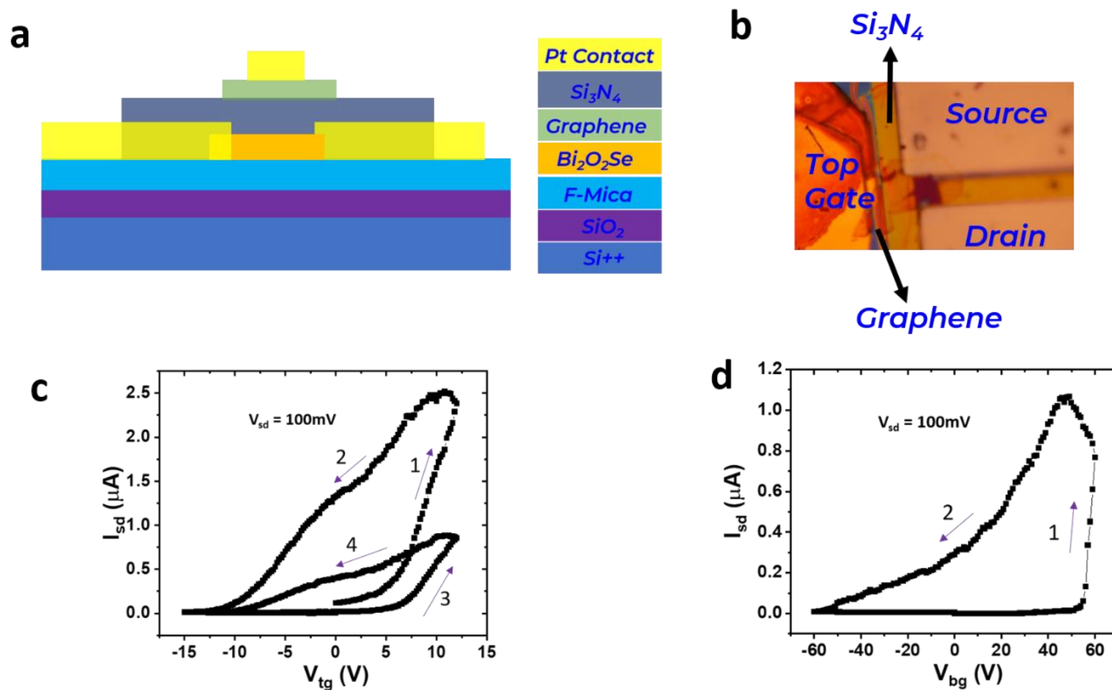

Figure 5.3 (a) Schematic of the Dual Gated device in which Si_3N_4 is used as a top gate. (b) OM image of the dual gated device . (c) Transfer charateristics of the device using top gate and (d) back gate respectively.

Figure 5.3a shows the schematic of our device in which Si_3N_4 is used as a dielectric for the top gate. We transferred as grown Bi_2O_2Se on SiO_2, made two probe devices, and gave gate contact using photolithography. Then, we have used photolithography and sputtering to deposit Si_3N_4 over Bi_2O_2Se. Figure 5.3b shows the Om image of our device. We have studied its electrical properties

under ambient conditions. Figure 5.3c displays the gate scan of our device using the top gate, and Figure 5.3d shows the gate scan using the back gate. In both cases, we observed good gate hysteresis in our system, possibly due to the interfacial trap state between Bi_2O_2Se and Si_3N_4. These preliminary results suggest the potential of these devices for memory and neuromorphic applications, which will be studied in future works.

5.2.3 F-Mica as a Back Gate

Figure 5.4a shows the schematic of our device geometry. Figure 5.4c shows the OM image of our device. To fabricate our device, we have exfoliated graphene and transferred it to a SiO_2/Si substrate. Then, we transferred Bi_2O_2Se f-mica onto this graphene. Photolithography, followed by metal deposition, is used to make two probe contacts on Bi_2O_2Se and a gate contact to graphene. We have done preliminary electrical characterization of our device under ambient conditions. Figure 5.4d shows the IV characteristics of our device, and 5.4e shows the plot of Isd vs. Vbg. In the future, we will investigate the optoelectronic properties of this system and compare it performance with the traditional SiO_2/ Si back gate.

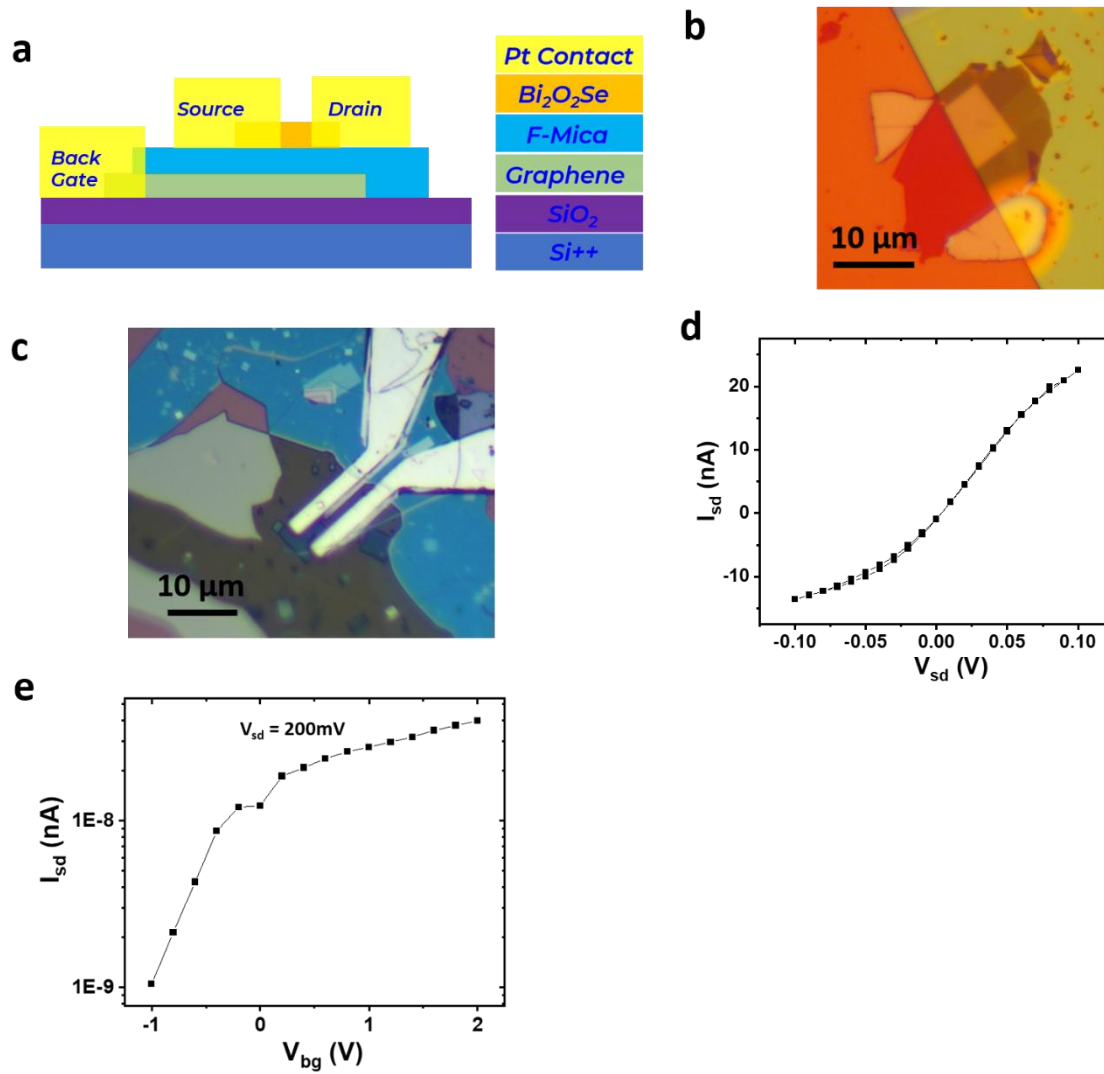

Figure 5.4 (a) Schematic of the device where F-Mica is used as a back gate. (b) OM image after transferring Bi_2O_2Se/f-mica on graphene. (c) OM image of our device. (d) IV characteristics of the device and (e) Isd Vs V_{bg} plot of the device measured under Ambient conditions.

5.2.4 $CsPbBr_3/Bi_2O_2Se$ Heterostructure

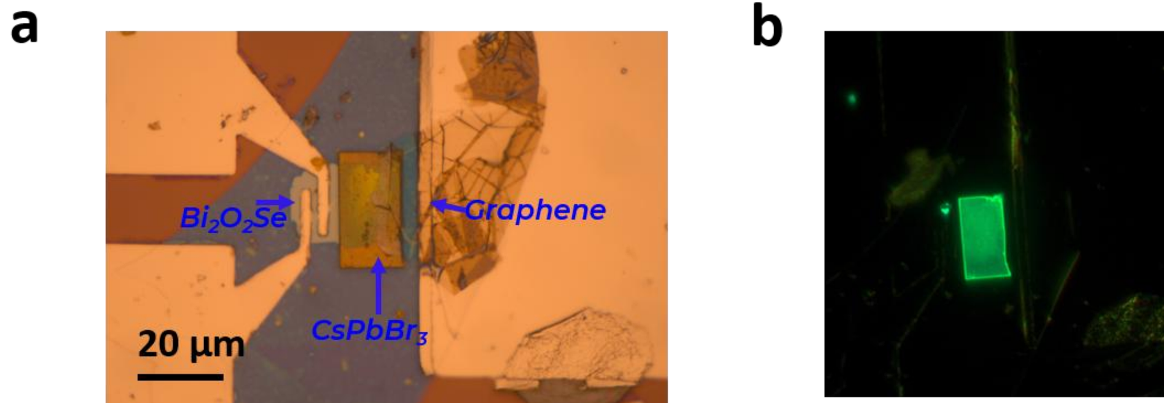

Figure 5.5 (a) OM image of $Bi_2O_2Se/CsPbBr_3$/Graphene Hetrostructure device. (b) Image after transferring $CsPbBr_3$ on Bi_2O_2Se on PL Microscope.

Figure 5.5a shows the OM image of our $CsPbBr_3/Bi_2O_2Se$ heterostructure. First, we fabricated two probe Bi_2O_2Se devices and gave them a pre-patterned metal pad. Then, we transferred the $CsPbBr_3$ crystal over Bi_2O_2Se without touching the metal pad. Figure 5.5b displays the image in the PL microscope, which shows the transferred flake's excellent quality. Then, we transferred graphene onto $CsPbBr_3$ and a metal pad. In the future, we can study its optoelectronic properties. This hybrid device is a good potential candidate of broadband photodetector and photodiode.

Appendix A

Supporting material for Chapter 3

Growth Optimisation

We have optimized the growth conditions of Bi_2O_2Se nanosheets in our CVD set by tuning the growth conditions such as the distance between precursor position, growth time, Temperature of furnace and flow rate.

Effect of Distance between Precursors

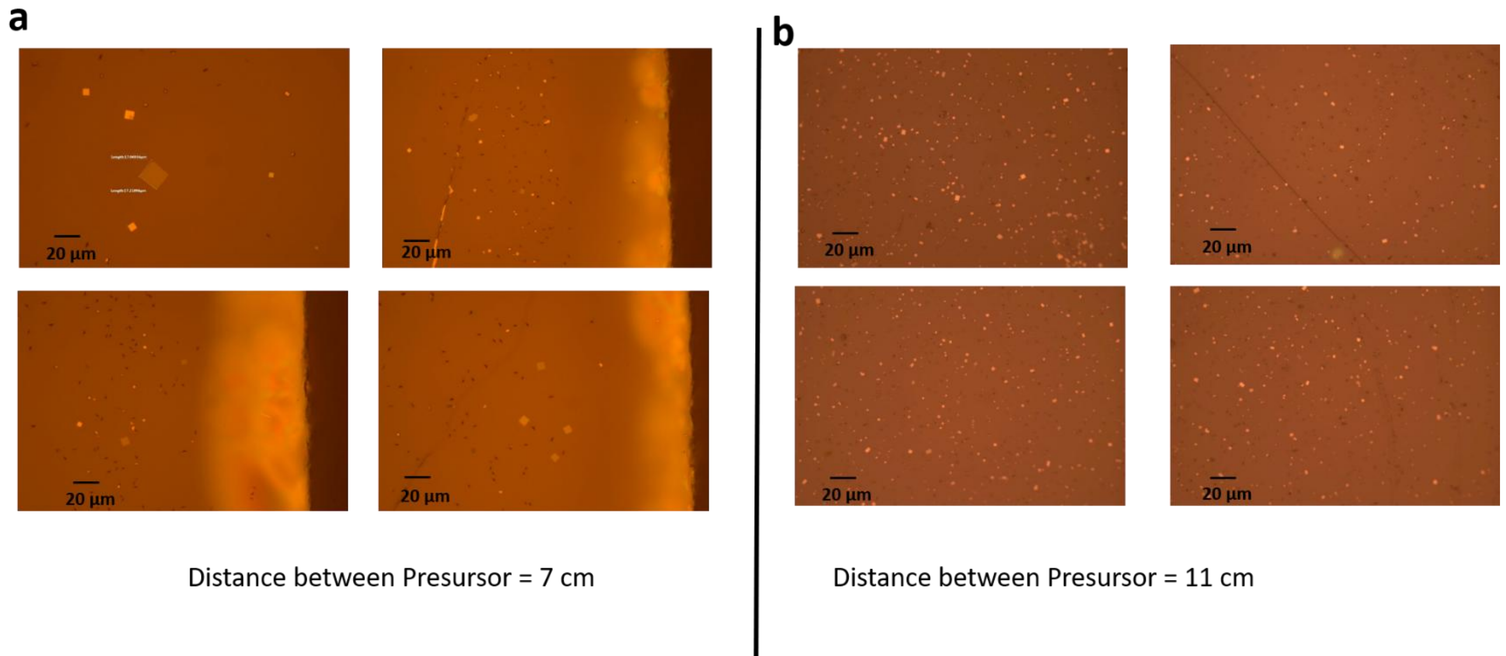

Figure A1.1: Effect of Distance between precursors: a) Left panel displaying OM images of Bi_2O_2Se on F-Mica when distance between precursors is 7 cm and b) 11 cm (Right panel) when distance between precursors is reduced size of sample increases. Temperature of the furnance is set at 640°C .

Effect of Temperature

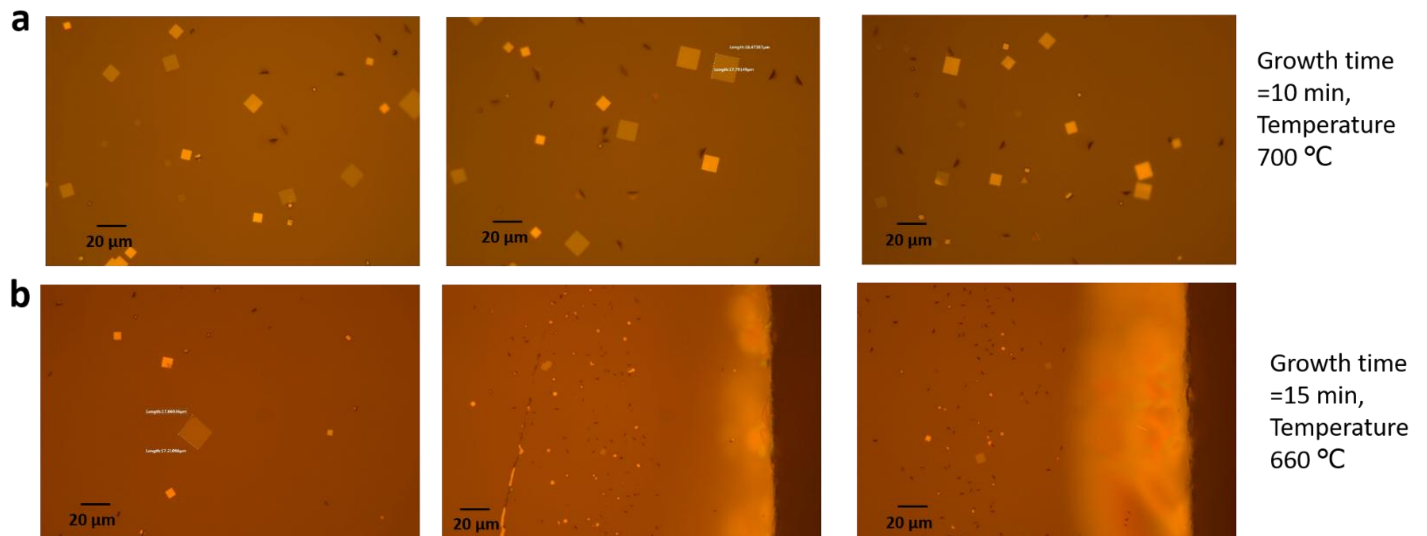

Figure A1.2: Effect of Temperature : a) upper panel shows OM images of Bi_2O_2Se on F-Mica when growth time is 10 minutes and temperature is 700°C and b) when growth time is 15 minutes and temperature is 660 °C (Lower panel) . As temperature increases we got flakes of bigger size and higher density of flakes.

Effect of Flow rate

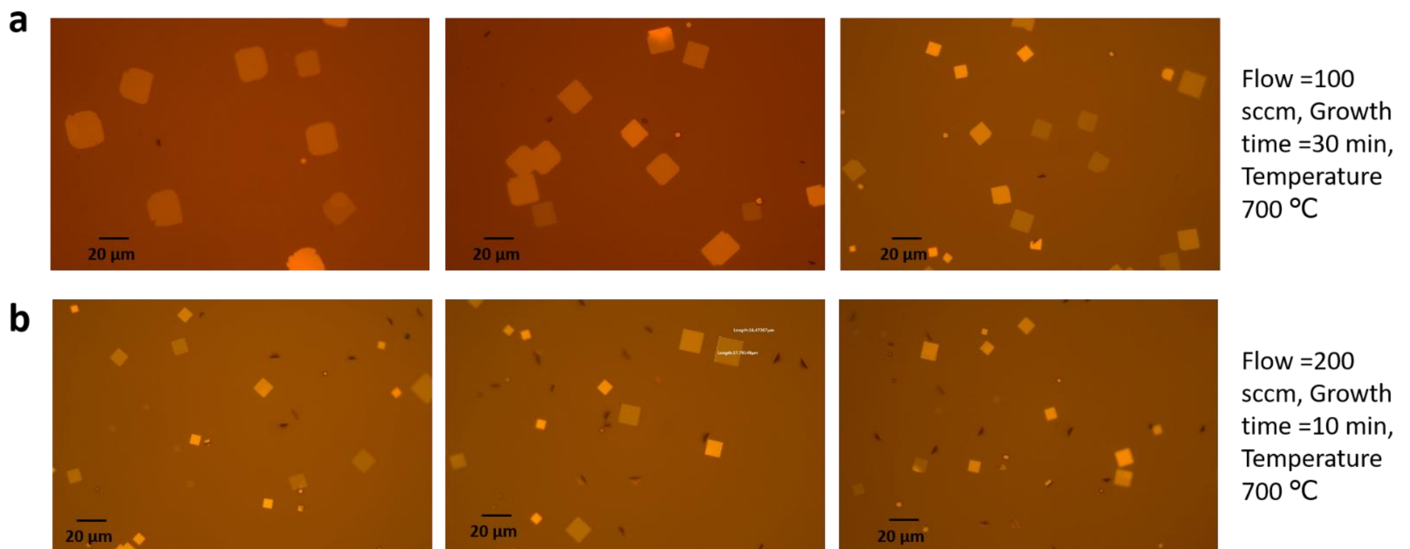

Figure A1.3: Effect of flow rate : a) upper panel shows OM images of Bi_2O_2Se on F-Mica when flow rate is 100 sccm and growth time is 30 minutes and b) when flow rate is 200 sccm growth time is 10 minutes (Lower panel). As flow rate decreases we got thinner and larger flakes

Appendix B

Supporting material for Chapter 4

Supporting figures

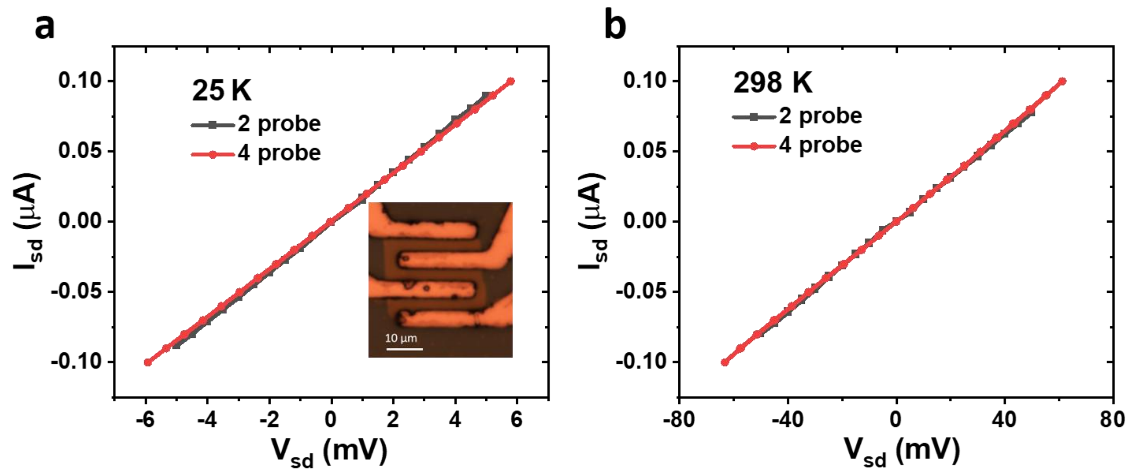

Figures A2: IV characteristics of our device using two probes and four-probe measurements at a) T= 25 K and b) T= 298 K. Inset of a) is the O.M. image of our device.